Summer 2011

Organic semiconductor co-crystals: reactivity, mobility, and spectroscopy

Joseph Charles Sumrak
University of Iowa

ORGANIC SEMICONDUCTOR CO-CRYSTALS: REACTIVITY, MOBILITY, AND SPECTROSCOPY

by

Joseph Charles Sumrak

An Abstract

Of a thesis submitted in partial fulfillment
of the requirements for the Doctor of
Philosophy degree in Chemistry
in the Graduate College of
The University of Iowa

July 2011

Thesis Supervisor: Professor Leonard R. MacGillivray

ABSTRACT

Organic semiconductors are of interest because low processing temperatures and cost which make such materials candidates for flexible electronics. The charge transport properties of the material are largely dependent on solid-state arrangement of the molecules. This thesis focuses on co-crystallization as a means to achieve [2+2] photodimerization with organic semiconductors, the impact the co-crystal former has on mobility, the use of a co-crystal former to obtain different conformations of a flexible system, and the ability to detect the change in conformation by infrared spectroscopy.

[2+2] photodimerization is studied as a way to alter the orientation of the π-systems in the solid state. To align a semiconductor building block into an orientation suitable for [2+2] photodimerization a co-crystallization method was used. The result of the photoreaction is the formation of a dimer in which the π-systems of the semiconductor building block are in a different orientation then before. Changes in the physical properties of the material through photodimerization are explored as a method for patterning thin films.

The impact the second component has on the overall mobility in our system is examined. The second component is not expected to act as a semiconductor and the impact on mobility the by its inclusion in the solid is unknown. The impact of a second component on mobility is studied by observing the mobility of multiple co-crystals along with the mobility of the single component. It was found that the mobility could be increased by a factor of approximately 200 with addition of a second component. The mobility change seen in the two-component crystals is equated to the changes observed in the crystal packing.

The conformation a molecule adopts in a solid can vary. It was discovered that the addition of a second component can be used to select the major conformation a bithiophene adopts in a solid. The change in conformation changes the orientation of the

π-systems between molecules within the solid. The ability for a second component to alter the conformation of a bithiophene is explored. Infrared spectroscopy is used as a facial method to detect the change in the bithiophene conformation.

Abstract Approved: _____
Thesis Supervisor

_____
Title and Department

_____
Date

ORGANIC SEMICONDUCTOR CO-CRYSTALS: REACTIVITY, MOBILITY, AND SPECTROSCOPY

by

Joseph Charles Sumrak

A thesis submitted in partial fulfillment
of the requirements for the Doctor of
Philosophy degree in Chemistry
in the Graduate College of
The University of Iowa

July 2011

Thesis Supervisor: Professor Leonard R. MacGillivray

Graduate College
The University of Iowa
Iowa City, Iowa

CERTIFICATE OF APPROVAL

_____

PH.D. THESIS

_____

This is to certify that the Ph.D. thesis of

Joseph Charles Sumrak

has been approved by the Examining Committee
for the thesis requirement for the Doctor of Philosophy
degree in Chemistry at the July 2011 graduation.

Thesis Committee: _____
Leonard R. MacGillivray, Thesis Supervisor

_____
Daniel M. Quinn

_____
Edward G. Gillan

_____
Alexei V. Tivanski

_____
Markus Wohlgenannt

To My Father and Grandfather Ferrara

Nothing is Impossible. Not if you can imagine it. That’s what being a scientist is all about.

Professor Hubert Farnsworth
Futurama

ACKNOWLEDGMENTS

Let me start off by first acknowledging my family who without I would not be the person I am today. Special thanks to my parents who gave me opportunities to pursue my interest growing up and for their support. Thanks to my older brother Michael for giving me someone to look up to and my younger brother Matthew for pushing me to achieve more. Also to all of my relatives who help instill in me the want to learn. Thanks goes out to all of the friends that I have made along the way; Steve, Matt, Chris, Tony, Dan, Paul, Bhumkia, Kristen, Courtney, Jake, Beth, Tony, Kreso, Manza, Poonam, Saikat, John, Jelena, Becca, Kristin, and many more. Without their companionship the path to this point would not have been as bright and the load heavier. I want to thank AXE for all of the fun and enjoyment that the organization has provided me during my time in Iowa. My fiancée Kim for making the past few years more enjoyable than I thought they could be and making the next many years look bright (thanks for setting us up Andy). Everyone at the department of chemistry that has helped me with my research, especially Dr. Dale Swanson for all of his help in collecting and solving crystal data, as well as the Tivanski group for their collaboration. Finally, thanks to Dr. Len MacGillivray for all that he has taught me the past five years. Without his guidance and support all of the following pages would not have been possible.

ABSTRACT

Organic semiconductors are of interest because low processing temperatures and cost which make such materials candidates for flexible electronics. The charge transport properties of the material are largely dependent on solid-state arrangement of the molecules. This thesis focuses on co-crystallization as a means to achieve [2+2] photodimerization with organic semiconductors, the impact the co-crystal former has on mobility, the use of a co-crystal former to obtain different conformations of a flexible system, and the ability to detect the change in conformation by infrared spectroscopy.

[2+2] photodimerization is studied as a way to alter the orientation of the π-systems in the solid state. To align a semiconductor building block into an orientation suitable for [2+2] photodimerization a co-crystallization method was used. The result of the photoreaction is the formation of a dimer in which the π-systems of the semiconductor building block are in a different orientation then before. Changes in the physical properties of the material through photodimerization are explored as a method for patterning thin films.

The impact the second component has on the overall mobility in our system is examined. The second component is not expected to act as a semiconductor and the impact on mobility the by its inclusion in the solid is unknown. The impact of a second component on mobility is studied by observing the mobility of multiple co-crystals along with the mobility of the single component. It was found that the mobility could be increased by a factor of approximately 200 with addition of a second component. The mobility change seen in the two-component crystals is equated to the changes observed in the crystal packing.

The conformation a molecule adopts in a solid can vary. It was discovered that the addition of a second component can be used to select the major conformation a bithiophene adopts in a solid. The change in conformation changes the orientation of the

π-systems between molecules within the solid. The ability for a second component to alter the conformation of a bithiophene is explored. Infrared spectroscopy is used as a facial method to detect the change in the bithiophene conformation.

TABLE OF CONTENTS

LIST OF TABLES

LIST OF FIGURES

CHAPTER 1: INTRODUCTION

1.1 Crystal engineering

1.1.1 Introduction

Crystal engineering is the use of intermolecular interactions to assemble molecules into a specific solid-state arrangement to achieve desired physical and chemical properties.[1,2] Examples of such intermolecular forces include lipophilic, dipolar, and quadrupole interactions, as well as hydrogen bonding. Control of dimensionality in the solid state using noncovalent bonds has been realized through the formation of zero-dimensional (0-D), 1-D, 2-D, and 3-D assemblies.[1] A key aspect to the growth of crystal engineering is the recognition and use of synthons. Synthons are the smallest structural units which allow for mutual recognition between individual molecules to yield supramolecular structures.[3] Synthons can be broken down into two classes: i) homosynthons and ii) heterosynthons. Homosynthons are comprised of a single functional group that forms intermolecular interactions with itself, where heterosynthons are comprised of two complementary functional groups that interact with each other (Figure 1).[1] Recently, great interest has developed in the utilization of crystal engineering as a bottom-up approach to achieve desired properties of organic solids such as porosity[4,5], nonlinear optics,[6] charge transfer complexes,[7] and monolayers.[8] This thesis will focus on the use of crystal engineering to improve packing and properties of organic semiconductor materials.

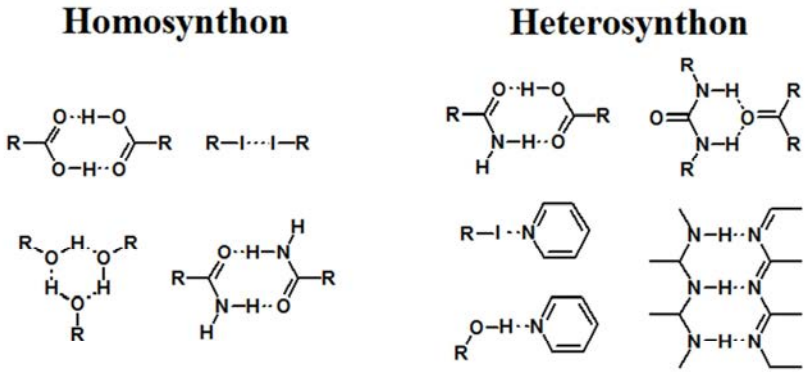

Figure 1: Types of synthons.

1.1.2 Properties of the organic solid-state

The properties of organic solids are dictated not only by the individual molecule but also packing in the solid state. Organic molecules can pack in an ordered array to form a crystalline solid or assemble in a non-ordered array to form an amorphous material. When multiple crystalline forms are available to the molecular constituents of a solid, the different molecular arrangements are called polymorphs.[9] Polymorphism plays an important role in solid-state chemistry due to the fact that different polymorphs can exhibit different properties such as density, solubility, optical, and electrical properties.[10] The ability to change the property of a material by changing crystalline phase has applications in pharmaceutics[11] and materials chemistry.[12] This thesis will focus on altering the solid-state packing of organic semiconductors to affect electronic properties of solids. Specifically, solid-state orientations will be altered through co-crystallization to change the packing from edge-to-face to face-to-face π-stacked arrangements to improve charge mobility.

1.1.3 Co-crystals

The definition of a co-crystal has been in debate in the literature.[13,14] For the purpose of this thesis, co-crystals will be defined as crystals made up of two or more neutral compounds that are solids at room temperature in a definite stoichiometric ratio.[15] Co-crystals, similar to polymorphs, will exhibit physical properties that are different than the pure components. The ability to alter the physical properties of a compound through co-crystallization has generated interest in the pharmaceutical industry,[16,17] as well as materials science.[18,19] Co-crystals are generally obtained by the co-crystallization of two components with complementary recognition groups to form heterosynthons. Co-crystallization allows for a systematic approach towards adjusting properties of a target compound without synthesizing multiple covalent derivatives by changing the solid state packing. A target property of a compound can, thus, be modified by co-crystallization with a co-crystal former to alter packing and, thus, the properties of a solid. If the property is not desired, the co-crystal former can be changed to obtain a different molecular packing to adjust the property.

1.1.4 Co-crystal preparation methods

Co-crystals can be obtained by many of the same methods used to obtain single-component crystals. Solution crystallization *via* slow evaporation is a widely used method to obtain co-crystals.[20] Slow diffusion and hydrothermal synthesis[21] are two alternative solution methods for obtaining co-crystals. When dealing with an insoluble compound in which solution crystallization is less of an option co-crystallization through mechanochemical techniques has proven reliable.[22] Mechanochemical methods involve the combination of the two components in a predetermined ratio and grinding them together, either neat or liquid assisted. Mechanochemistry can avoid the effects of solubility and solvent competition.[22]

1.2 Organic Semiconductors

1.2.1 Introduction

Organic semiconductors are extended conjugated π-systems that have the ability to transport charge when an electrical bias is applied. Organic semiconductors tend to consist of one or more classes of molecular species that possess an extended aromatic structure (e.g. acenes, thiophenes) (Figure 2), and typically begin to demonstrate field

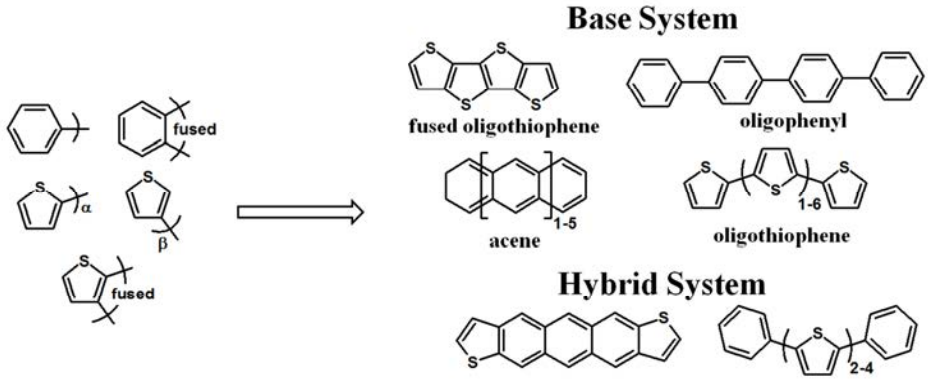

Figure 2: Common organic semiconductors based on acenes and thiophenes.

effect transistor (FET) mobilities upon reaching four, or more, units of conjugation. There is great interest in organic semiconductors owing to a promise of low cost flexible electronics (i.e. RFID tags, displays, e-paper).[23-25] Pentacene has been one of the most widely-studied organic semiconductors and has set a benchmark with room temperature mobilities as high as 35 $cm^2V^{-1}s^{-1}$ for ultra-pure single crystals.[26] The first electronic prototypes of organic semiconductors are already experiencing technological applications in what is poised to be a multibillion dollar industry.

1.2.2 Charge transport of organic semiconductors

The conduction band in organic semiconductors is formed through the interactions of the frontier molecular orbitals of the π-conjugated system of neighboring molecules. Charge transport in organic semiconductors at low temperature can be described as band-like, similar to that for inorganic semiconductors.[27] However, at temperatures above 150 K charge transport is proposed to occur via a hopping mechanism in which electron movement occurs by $M_1 + M_2^+ \rightarrow M_1^+ + M_2$, where M_1 and M_2 are organic semiconducting molecules.[28-30] The rate of hopping can be described by Marcus theory using the following equation (Figure 3).

$$k = \frac{V^2}{\hbar}\left(\frac{\pi}{\lambda k_b T}\right)^{\frac{1}{2}} \exp\left(-\frac{\lambda}{4 k_b T}\right)$$

Figure 3: Marcus theory equation for rate of hopping in organic semiconductors.

Here, k is the rate of hopping, V represents the effective electronic coupling matrix, λ is the reorganization energy, ħ is Planck's constant, k_b is the Boltzmann constant and T is the temperature. The equation shows that the two key parameters in determining charge mobility are the effective electronic coupling matrix (V), which is dictated by the strength of orbital overlap between neighboring molecules, and the reorganization energy (λ), which is the energy required to modify geometry when an electron is added or removed.[27,29]

The reorganization energy takes into account the energy required for rearrangement in molecular geometry, as well as the repolarization of the surrounding area.[30] Rigid molecules are expected to have smaller internal reorganization energies due to a lower intramolecular degree of freedom.[31] Reorganization energy calculations have demonstrated that the number of conjugated units is inversely proportional

reorganizational energy.[30] The observation matches experimental measurements that show an increase in mobility with an increase in number of conjugated thiophene units,[32] which is due to a decrease in HOMO/LUMO gap with an increase in the number of conjugated orbitals.

Due to the effective electronic coupling matrix dependence on strength of frontier molecular orbital interaction, molecular packing plays an important role in determining mobility in organic semiconductors. Interactions between dimers lead to splitting of the HOMOs and LUMOs. The splitting of the HOMO is typically larger than the splitting in the LUMO leading to holes of higher mobility in many organic semiconductors making them p-type semiconductors.[27] Computational studies have shown that even slight shifts in molecular packing will impact the hopping rate.[27,28] Changes in molecular packing impact interactions between wave functions of HOMOs and LUMOs, either constructively or deconstructively, causing either an increase or decrease in the effective coupling matrix, respectively. Increased spacing between molecules also leads to a decrease in mobility.[27]

1.2.3 Device structure and mobility

Organic thin-film transistors (OTFT) are a component in electronic devices made from organic semiconductors that can be created by low-temperature deposition or solution processes.[33] The low processing temperatures of organic semiconductors makes such systems compatible with plastic substrates that are incompatible with silicon.[34] OTFT consist of a substrate, gate, dielectric, semiconductor, source and drain. Charge transport occurs when independent voltages are applied to the gate and between the source and drain. The device configuration can be top contact-top gate or top contact-bottom gate or bottom contact-bottom gate or bottom contact-top gate (Figure 4). The deposition of the organic semiconductor layer is achieved either by vacuum or solution deposition. Vacuum deposition is typically performed at pressures ranging from 10^{-8} to

10^{-6} Torr for small molecules or oligomers.[33] Solution deposition is not limited to the size of the vacuum chamber and, hence, is more compatible with large-area thin film fabrication. However, thin films made from solution tend to be less ordered then those from vacuum deposition.[33]

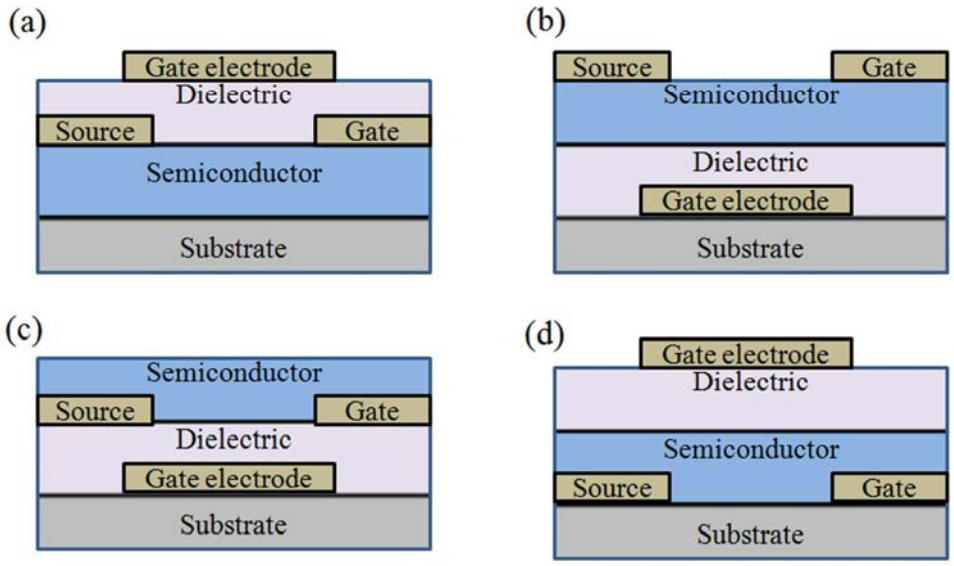

Figure 4: Device schematic of a) top gate-top contacts, b) bottom gate-top contacts, c) bottom gate-bottom contacts, and d) top gate-bottom contacts.

The charge transport ability of an OTFT made of an organic semiconductor determines usefulness. For practical applications, a charge carrier mobility (μ) of 1 $cm^2V^{-1}s^{-1}$ remains a benchmark.[35] Carrier mobility is the ratio between the charge drift velocity and the driving electric field.[31] Charge transport occurs when a gate voltage (V_G) above the threshold voltage (V_T) is applied to collect charge at the semiconductor/dielectric interface, which is carried by the drain voltage (V_D). At low V_D the drain current (I_D) can be expressed using the following equation (Figure 5).[34,36]

$$I_D = \frac{W}{L}\mu C_i(V_G - V_T - \frac{V_D}{2})V_D$$

Figure 5: Equation for drain current at low voltage.

Here, W is the channel width, L is the channel length, and C_i is the capacitance of the dielectric. The carrier mobility (μ) can be calculated from the transconductance which is the slope of a plot of I_D versus V_G at a constant V_D in which $-V_D << -(V_G - V_T)$ (Figure 6).

$$g_m = \frac{WC_i}{L}\mu V_D$$

Figure 6: Equation for transconductance region.

When $-V_D > -(V_G - V_T)$ the drain current reaches the saturation regime and the relation between the drain current and the gate voltage changes to the following equation (Figure 7).

$$I_D = \frac{WC_i\mu}{2L}(V_G - V_T)^2$$

Figure 7: Drain current in saturation regime for organic semiconductors.

The equations show that an increase in gate voltage leads to an increase in mobility. The increased mobility is due to an increase in carrier concentration at the semiconductor/dielectric interface. Factors that limit charge transport are traps that occur

between grain boundaries and impurities in the sample. The traps serve as areas of low charge density and decrease the overall charge transport of the OTFT.

1.2.4 Device patterning

Advanced electronics require minimal cross-talk between adjacent transistors to work properly. To minimize cross-talk, there needs to be an area of minimal conductivity between adjacent transistors, which requires precise control over the placement of semiconductors to create a pattern of charge conducting and non-conducting areas. The patterning of organic semiconductors can be accomplished either through solution[37,38] or vapor techniques.[39] Some of the methods are direct patterning techniques such as molecular jet (MoJet) printing. MoJet printing uses a Knudsen cell equipped with a nozzle and shutter along with a moving stage such that the organic semiconductor is only deposited when the shutter is open and draws a designed pattern.[39] Other methods use stamps or a monolayer to create regions of preferential crystal growth. Once the substrate is patterned, organic semiconducting crystals can be grown in the preferred region through either solution[40] or vapor techniques.[41] Other methods include the use of shadow masks and UV lithography.

1.2.5 Oligoacenes

Of the oligoacenes, tetracene and pentacene have been the main focuses as organic semiconductors. Pure tetracene and pentacene pack in a similar manner (Figure 8).[42] Both molecules exhibit herringbone packing that is dictated by C-H$\cdots\pi$ interactions, and exhibit an angle of approximately 52^{o} between the planar surfaces of nearest-neighbor molecules. The shortest carbon-carbon (C-C) distance between two pentacene molecules is approximately 3.7 Å, which is the same distance as tetracene. A distance of 6.6 Å separates adjacent pentacene molecules in a column of the herringbone structure. Reported mobilities for pentacene are as high as 35 $cm^2V^{-1}s^{-1}$ for extremely pure single crystals.[26] Without rigorous purification, mobilities of approximately 3 $cm^2V^{-1}s^{-1}$ have

been reported for single-crystal pentacene.[43] The highest-reported mobility for a single crystal of tetracene is 1.3 $cm^2V^{-1}s^{-1}$.[44] Hexacene and heptacene have been synthesized, however, the instability of both compounds makes them impractical for use in thin film transistors.[45]

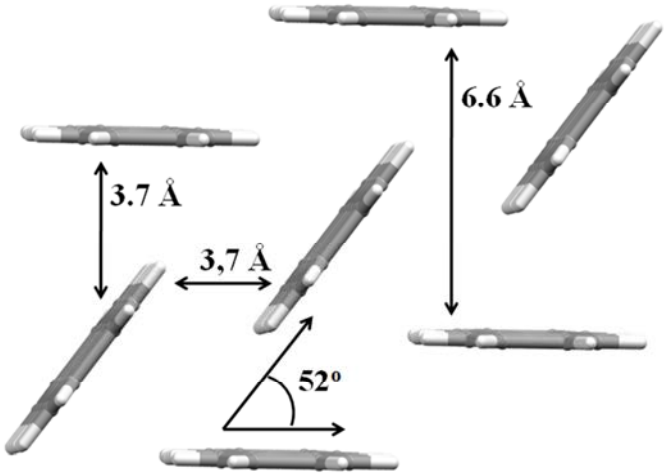

Figure 8: Solid-state packing of pentacene.

1.2.6 Oligothiophenes

Oligothiophenes are of great interest as organic semiconductors owing to ease of their synthesis and chemical modification. The solid-state packing for all unsubstituted oligothiophenes up to octithiophene has been determined via single-crystal X-ray diffraction.[32,46-50] As with the oligoacene counterparts, oligothiophenes exhibit herringbone packing in the solid state (Figure 9). The angle between planar surfaces of oligothiophenes is typically 63°, which is slightly higher than the oligoacenes. The shortest distance between two thiophene rings is on the order of 3.8 Å. A distance of approximately 6.8 Å separates thiophenes in the column of the herringbone structure. As

expected, an increase in the number of thiophene rings in an oligothiophene leads to an increase in mobility (Table 1).

Table 1: Reported mobilities of oligothiophenes

Number of thiophene units	4	5	6	7	8
Mobility (V^2 cm^{-1} s^{-1})	0.006	0.05	0.075	0.13	0.33
Ref	50	32	50	32	50

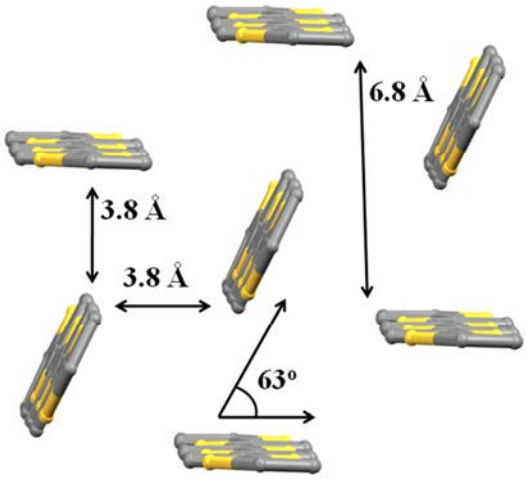

Figure 9: Solid-state packing of sexithiophene.

1.2.7 Structural limitations

As stated above, the charge transport in organic semiconductors occurs *via* a hopping mechanism between nearest conjugated π-surfaces and slight shifts in packing can affect the charge mobility of a material.[28-30] Viewing organic semiconductor molecules as planar objects the angle between two π-surfaces can vary between 90° (i.e. edge-to-face) and 0° (i.e. face-to-face) (Figure 10). Computational studies along with

experimental evidence have shown that a face-to-face packing motif exhibit higher mobilities versus edge-to-face packing.[31,51,52] Face-to-face packing maximizes orbital-orbital interactions, which improves the effective electronic coupling matrix. However, unsubstituted oligoacenes and oligothiophenes are directed into a herringbone packing motif by an electrostatic interaction between δ^+ H-atoms along the edge and the δ^- π-

Figure 10: Stacking of organic semiconductors in a a) edge-to-face and b) face-to-face stacking.

electrons along the face. The C-H$\cdots\pi$ forces the molecules to pack in an edge-to-face fashion that places the π-surfaces at an angle greater than 50^o.[44,49] It is expected that decreasing the angle to closer to 0^o to achieve face-to-face stacking would lead to increased charge transport without a need to increase the size of the conjugated system. Increases in performance with smaller molecules is beneficial because smaller molecules are more stable at ambient conditions and easier to process *via* solution methods.[53]

1.2.8 Crystal engineering organic semiconductors

Since the solid-state structures of unsubstituted organic semiconductors are not ideally suited to achieve high mobilities, structures must be designed to produce more efficient π-π overlap. To this end, attempts to control the arrangements of organic semiconductors through modifying the intermolecular forces that govern the solid-state

packing have been a major focus of research. Changes to packing have been generally accomplished through the covalent introduction, or modification, of substituents along the periphery of semiconductor molecules

1.2.8.1 Steric interactions to adjust crystal packing

One method to improve packing has been the use of bulky side groups to destabilize or eliminate close C-H···π contacts. C-H···π forces are based on electrostatic interactions between δ^+ charges of H-atoms located on the edges of the rings and the δ^- charges on the π-face of the internal ring C-atoms. With the driving force for edge-to-face packing eliminated, there is an increased likelihood for face-to-face stacking. The approach has been developed by Anthony et al., where a pentacene functionalized with triisopropylsilylethynyl (TIPS) groups not only prevented herringbone packing but improved solubility and stability.[54,55] With a reduction in C-H···π interactions achieved, the TIPS-functionalized pentacene packed in a brick motif based on co-facial columns with a 3.5 Å separations between nearest-neighbors acenes (Figure 11). Whereas such

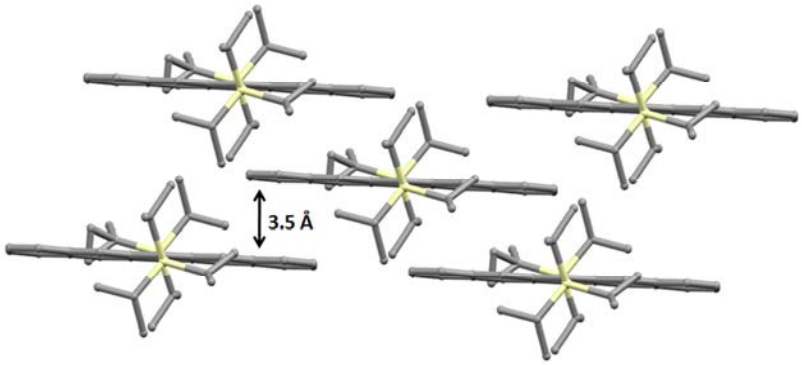

Figure 11: Crystal structure of TIPS-pentacene.

changes to packing led to a significant improvement in π-orbital overlap compared to unsubstituted pentacene, control of a slip-stack arrangement of the pentacenes on a long

molecular axis remained difficult.[56] Mobilities as high as 1.8 $cm^2V^{-1}s^{-1}$ were obtained for TIPS-functionalized pentacenes prepared via solution process methods.[57] Anthony et al. have also successfully extended the method to hexacene and heptacene.[58] The method has been successful in both single crystals and thin film devices, which demonstrates the robustness of steric interactions for potential applications in organic electronics.

Along with TIPS groups, phenyl groups have been used to reduce C-H···π interactions. Ultra-pure single crystals of 5,6,11,12-tetraphenyltetracene, or rubrene, have, afforded a hole mobility of 20 $cm^2V^{-1}s^{-1}$.[59] The mobility is significantly higher than that achieved for single crystals of the parent tetracene.[51] The increase in mobility can be attributed to the increase in co-facial π-stacked interactions along the a-axis in single crystals of the molecule.[60] Mobilities of rubrene in thin films, however, have underperformed single crystals owing to difficulties to achieve crystalline films of the compound.

Nuckolls et al. have recently extended phenyl substitution to pentacene with a series of cruciform-based π-systems; specifically, 6-phenyl-, 6,13-diphenyl-, 6,13-dithienyl-, 5,7,12,14-tetraphenyl-, 1,4,6,8,11,13-hexaphenyl-, and 1,2,3,4,6,8,9,10,11,13-decaphenylpentacene.[61] The phenyl substituents circumvented herringbone packing, however, the packing motifs varied depending upon number of phenyl substitutions. The presence of a single phenyl in 6-phenylpentanene resulted in both edge-to-face and face-to-face packing in the crystal structure. Hexaphenyl- and decaphenylpentacene packed in layered structures directed by edge-to-face C-H···π interactions between the phenyl substitutes with the pentacene backbones separated by 5 Å. The resulting solids did not display measurable mobilities as thin films (Figure 12a). The diphenyl substituted pentacene packed co-facially, however, the long axis of nearest-neighbor acenes were oriented orthogonally and resulted in cage-like superstructures. The solid exhibited a mobility of 8×10^{-5} $cm^2V^{-1}s^{-1}$ (Figure 12b). A mobility of 0.1 $cm^2V^{-1}s^{-1}$ was obtained for the dithienyl derivative, which exhibited the greatest π-π overlap in the series (Figure

12c). Each of these methods circumvented C-H···π interactions to vary the packing motifs. The lack of mobility in hexaphenyl and decaphenyl substituted pentacene demonstrated the importance of π-π overlap in improving mobility.

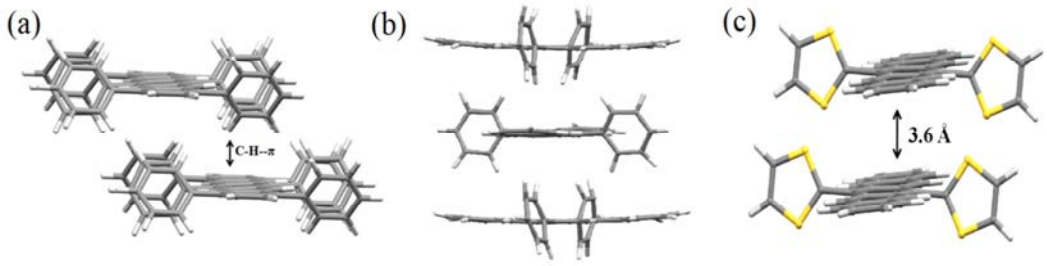

Figure 12: Packing of a) 1,4,6,8,11,18-hexylphenylpentacene, b) 6,13-diphenylpentacene, and c) 6,13-dithienylpentacene.

1.2.8.2 Alkyl chains to adjust crystal packing

Alkyl chains are known to promote layered structures in the solid state through lipophilic interactions. Garnier et al. synthesized 2,5′′′′′′-dihexylsexithiophene (DH6T) to incorporate the self-assembly of alkyl chains into thin films of the semiconductor molecule. [62] Although X-ray diffraction (XRD) revealed the thin film to exhibit herringbone packing similar to unsubstituted sexithiophene (6T), mobility measurements showed a 40-fold increase compared to 6T when both were deposited at room temperature (6T = 2 x 10^{-3} $cm^2V^{-1}s^{-1}$, DH6T = 8 x 10^{-2} $cm^2V^{-1}s^{-1}$).[63] The increase in thin-film mobility in α-alkyl substituted oligothiophenes was attributed to an increase in long-range order owing to a change in the growth mechanism of the thin film from 3D island to a more 2D layered growth. (Figure 13).[64] Halik et al. compared diethyl, dihexyl, and didecyl α,ω-substituted sexithiophenes to study the impact of alkyl substituent length on mobility. Diethyl- and dihexyl-substituted sexithiophene were determined to exhibit superior thin-film mobilities compared to sexithiophene, with the respective mobilities

being 1.1 and 1.0 $cm^2V^{-1}s^{-1}$. α,ω-Didecylsexithiophene, however, showed little improvement versus sexithiophene, with mobilities of 0.1 and 0.07 $cm^2V^{-1}s^{-1}$, respectively, suggesting an optimum alkyl substitution length for charge tranport.[65]

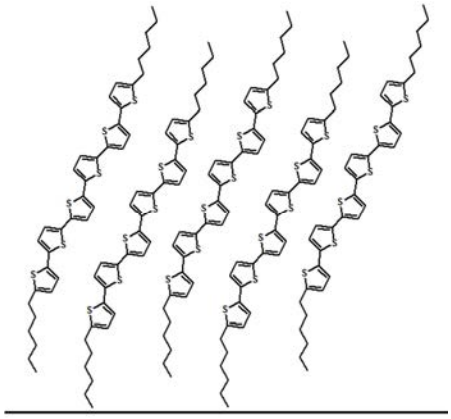

Figure 13: Schematic representation of DH6T thin film.

More recent studies on alkyl-substituted organic semiconductors have involved a hybrid phenyl-thiophene system. Marks et al. demonstrated entirely solution processed devices composed of 5,5′-Bis(4-n-hexylphenyl)-2,2′-bithiophene (dHPTTP) that exhibited higher than expected mobilities (0.07 $cm^2V^{-1}s^{-1}$) for a system with a relatively weak π-conjugation.[66] Single crystal studies on dHPTTP revealed the molecule to exhibit herringbone packing similar to most oligothiophenes (Figure 14). The improvement in mobility was attributed to a decrease in traps in the thin film owing to alkyl-alkyl interactions, similar to DH6T.[67] In related work, Bao et al. have also synthesized a series of alkyl- and alkoxy-substituted bisphenylbithiophenes (PTTP) and bisphenylterthiophenes (PTTTP) to study side chain effects on mobility. It was discovered that branching in the side chain leads to a decrease in mobility. The decrease was attributed to branching increasing steric interactions to an extent that prevented close packing and efficient π-π overlap. The growth modes of the branched substituents were

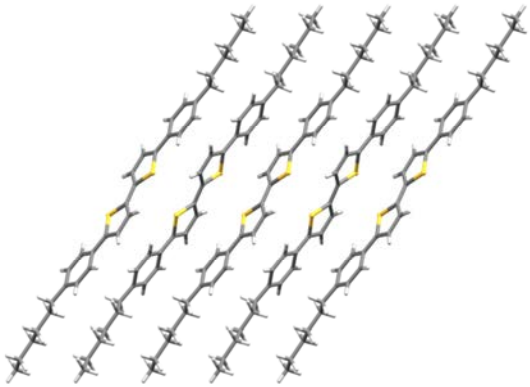

Figure 14: Crystal structure of 5,5'-bis(4-n-hexylphenyl)-2,2'-bithiophene.

also more three dimensional, as opposed to the linear chains, further contributing in the lowering of mobilities and, thus, making it difficult to decouple steric from growth mode effects. When the semiconductor core was changed from PTTP to PTTTP the mobility peaked at a shorter side chain length suggesting an optimal molecular dimension for charge transport.[68] The changes in alkyl lengths played an important role in altering the molecular packing, and thus, can be considered a tool to gauge finer effects of packing on charge transport.

1.2.8.3 Dipolar interactions to adjust crystal packing

The introduction of dipolar interactions within an organic semiconductor molecule provides a means to enforce face-to-face π-stacked arrangements. The arrangements are based on the stacked molecules adopting either an antiparallel or parallel geometry. In this context, Kobayashi et al. have introduced chalcogens (O, S, Te) at the 9,10-position of anthracene and alkylthio groups at the 6,13-position of pentacene to induce π-π stacking through chalcogen-chalcogen interactions.[69] 9,10-dimethoxyanthracene was determined to pack into a herringbone motif with a lack of heteroatom interactions. However, 9,10-bis(methylthio)-anthracene crystallized into 2D

sheets, directed by S···S interactions. Anthracene rings of adjacent stacked sheets formed 1D π-stacked columns. The same packing motif was observed in the case of 6,13-bis(methylthio)pentacene (Figure 15).[70] 9,10-bis(methyltelluro)anthracene also formed sheets through Te···Te interactions.[69] Mobility measurements were not reported for these compounds.

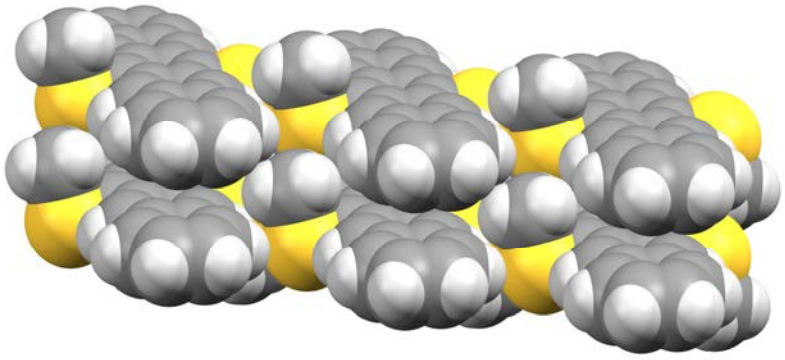

Figure 15: Solid-state packing of 6,13-bis(methylthio)pentacene.

Halogen-halogen interactions have been investigated by Bao et al. to increase π-π stacking in crystals of 5-chlorotetracene (CT), 5,11-dichlorotetracene (DCT), and 5-bromotetracene (BT).[51] CT and BT exhibited isostructural herringbone arrangements while DCT adopted a face-to-face slipped π-stacking motif with an intermolecular distance of 3.48 Å (Figure 16). Crystals grown by vapor growth methods for BT exhibited a mobility of 0.3 $cm^2\ V^{-1}s^{-1}$. Crystals of DCT grown by the same method exhibited a mobility of 1.6 $cm^2\ V^{-1}s^{-1}$, which is the highest reported for tetracene. The increase in mobility in the case of DCT relative to tetracene was attributed to the enhanced π-orbital overlap owing to the change in packing.

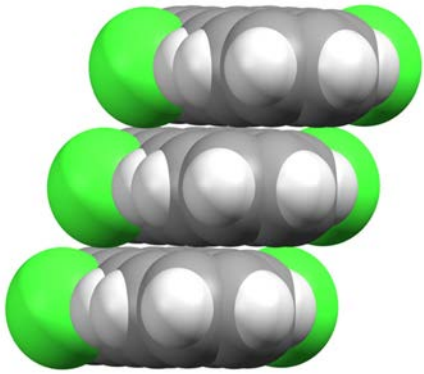

Figure 16: Crystal structure of 5,11-dichlorotetracene.

1.2.8.4 Quadrupole interactions to adjust crystal packing

Molecular complexes between electron rich and electron poor aromatic rings have been known since 1960.[71] The self-assembly via quadrupole interactions has been applied in supramolecular construction since the late 1990s.[72,73] In 2003, Marks et al. reported the first examples of semiconductors that incorporate quadrupole interactions. Two fluoroarene units were incorporated with four thiophene units to make three symmetrical molecules; specifically, 2,5‴-bis(2,3,4,5,6-pentafluorophenyl)-quaterthiophene, 5,5′-bis[2,3,5,6-tetrafluoro-4-(2-thienyl)phenyl]-bithiophene, and 5,5″-(2,2′,3,3′,5,5′,6,6′-octafluoro[1,1′-biphenyl]-4,4′-diyl)bisbithiophene (figure 17).[74] All three molecules exhibited co-facial packing of the electron-rich thiophene units with the electron-deficient fluoroarene units. The compounds in which the fluoroarene units were spaced by a quaterthiophene or bithiophene displayed co-facial π-π stacking distances of 3.20 Å and 3.37Å, respectively. The distances are remarkably short for thiophene-based oligomers (Figure17a and b). The compound in which the fluoroarene units were adjacent to each other exhibited a torsion angle of approximately 54^{o}, which disrupts the π-conjugation (Figure 17c). Mobilities of 0.08, 0.01, and 4 x 10^{-5} cm^2 $V^{-1}s^{-1}$ were

reported for the fluoroarenes with the quaterthiophene spacer, bithiophene spacer, and no spacer, respectively, which generally compare to that of α-6T (0.03 cm^2 $V^{-1}s^{-1}$).[74]

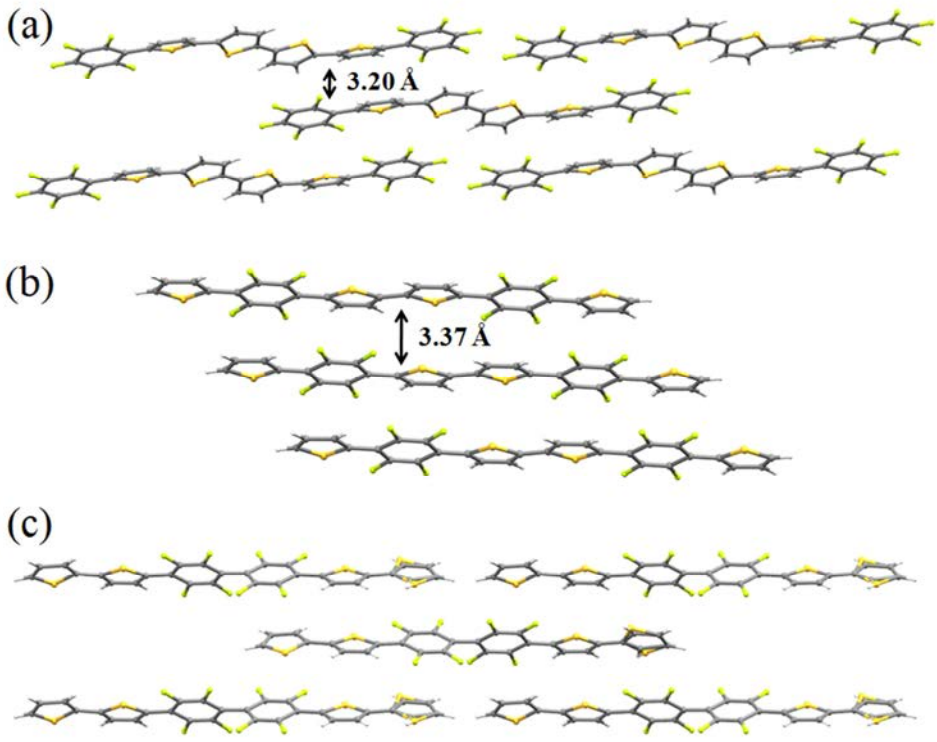

Figure 17: Packing of a) 2,5'''-bis(2,3,4,5,6-pentafluorophenyl)-quaterthiophene, b) 5,5'-bis[2,3,5,6-tetrafluoro-4-(2-thienyl)phenyl]-bithiophene, and c) 5,5''-(2,2',3,3',5,5',6,6'-octafluoro(1,1'-biphenyl)-4,4'-diyl)bisbithiophene.

Anthony et al. have integrated quadrupole interactions into TIPS-based pentacenes to improve packing.[75] In particular, changing one or both of the terminal benzene rings in pentacene to TIPS-tetrafluoropentacene or TIPS-octafluoropentacene, led to increased face-to-face π-interactions. Both compounds adopted 2-D π-stacked arrangements similar to TIPS pentacene. The compounds were stable in solution and the solid state when exposed to air and light. The intermolecular π-stacking distances decreased with an increase in the number of fluoro groups, with the average

intermolecular distances being reduced from 3.43 Å in the nonfluorinated compound, to 3.36 Å in tetrafluoro and 3.28 Å in the octaflouro compound (Figure 18). However, in all cases the slip-stacked arrangement along the long axis of the pentacene molecules was prevalent. Nevertheless, the reduction in the intermolecular spacing was accompanied by an increase in mobility from 0.001 to 0.014 to 0.045 $cm^2V^{-1}s^{-1}$ for TIPS-pentacene, TIPS-tetrafluoropentacne, and TIPS-octafluoropentacene respectively when prepared under the same evaporation conditions. A similar introduction of perfluoroarene groups to improve stacking has been demonstrated by Swager et al. involving tetracene derivatives[76] and Watson et al. using polycyclic aromatics.[77]

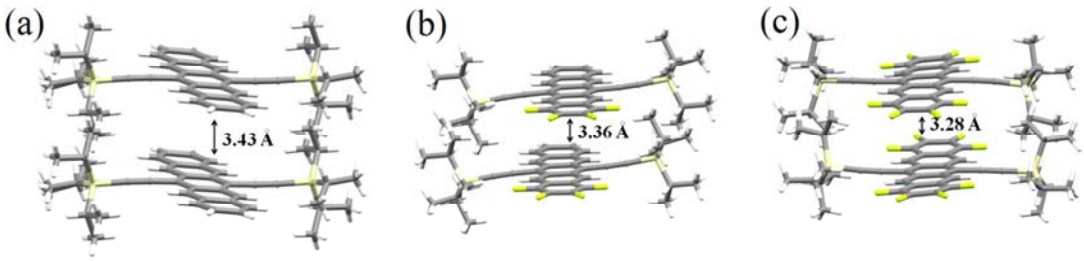

Figure 18: Dimer distance of a) TIPS-pentacene, b) TIPS-tetrafluoropentacene, and c) TIPS-octafluoropentacene.

Nuckolls et al. have used quinone moieties to achieve a quadrupole interaction that improved stacking. The syntheses, packings, and mobilities of three acene-quinone compounds, namely, 2,3-dimethyl-1,4-hexacene-quinone, 2,3-dimethyl-1,4-pentacene-quinone, and 5,6-hexacene-quinone were described. Single crystals of the pentacene-quinone revealed a head-to-tail arrangement with an intermolecular distance of 3.25 Å between π-surfaces and a mobility of 2×10^{-3} cm^2 $V^{-1}s^{-1}$ was obtained for thin films based off of pentacene-quinone. Single crystals for dimethyl hexacene-quinone were not suitable for XRD, however, a mobility of 5.2×10^{-2} cm^2 $V^{-1}s^{-1}$ with an on/off ratio of greater than 10^6 was obtained for thin films. Experimental data suggest that dimethyl

hexacene-quinone adopts the same head-to-tail arrangement as the pentacene-quinone (Figure 19).[61] Chang et al. have also recently described a donor-acceptor interaction integrated into a thiophene. In particular, the solid-state structure of 2,5-di(pyrimidin-5-yl)thieno[3,2-b]thiophene revealed π-stacking achieved *via* electron-rich S-atom of the thiophene and electron-poor C-atoms of the pyrimidine.[78] The use of such quadrupole interactions is promising to control π-π arrangements; however, low mobilities may be attributed to the electronegative substituents (i.e. O-atom) along the aromatic core. The direct placement may cause a trapping effect, effectively lowering the observed performance.

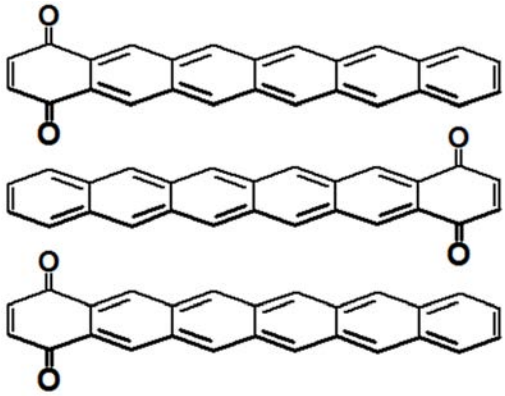

Figure 19: Scheme of solid state head-to-tail orientation of 5,6-hexacene-quinone.

1.2.8.5 Hydrogen bonds to adjust crystal packing

The first study that incorporated hydrogen bonds as a means to affect the self-assembly of an organic semiconductor in the solid state was reported by Barbarella et al. in 1996. 2-hydroxyethyl groups were added to the backbones of 2T, 4T, and 6T in the forms of 3,3′-bis(2-hydroxyethyl)-2,2′-bithiophene, 3,3′,4″3‴-tetrakis(2-hydroxyethyl)-2,2′:5′,2″:5″,2‴-quaterthiophene, and 3,3,4″,3‴,4⁗,3⁗′-hexakis(2-hydroxyethyl)-2,2′:5′,2″:5″,2‴:5‴,2⁗:5⁗,2⁗′-sexithiophene. Although a crystal structure of the

bithiophene revealed intermolecular O-H···O hydrogen bonds, a large twist angle of approximately 67^{o} between thiophene units of the backbone effectively disrupted the conjugation of the molecule (Figure 20)[79] and circumvented the formation of face-to-face stacking. The bithiophenes, however, packed into a columnar arrangement. Crystal structures were not obtained for the quaterthiophene or sexithiophene derivative. UV adsorption studies involving the longer derivatives suggested each to exhibit a largely-twisted conformation, a non-ideal conformation for achieving high mobility, in solution similar to the bithiophene derivative.

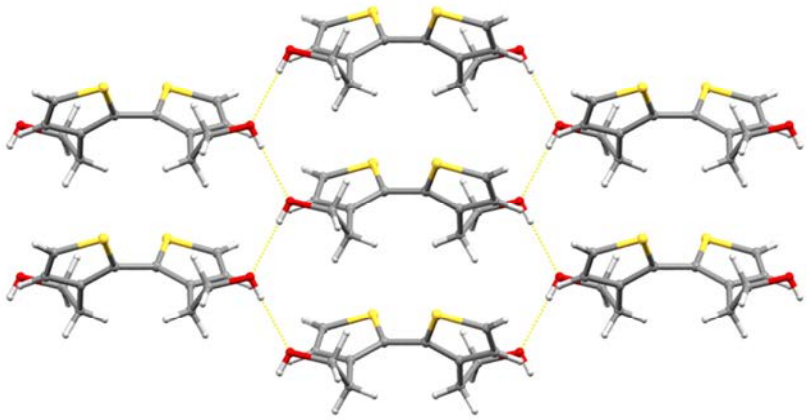

Figure 20: Hydrogen bonded network of 3,3'-bis(2-hydroxyethyl)-2,2'-bithiophene.

Feringa et al. have synthesized a series of bisurea compounds with an oligothiophene spacer in an attempt to form infinite 1-D π-stacked columns. Specifically, 2,5-di(4-(3-dodecyl-ureido)butyl)thiophene and 5,5′-Di(4-(3-dodecylureido)butyl)-2,2′-bithiophene were described. Organogels formed upon cooling each compound to room temperature in tetralin and 1,2-dichloroethane. Characterization of the gels using infrared spectroscopy, scanning electron microscopy, and powder X-ray diffraction revealed the formation of lamellar fibers formed through the hydrogen-bonded urea groups. It was

suggested that the lamellar arrangement of the bithiophene derivative corresponds to co-facially stacked bithiophene moieties with an intermolecular distance on the order of 3.0 Å (Figure 21). Conductive properties of the bisurea compounds were studied via pulse-radiolysis time-resolved microwave conductivity. The bithiophene bisurea compound displayed a mobility of (5 ± 0.2) x 10^{-3} cm^2 $V^{-1}s^{-1}$, which is higher than unsubstituted quaterthiophene (1 x 10^{-3} $cm^2V^{-1}s^{-1}$) studied by the same technique.[80] The growth mechanisms of the fibers from solution and electronic properties have been further probed by Rep et al. and Gequiere et al., respectively.[81,82] While the improved mobility materials have not been incorporated in devices, the finding is an encouraging step towards the use of hydrogen bonds to direct molecular self-assembly where the electronegative substituents do not appear to have an adverse effect on the transport properties.

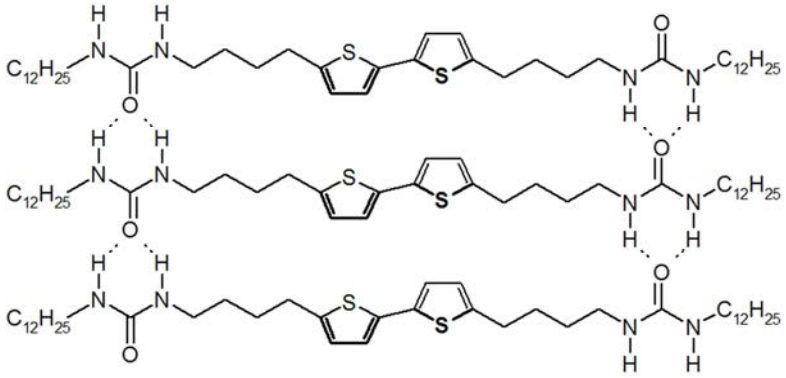

Figure 21: Schematic of solid-state packing of 5,5'-di(4-(3-dodecylureido)butyl)2-2'-bithiophene through 1-D hydrogen bonded network.

1.2.8.6 Co-crystals to adjust crystal packing

Recently, our research group described how face-to-face stacking of semiconductor molecules can be achieved in two-component solids, or co-crystals. The method involves co-crystallizing a semiconductor molecule with a second molecule,

termed the semiconductor co-crystal former (SCCF), that is designed to enforce, via intermolecular bonds, the stacking of the semiconductor in a face-to-face arrangement.[19] The key to the co-crystal approach is that the SCCF effectively decouples the organization of the semiconductor within the crystal from the effects of long-range crystal packing. More specifically, the bifunctional SCCF utilizes hydrogen bonds to enforce stacking of acenes and thiophenes functionalized with appropriate molecular

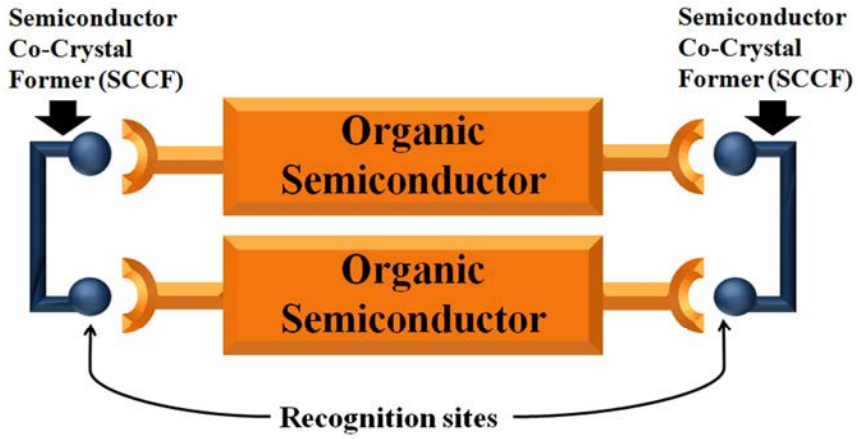

Figure 22: Schematic representation of co-crystallization of an organic semiconductor and semiconductor co-crystal former.

recognition sites (Figure 22). Using a series of 1,3-dihydroxybenzenes, or resorcinols, as SCCFs, the approach has been used to successfully enforce π-π stacking between both an oligoacene and a thiophene within co-crystals of 2(5-iodoresorcinol)·2(9,10-bis(4-pyridylethynyl)anthracene) and 2(5-methylresorcinol)·2(2,5-bis(4-pyridylethynyl)thiophene), respectively. The acene and thiophene were forced into face-to-face stacks with separation distances of 3.44 Å and 3.56 Å, respectively (Figure 23).

The hydrogen-bonded assemblies were shown to self-assemble into face-to-face arrangements, which enabled the formation of extended π-stacked structures. We are working to expand the components of the modular approach to semiconductors of

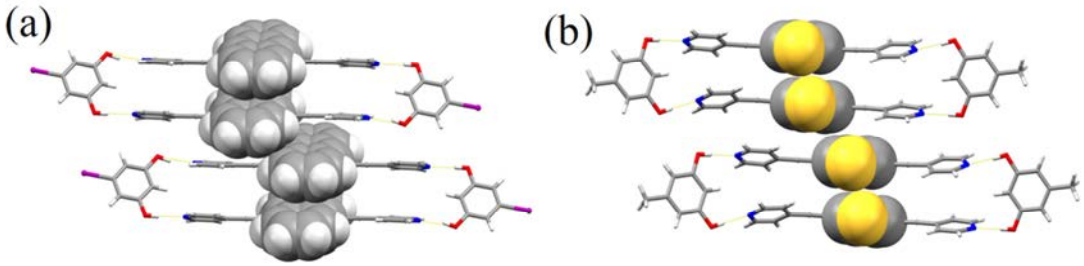

Figure 23: Solid-state packing of a) 2(5-iodoresorcinol)·2(9,10-bis(4-pyridylethynyl)anthracene) and b) 2(5-methylresorcinol)·2(2,5-bis(4-pryidylethynyl)thiophene).

increasing complexity and determine the mobilities of the resulting solids.

1.3 Dissertation overview

The focus of this dissertation will be on the use of co-crystals to affect the structures and properties of organic semiconductor materials. The focus will be accomplished by synthesizing organic semiconductor molecules with a pyridyl group to act as a hydrogen bond acceptor. The organic semiconductor will then be co-crystallized with a resorcinol based SCCF that will direct the organic semiconductor into a face-to-face arrangement. The face-to-face arrangement is not only a more ideal packing for charge transport but we will show allows for the further modification to the solid through a covalent bond forming reaction; namely, a[2+2] photodimerization.

More specifically, chapter two will focus on the synthesis of pyridyl-functionalized organic semiconductors with an ethylene group suitable for [2+2] photodimerization. It will be shown that 0-D assemblies can be formed through co-crystallization of both thiophene and naphthalene units. The resulting co-crystals will be

exposed to ultraviolet (UV) light to induce photodimerization. Photodimerization will be shown to achieve yields greater than 90% for thiophenes in the solid state. Photodimerization using the components within thin films will then be used as a patterning method.

Chapter three will focus on the effect of a SCCF on mobility of crystalline organic semiconductors. Specifically, effects of various substituted resorcinols on the mobility of *trans*-1,2-bis(2-(4-pyridyl)-thien-5-yl)ethylene (DTE) will be described. The mobility measurements are the first performed on co-crystals and will show that co-crystallization is a viable method to improve the mobility of an organic semiconductor. The resulting mobilities are related to the overall packing of the co-crystals showing how enforced face-to-face packing improves mobility.

Chapter four will focus on the use of co-crystals to isolate different conformations of an oligothiophene compound. Specifically, the major conformation of the bithiophene moiety of 1-(4-pyridyl)-2-(5-(2,2'-bithienyl))ethylene (P2TE) present in a solid can either be the *anti*-conformation or the less stable *syn*-conformations depending on the SCCF. Infrared (IR) spectroscopy is shown as a means to identify conformations through monitoring changes in out-of-plane C-H and in-plane C-S stretches. Specifically, it will be demonstrated that IR spectroscopy can be used to detect the change in conformation for conformational polymorph of a terthiophene derivative.

Overall, this thesis work investigates how the co-crystallization of organic semiconductors can lead to changes in structures and properties. The change in properties is due to the change in the solid-state packing cause by the introduction of the SCCF. The ability to alter the properties of organic semiconductors is expected to aid advancements of the field of organic electronics.

CHAPTER 2: PHOTOREACTIVITY OF ORGANIC SEMICONDUCTORS AND CO-CRYSTAL THIN FILMS

2.1 Introduction

With the growth of organic semiconductors as promising materials for use in organic light emitting devices (OLEDs) and OTFTs, there comes a challenge to develop fabrication methods. Advanced electronics (i.e. active matrix displays and sensors) require minimal cross-talk between neighboring devices. Multiple techniques have been developed for the patterning of organic semiconductors. Some of the techniques used in patterning organic semiconductors are physical masks,[83] nozzle printing techniques,[84] stamps,[85] monolayers[41,86] and photolithography.[87] The goal of each technique is to control the deposition of organic semiconductor material on the substrate to fabricate a desired circuit pattern. Many of these techniques involve multiple steps to cast the organic semiconductor as a crystalline thin film, which may have a lower mobility than a single crystal due to grain boundaries.

2.2 Overview

The chapter herein will introduce a possible approach to pattern organic semiconductor materials. The approach aims to utilize UV light to induce a [2+2] photodimerization between neighboring organic semiconductor molecules in specific regions of an organic semiconducting crystal or thin film so as to alter charge mobility. We expect the approach to be realized by photodimerization since the reaction changes conjugated length and, thus, the HOMO/LUMO energy levels and the distances between the semiconducting moieties. Since [2+2] photodimerizations can proceed *via* single-crystal-to-single-crystal (SCSC) reactivity,[88] the method could, in principle, be used to pattern a single crystal (Figure 24). The patterning of a single crystal of an organic semiconductor is expected to overcome problems of grain boundaries, which diminish charge mobility and, thus, allow for maximum charge mobility of the material.

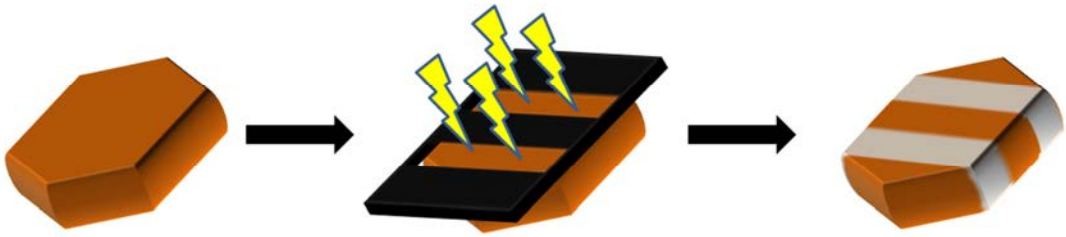

Figure 24: Schematic representation of photopatterning of a single crystal.

2.3 Patterning techniques of thin films

2.3.1 Physical masks and nozzle techniques

One of the common techniques used in device patterning is physical masks. Physical mask techniques involve passing material, either as a solution or vapor, through openings in the mask to produce the desired pattern (Figure 25). The two types of physical masks used for printing are screen printing and shadow masking. In screen

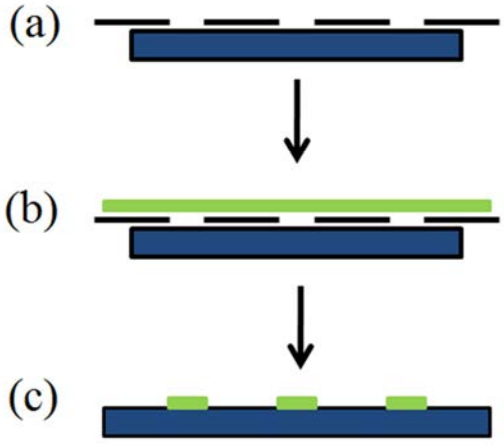

Figure 25: Shadow mask printing a) orientation of shadow mask for desired patterned, b) printing through mask and c) resulting pattern.

printing, a template, either metal or plastic, with windows to create the desired features is placed in contact with the substrate. A solution is then pushed through the openings using a blade. Once the solution is dry, the mask is removed leaving the desired pattern.[89] Screen printing is an additive technique. The gate, source, and drain must be added separately by processes that do not degrade the organic semiconductor layer. Screen printing has been used to create devices of poly(3-hexylthiophene) with mobilities as high as 0.03 $cm^2V^{-1}s^{-1}$ with resolutions as low as 100 μm.[90] However, for screen printing to work the semiconductor must be soluble, which makes the process incompatible with many unsubstituted oligomers and polymers that exhibit low solubility.

Shadow mask printing is similar to screen printing, but the material is deposited through the mask to create desired features with resolutions as low as 5 μm.[91] The technique has already been utilized by several companies to make full color displays of an OLED.[92] Shadow mask, like screen printing, is an additive process, but unlike screen printing there are no problems with solvents affecting the previous layer. A new mask needs to be aligned before the deposition of the next layer. The process has been used to make a RFID card using pentacene as the organic semiconductor.[93] Some drawbacks to the technique is the need for it to be performed at reduced pressure placing a limit on the substrate size to the size of the vacuum chamber, and the need for precise control of the substrate and evaporation source.[33]

Nozzle techniques can use either solution (inkjet printing)[84,94] or vapor deposition (molecular jet printing)[39] methods, and function similar to modern printers and have been used to make functional OLED displays.[92] The nozzle is stationary while the support moves to allow for deposition in the desired location (Figure 26). Deposition only occurs when the nozzle is open and is closed between features to prevent deposition. The size of the features is limited by the nozzle size. Channels down to 15 μm with mobilities of 0.20 $cm^2V^{-1}s^{-1}$ have been created with pentacene with this technique.[39] Nozzle techniques improve on the physical mask techniques by removing the need for a mask,

Figure 26: Scheme for nozzle printing.

which eliminates all cost associated with their fabrication and upkeep, and waste less material. Nozzle techniques, like physical masks, require multiple nozzles, one for each layer and high scanning speeds to be used for high-throughput manufacturing.[92]

2.3.2 Stamping

Stamps have been used for direct patterning of organic semiconductors. An advantage of direct printing is the absence of chemical treatment that can hinder charge transportation.[96] Direct patterning using a stamp requires that there be a difference in the strength of adhesion between the stamp and the substrate. Adhesion can be further improved with the addition of excess pressure and heat. The difference in adhesion force can be used either to add the organic layer or remove it from specific locations (Figure 27). A device in which the gate, source, and drain electrodes, and pentacene layer were added by direct patterning *via* a stamp demonstrated a current mobility of 0.09 $cm^2V^{-1}s^{-1}$. The process was demonstrated to also work for poly(3-hexylthiophene) and carbon

Figure 27: Scheme for stamping a) stamp with desired material is brought into contact with substrate, b) transfer of substance to substrate and c) removal of stamp.

nanotubes.[85] The reverse process of removal of unwanted areas to yield the desired pattern has also been demonstrated. In this method, a PDMS mold is brought into contact with the organic surface under vacuum before annealing. The thin film is then annealed while in contact with the PDMS mold. After annealing the mold is removed with the unwanted areas to yield the desired pattern. The method was able to yield regions of organic material ranging from 1μm to 70 μm.[95]

2.3.3 Monolayer for site specific crystallization

Single crystals represent the most efficient mode of charge mobility due to the long range order and a lack of defects. However, the direct placement of multiple single crystals to create a large area display would be tedious and inefficient for device fabrication. Monolayers have, thus, been used to create sites for preferential crystal growth (Figure 28). It has been demonstrated that directly stamping a layer of octadecyltriethoxysilane (OTS) on a silicon dioxide substrate causes preferential crystal growth on top of the OTS layer through vapor growth for pentacene, rubrene, and

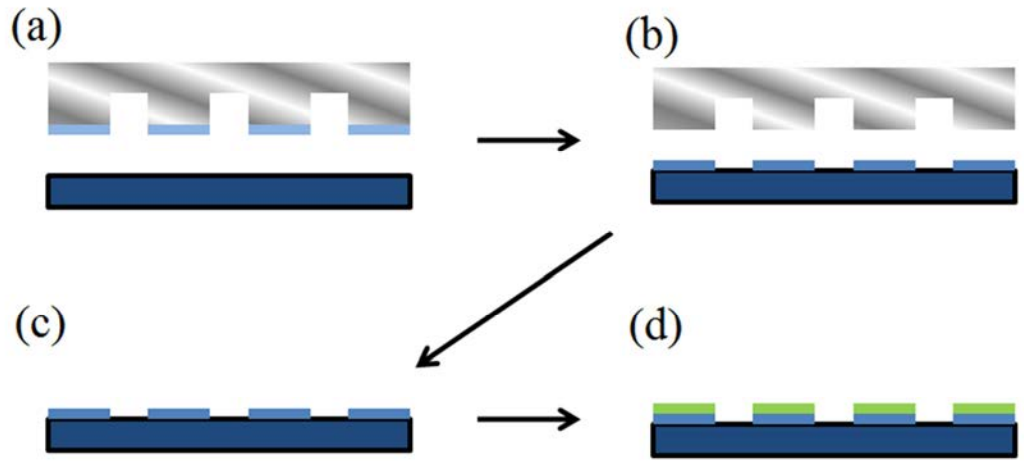

Figure 28: Schematic representation of monolayer for site specific crystallization a-c) stamping of monolayer and d) deposition of organic semiconductor on monolayer.

fullerene.[41] Transistors arrays as small as 25 μm^2 with mobilities as high as 2.4 $cm^2V^{-1}s^{-1}$ were fabricated on flexible substrates using this method.[41] The method was also demonstrated for solution printing. Solution printing is done by dipping a substrate patterned with OTS sites in a suspension of a halogenated aromatic, which the organic semiconductor is dissolved, in water for five seconds. Upon evaporation crystals showed preferential growth at the OTS sites due to hydrophobic interactions.[96] However, there is a lack of control over the orientation of the single crystals while channels can be bridged by multiple crystals allowing for multiple paths for charge transfer.

2.3.4 Photolithography

Photolithography is the dominant manufacturing approach for inorganic electronics and optoelectronics. However, photolithography has not been widely applied to patterning organic semiconductors due to the incompatibility of the process with many organic compounds.[92] Photolithography has been demonstrated as a technique to pattern thin films of both polymers[97] and small molecule organic semiconductors.[38,98] In this technique a solution cast thin film is patterned with ultraviolet or visual light through the use of a photomask. The irradiated area undergoes a chemical reaction to make the material insoluble whereas the protected area remains soluble. The protected area is then removed *via* dissolution leaving behind only the exposed material in the desired pattern. The patterned material is then subjected to additional steps to activate conductive properties (Figure 29). The method was used to pattern a pentacene thin film with features as small as 40 μm with mobilities as high as 0.25 $cm^2V^{-1}s^{-1}$.[38] The lower mobility when compared to other thin films of pentacene is likely due to impurities from the multiple steps or decreased grain size.

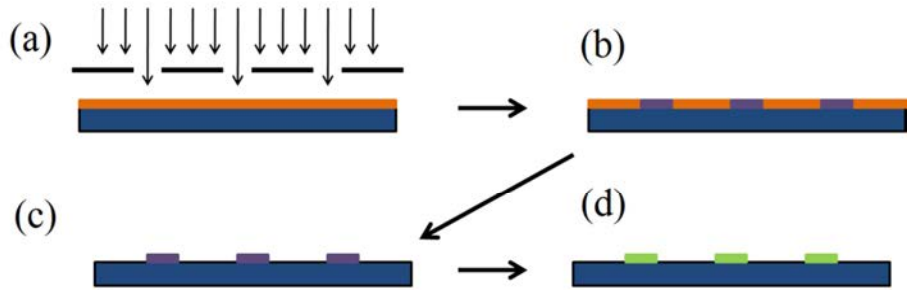

Figure 29: Schematic representation of photolithography method for creating patterned organic thin films.

2.4 Photoreactive solids

2.4.1 Requirements for photoreactivity

Requirements for a [2+2] photodimerization to proceed in the solid state were outlined by Schmidt *et.al.* in 1964 through the study of cinnamic acid derivatives. The acid derivatives were categorized according to unit cell dimensions into three groups α, β, and γ (Figure 30).[99] The olefins in the α-form were separated by 3.6-4.1 Å and were photoreactive to give α-truxillic acid as the photoproduct. The β-form is a metastable phase with the olefins separated by 3.6-4.1 Å and yielded only β-truxinic acid at low temperatures. A combination of α-truxillic acid and β-truxinic acid is obtained for the β-form at higher temperatures due to a phase change.[100] The γ-form has olefins separated by 4.7-5.1 Å and upon exposure to UV light, no photodimerization occurs. From these observations, Schmidt postulated that in order for a photoreaction to occur in the solid state the olefins must be separated by less than 4.2 Å. Further studies have led to the observation that the olefins must be parallel to be photoreactive in a solid.

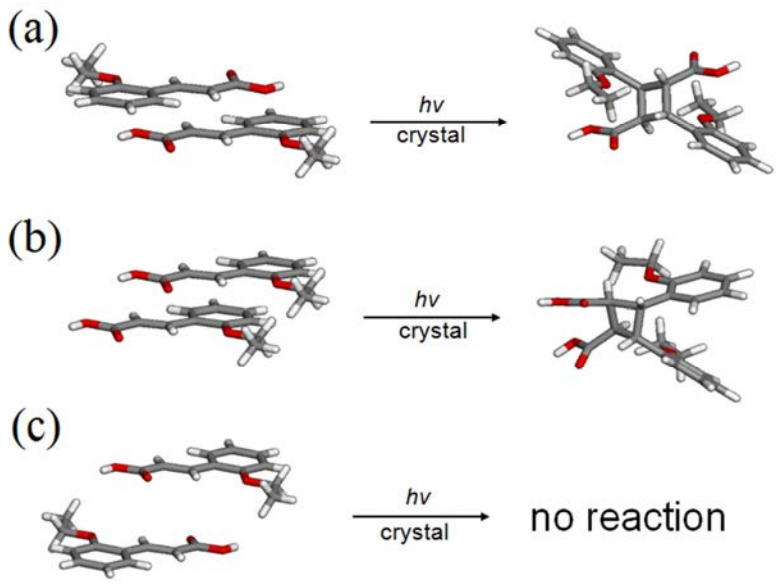

Figure 30: Classes of cinnamic acid derivatives and photo product yield A) α-class yielded α-truxillic acid photoproduct B) β-class yielded β-truxinic acid photoproduct and C) γ-class no photoreaction.

2.4.2 Single-crystal to single-crystal reaction (SCSC)

Solid-state reactions that occur without disruption of the crystal lattice are termed SCSC reactions. A proposed mechanism for heterogeneous solid-state reaction is three-steps: 1) phase rebuilding, 2) phase transformation, and 3) crystal disintegration.[101] In a SCSC reaction crystal disintegration does not occur. The lack of crystal disintegration is derived from the minimal motion of atoms in the reactions.[88] Despite the lack of crystal disintegration, the physical properties of the crystal can change.[102,103] Kohler *et.al.* were able to create a periodic spatial distribution of a monomer and dimer from a [2+2] photodimerization extending the length of the crystal through a SCSC reaction.[103] The ability to alter the physical properties could allow for creating preferred charge transport pathways in a single crystal which could potentially improve charge mobility. Indeed,

our group has shown that the fluorescence properties of a single crystal can be altered through [2+2] photodimerization.[104]

2.5 Two Component Thin Films

Organic thin films from conjugated organic molecules are promising for OLEDs, OTFTs, and organic photovalic devices (OPDs).[105] It has been established that the solid-state packing of organic semiconductors plays a key role in the charge transport process.[28,31] However, the ability to transfer the long range organization achieved in the single crystal to thin films has been difficult. Mobilities of single crystals of rubrene have achieved mobilities in excess of 15 $cm^2V^{-1}s^{-1}$ at room temperature. However, rubrene does not readily form crystalline thin films, which makes achieving high mobility films difficult.[106] A potential approach to overcome the problem is the addition of a second component to the aid in the formation of a crystalline thin film.

Thus far, two component thin films have consisted of blends of two polymers or of a polymer with small molecules.[107-109] Creating a thin film of a polymer and small molecule is difficult owing to differences in entropy and enthalpy between the polymer and small molecule. The differences can often lead to phase separation after some period of time.[110] In the examples which have created polymer small molecule blends, intermolecular forces, such as hydrogen bonds, have been used to help organize the blends into an ordered system.[107,111] The use of hydrogen bonds has allowed for the alignment of molecules in the thin film for solid-state reactions. The solid-state reactions have allowed for adjustment of the properties of thin films through photolithography. In one example, a spin-coated thin film consisted of aligned diacetylene monomers. The diacetylene monomers contained a carboxylic acid and were aligned *via* hydrogen bonds to poly(4-vinylpyridine) (Figure 31). Following fabrication, photopolymerization of the aligned diacetylene was performed.[111] The use of two small molecules instead of a polymer in combination with small molecules overcomes the phase separation problem.

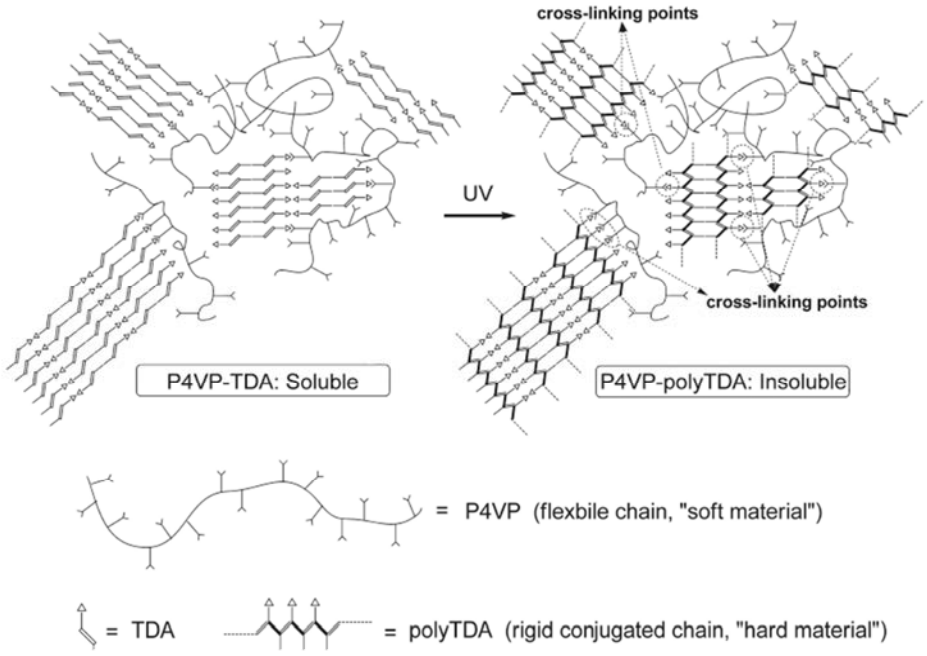

Figure 31: Scheme for hydrogen bonded complex before and after photoreaction. Reprinted with permission of Macromolecules.[111]

2.6 Chapter focus

The focus of this chapter is the use of resorcinol-based templates to direct the [2+2] photoreaction of building blocks of organic semiconductors in the solid state. In particular, a single vinyl pyridine group was fixed onto either a monothiophene or naphthalene and subjected to co-crystallization with a variety of co-crystal formers. The compounds studied are *trans*-1-(4-pyridyl)-2-(2-thienyl)ethylene (α-PTE), *trans*-1-(4-pyridyl)-2-(3-thienyl)ethylene (β-PTE), and *trans*-1-(2-naphthyl)-2-(4-pyridyl)ethylene (NPE) (Figure 32a, b and c). After co-crystallization, the resulting co-crystals were irradiated with UV light to determine photoreactivity. It is envisioned that the formation of the co-crystalline assembly will lead to improved π-overlap of the semiconductor building block, which should lead to improved charge transport for small molecules. Dimerization of the assembly should then not only shorten the π-conjugated distance, but

also drive the thiophene further apart to decrease the π-overlap to affect charge transport properties of the materials (Figure 32d). The process is projected to allow for the patterning of thin films of organic semiconductors by photolithography. If the reaction occurs *via* SCSC reaction, then a means to pattern a single crystal, which would allow for higher mobilities than those seen in thin film, may be achieved. Systematic studies of [2+2] photoreactions of thiophenes have not been reported in the solid state.

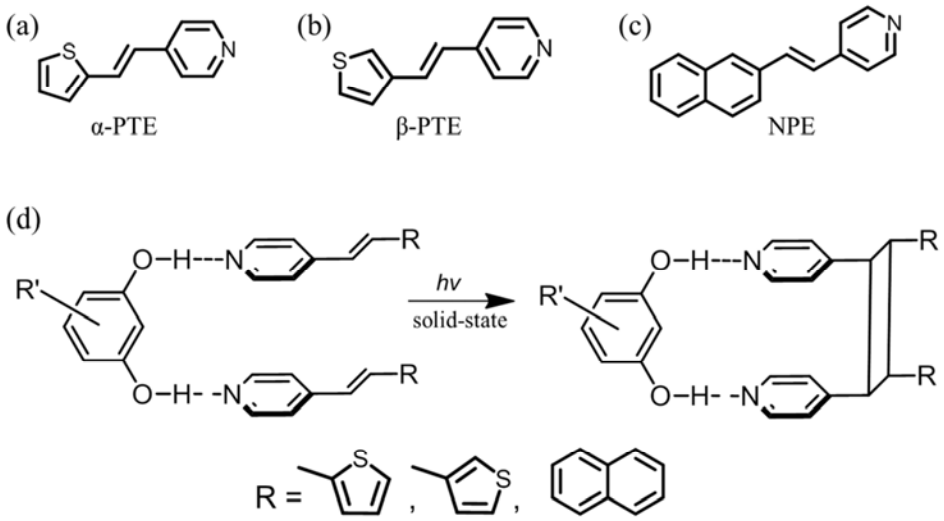

Figure 32: Compounds studied for photoreactivity a) α-PTE, b) β-PTE, c) NPE, and d) scheme for solid-state photoreactivity.

Thus, far resorcinol based SCCFs using O-H···N interactions have been used as a means to achieve a π-stacked arrangement. In order to generate possible alternate packing motifs, a different well-known heterosynthon was also explored for use as an interaction for SCCFs. Specifically, the COOH···N interaction was studied as a possible supramolecular interaction between a SCCF and a semiconductor building block (SBB). To this extent, carboxylic acid-based SCCFs with one or two carboxylic acids moieties were co-crystallized with α-PTE, β-PTE, and NPE to generate assemblies to achieve

different crystal packing motifs (Figure 33). It was found that benzoic acid and succinic acid formed co-crystals with β-PTE. The solid of 2(β-PTE)·(succinic acid) underwent a [2+2] photoreaction, and was found to yield a different stereoisomer of the photoproduct of β-PTE.

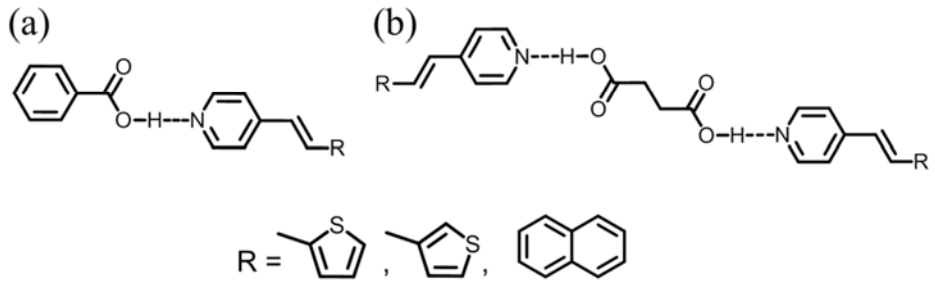

Figure 33: Schematic of 0-D assembly with a) benzoic acid and b) succinic acid.

In addition to single crystals, the chapter will focus on the ability to use template directed [2+2] photoreactions to pattern thin films. Thin films were fabricated using 4,4´-bis(4-pyridyl)ethylene (4,4´-BPE) and a phloroglucinol as the CCF (Figure 34).[112] A co-crystal former that contains an alkyl chain was used to form a two component thin film. The resulting thin film was then covered with a photomask and exposed to UV light. Development by solution methods allowed for micron sized features to be obtained. Advantages of using small molecules are expected to overcome the phase separation problem encountered with polymers and small molecules. It is expected that the thin film could be used as a photoresist due to its UV adsorption properties.

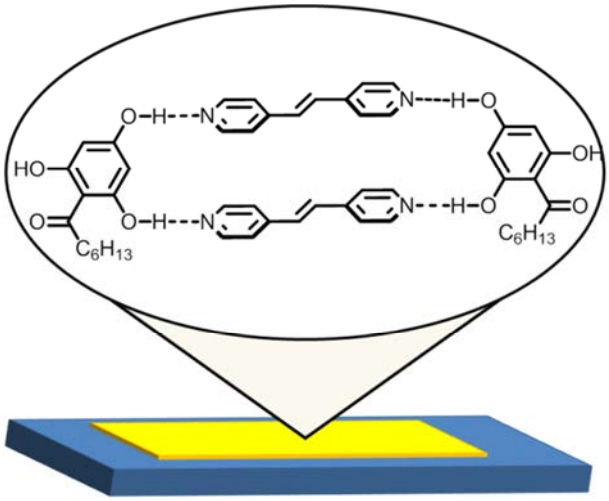

Figure 34: Proposed two-component thin film consisting of 0-dimensional hydrogen-bonded assemblies.

2.7 Photoreactions of thiophenes and naphthalene

2.7.1 Thiophenes

Very few photoreactions involving thiophene rings in solution or the solid state have been reported. In 1970 Wynberg *et.al.*, reported that 1,2-dithienylethenes and 2-styrylthiophene do not undergo photochemical dimerization to yield a cyclobutane product in solution.[113] Since that time, several groups have studied additional thiophenes that undergo photodimerization (Table 2).

In 1982, Costanzo et al. discovered that photodimerization only occurred for α-phenyl-β-(2-thienyl)-acrylonitrile when irradiated above 405 nm in solution. Irradiation at lower wavelengths resulted in reversible *trans-cis* photoisomerization.[114] It was hypothesized that irradiation at wavelengths above 405 nm did not supply enough energy for *trans-cis* photoisomerization to occur allowing for photodimerization. Scarlata *et.al.* increased the percent yield of the photoreaction of α-phenyl-β-(2-thienyl)-acrylonitrile to 88% yield by irradiation under a sunlamp for five days.[115] In 1997, Auria *et.al.*

Table 2: Photoreactions of thiophenes and naphthalenes

Compound	Photoreactivity	Ref
Thiophene compounds		
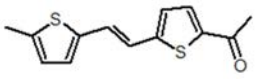	0 % (solid), 45 % (solution)	116
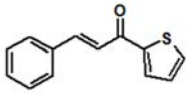	10 % (solution)	113
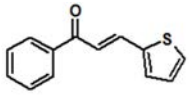	6 % (solution)	113
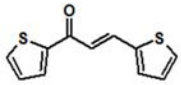	63 % (solution)	113
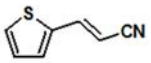	12 % (solution)	116
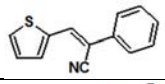	88 % (solid)	114, 115
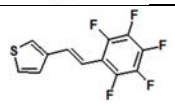	100 % (solid)	117
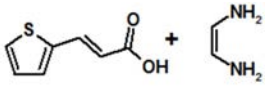	13 % (solid)	118
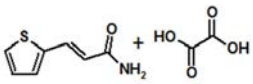	3 % (solid)	119
Naphthalene compounds		
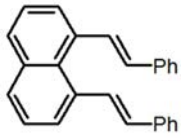	90 %	122
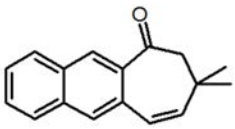	57 %	121
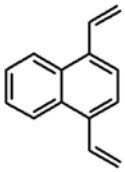	0 %	123

Table 2 Continued

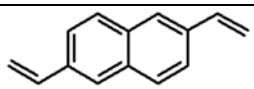	20 %	123
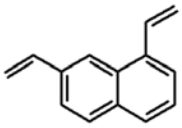	15 %	123
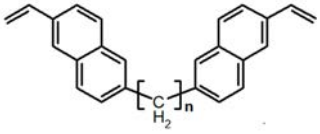	n = 3, 79 % n = 4, 32 %	124
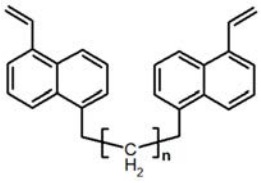	n = 3, 58 % n = 4, 64 %	125

studied the photocyclization of 3-(2-thienyl)acrylonitrile in solution. After 72 hours of irradiation with a 125 W high-pressure mercury lamp, only 12% photoreaction occurred. The yield was lower than that obtained for 3-(2-furyl)acrylonitrile which occurred in 82% yield in 48 hours.[116] Recently, the first report of a photoreaction with a beta-substituted thiophene was demonstrated in quantitative yield. The head-to-tail photoproduct was obtained for (E)-1-2′-5′-dibromo-3′-thienyl-2-pentafluoro-phenylethene after 24 hrs of UV irradiation at 340 nm.[117]

The first attempt to use two-component crystals to obtain the photodimerized product with thiophene derivatives was performed by Ito. Salts were created by precipitation of a solution of *trans*-(2-thienyl)-acrylic acid and ethylenediamine. Upon irradiation for 10 hours with a 400 W high-pressure mercury lamp, 13% photoreaction was obtained.[118] In another attempt, ethanedioic acid was precipitated with *trans*-β-(2-thienyl)-acrylamide as a salt. After irradiation for 20 h with a 400 W high-pressure

mercury lamp only a 3% yield was obtained.[119] Table 2 provides a list of photoreactions involving thiophenes.[120]

2.7.2 Naphthalene

Photodimerization reactions involving naphthalene have been studied since the late 1960s.[121,122] There have been extensive studies on the photoreactivity of divinylnaphthalene for the purpose of forming naphthalenophanes. When 1,4-, 1,5-, and 1,6-divinylnaphthalene were irradiated with UV light in benzene, a polymer material was produced.[123] A naphthalenophane was produced in 8, 15, 18, 20, and 27 % yields when 1,3-, 1,7-, 2,3-, 2,6-, and 2,7-divinylnaphthalene were exposed to UV light, respectively.[123] A dimer was formed during the photoreaction of 1,8-distyrylnaphthalene with both double bonds reacting.[122] Formation of cyclobutanes from vinylnaphthalene was also seen in the irradiation of several other compounds listed in Table 2.[124,125] All of the reported photoreactions involving vinylnaphthalene were conducted in solution. There have been no reported [2+2] photoreactions of a vinylnaphthalene in the solid state.

2.8 Experimental Procedure

2.8.1 Synthesis of α-PTE

Trans-1-(4-pyridyl)-2-(2-thienyl)ethylene (α-PTE) was synthesized according to the following procedure. A round-bottom flask was charged with 2-iodothiophene (2.0 g, 9.5 mmol), distilled 4-vinylpyridine (1.2g, 11.4 mmol), $PdCl_2(PPh_3)_2$ (332 mg, 5 mol %), anhydrous potassium carbonate (3.9 g, 28.5 mmol), 20 ml dimethylformamide. The solution was refluxed overnight. The solution was then poured onto ice and subsequently extracted with chloroform. The chloroform layer was washed with brine and dried with $MgSO_4$. The organic solvent was reduced to afford dark solid. The solid was further purified via column chromatography using silica powder and a 2:1 mixture of tetrahydrofuran to hexane as an eluent. Evaporation of the solvent yielded a yellow solid

confirmed to be α-PTE by ^{1}H NMR spectroscopy and ^{13}C NMR spectroscopy. ^{1}H NMR data for α-PTE ($CDCl_3$, 300 MHz): δ 8.55- 8.59 (2H's, dd, pyridine), δ 7.39-7.47 (1H, d, ethylene), δ7.26-7.34 (3H's, m, pyridine, thiophene), δ 7.15-7.18 (1H, d, thiophene), δ 7.02-7.07 (1H, dd, thiophene), δ 6.79-6.87 (1H, d, ethylene). ^{13}C NMR data for α-PTE ($CDCl_3$, 400 MHz) δ 150.20, 144.28, 141.59, 127.94, 127.85, 126.04, 125.31, 120.54.

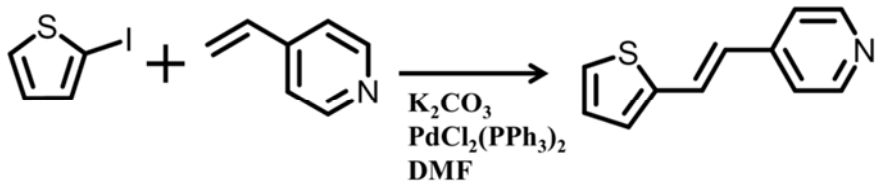

Figure 35: Synthesis of α-PTE.

2.8.2 Synthesis of β-PTE

Trans-1-(4-pyridyl)-2-(3-thienyl)ethylene (β-PTE) was synthesized according to the following procedure. A round-bottom flask was charged with 3-bromothiophene (4.0 g, 24 mmol), distilled 4-vinylpyridine (2.73 g, 26 mmol), $PdCl_2(PPh_3)_2$ (504 mg, 3 mol %), anhydrous potassium carbonate (5.0 g, 36 mmol) in 40 mL dimethylformamide. The solution was refluxed overnight. The resulting mixture was poured onto ice and extracted with dichloromethane. The organic layer was washed with brine and dried with $MgSO_4$. The organic solution was evaporated to give a solid which was recrystallized from toluene to give clean β-PTE (1.18 g, 28 % yield) verified by ^{1}H NMR spectroscopy and ^{13}C NMR spectroscopy. ^{1}H NMR data for β-PTE ($CDCl_3$, 300 MHz) δ 8.53-8.58 (2H's, dd, pyridine), δ 7.30-7.39 (5H's, m, ethylene, thiophene, pyridine), δ 7.24-7.29 (1H, d, thiophene), δ 6.81-6.89 (1H, d, ethylene). ^{13}C NMR data for β-PTE ($CDCl_3$, 400 MHz) δ 150.17, 144.72, 139.08, 127.10, 126.69, 125.86, 124.83, 124.54, 120.63.

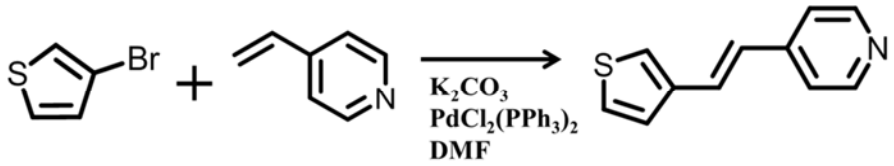

Figure 36: Synthesis of β-PTE.

2.8.3 Synthesis of NPE

Trans-1-(2-naphthalene)-2-(4-pyridyl)ethylene (NPE) was synthesized according to the following procedure. A round-bottom flask was charged 2-bromonaphthalene (2.0 g, 9.6 mmol), distilled 4-vinylpyridine (1.05 g, 10 mmol), $PdCl_2(PPh_3)_2$ (338 mg, 5 mol %), anhydrous potassium carbonate (4.0 g, 29 mmol) in 30 mL dimethylformamide. The solution was refluxed overnight. The resulting mixture was poured onto ice and the solid was filtered. The filtered solid was recrystallized from hot toluene and confirmed to be NPE by ^{1}H NMR spectroscopy and ^{13}C NMR spectroscopy. ^{1}H NMR data for NPE ($CDCl_3$, 300 Mhz): δ 8.60-8.63 (2H's, dd, pyridine), δ 7.92-7.94 (1H, s, naphthalene), δ 7.83-7.89 (3H's, m, naphthalene), δ 7.74-7.78 (1H, dd, naphthalene), δ 7.45-7.53 (3H's, m, ethylene, naphthalene), δ 7.41-7.44 (2H's, dd, pyridine), δ 7.13-7.19 (1H, d, ethylene). ^{13}C NMR data for NPE ($CDCl_3$, 400 MHz) δ 150.18, 144.67, 133.61, 133.54, 133.27, 128.59, 128.45, 128.22, 126.56, 126.21, 123.34, 120.87.

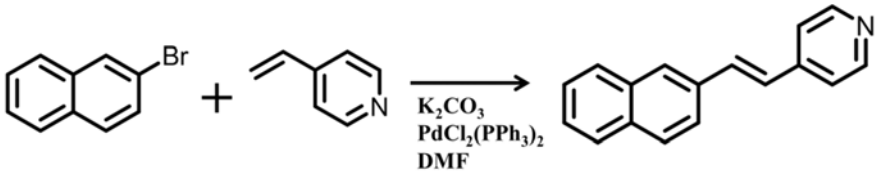

Figure 37: Synthesis of NPE.

2.8.4 Crystal growth

Single crystals of α-PTE were obtained *via* vacuum sublimation. Co-crystallization experiments with α-PTE were conducted by adding α-PTE and an appropriate SCCF in a screw-cap vial in a 2:1 ratio. A minimum amount of solvent was added such that all solids would dissolve when heated. If no crystals were obtained upon cooling, the cap was removed such that the solvent could evaporate. For initial screening, 8 mg of α-PTE were dissolved with an SCCF in a 2:1 ratio in approximately 4 mL of solvent. Crystal structures of co-crystals involving 4,6-diiodoresorcinol (4,6-diI-Res), 4,6-dibromorescorcinol (4,6-diBr-res), 4,6-dichlororescorinol (4,6-diCl-res), and 3,5-dihydroxyacetaphenone (5-acetyl-Res) using acetonitrile as a solvent were collected and solved.

Single crystals of β-PTE were obtained from slow evaporation of toluene at room temperature. As with α-PTE, co-crystallization experiments with β-PTE were carried out by adding β-PTE and an appropriate SCCF in a screw-cap vial in a 2:1 ratio. Co-crystals involving 4,6-diI-res and 4,6-diCl-res using acetonitrile as a solvent had crystal structures solved. Crystal structures were also solved for co-crystals using succinic acid and benzoic acid as the SCCF and tetrahydrofuran as a solvent.

Single crystals of NPE were obtained from slow evaporation of acetonitrile. Co-crystallization experiments with NPE were carried out by adding NPE and an appropriate SCCF in a screw-cap vial in a 2:1 ratio. Co-crystals involving 4,6-diI-res, 4,6-diBr-res, and 4,6-diCl-res were obtained using acetonitrile as a solvent.

Single crystals of the photoproduct of 2(α-PTE)·(4,6-diI-res) were obtained by dissolving the reacted powder in a boiling 1:1:1 acetonitrile to toluene to methanol solution. Once the reacted solid had dissolved, the solution was allowed to evaporate at room temperature until single crystals formed. Single crystals of the photoproduct of 2(β-PTE)·(4,6-diI-res) were obtained in the same manner.

The following single crystal structures have been obtained: α-PTE, 2(α-PTE)·(4,6-diI-res), 2(α-PTE)·(4,6-diBr-res), 2(α-PTE)·(4,6-diCl-res), (α-PTE)·(5-acetyl-res), β-PTE, 2(β-PTE)·(4,6-diI-res), 2(β-PTE)·(4,6-diCl-res), 2(β-PTE)·(succinic acid), (β-PTE)·(benzoic acid), 2(NPE)·(4,6-diI-res), 2(NPE)·(4,6-diBr-res), and 2(NPE)·(4,6-diCl-res).

2.8.5 X-ray crystallography

All crystal data were taken on a Nonius Kappa CCD single-crystal X-ray diffractometer at room or liquid N_2 temperature using MoK_α radiation (λ = 0.7107 Å). The structures were solved and refined by full-matrix lease-squares based on F^2 parameter. All non-hydrogen atoms were refined using the anisotropic model. H-atoms bonded to C-atoms were placed in idealized positions based on the hybridization of the belonging C-atom. H-atoms bonded to O-atoms were based on calculations to establish hydrogen bonds to the nearest neighbor hydrogen bond acceptor. Structure solution was accomplished with the aid of WinGX and refinement was conducted using SHELXL-97 locally implemented on a Pentium-based IBM compatible computer.[126] Relevant crystallographic data for all structures described within this chapter are present in the appendix in Tables A-1 through A-6.

2.8.6 Photodimerization

All co-crystals of 2(SBB)·(SCCF) and pure SBB were examined for [2+2] photoreactivity. In particular, 50 mg of solid was placed between two glass plates and exposed to broadband or 350 nm UV radiation. The formation of a cyclobutane ring was studied by ^{1}H NMR spectroscopy. The photoreactions were monitored by the decreased intensity of the olefin peaks and general emergence of peaks between 4 to 5 ppm indicating the formation of the cyclobutane product.

^{1}H NMR data for product of 2(α-PTE)·(4,6-diI-res) after photoreaction ($CDCl_3$, 300 MHz): δ 8.28-8.52 (4H's, bs, pyridine), δ 7.24-7.29 (2H's, d, thiophene), δ 7.34-7.38

(2H's, dd, thiophene), δ 7.20-7.33 (4H's, bs, pyridine), δ 7.07-7.13 (2H's, m, thiophene), δ 6.95-7.00 (2H's, dd, thiophene), δ 4.78-4.83 (2H's, m, cyclobutane), δ 4.53-4.58 (2H's, m, cyclobutane).

^{1}H NMR data for product of (α-PTE)·(5-acetyl-res) after photoreaction ($CDCl_3$, 300 MHz): δ 8.35-8.50 (4H's, bs, pyridine), δ 7.23-7.38 (6H's, m, pyridine, thiophene), δ 7.00-7.06 (2H's, dd, thiophene), δ 6.88-6,94 (2H's, m, thiophene), δ 4.84-4.85 (2H's, dd, cyclobutane), δ 4.40-4.53 (2H's, dd, cyclobutane).

^{1}H NMR data for product of 2(β-PTE)·(4,6-diI-res) after photoreaction ($CDCl_3$, 300 MHz): δ 8.26-8.49 (4H's, bs, pyridine-product), δ 7.35-7.42 (2H's, m, thiophene), δ 7.29-7.34 (2H's, m, thiophene), δ 7.19-7.27 (4H's, bs, pyridine), δ 6.92-6.95 (2H's, m, thiophene), δ 4.52-4.60 (4H's, s, cyclobutane).

^{1}H NMR data for product of 2(β-PTE)·(succinic acid) after photoreaction ($CDCl_3$. 300 MHz): δ 8.50-8.35 (4H's, dd, pyridine), δ 7.13-7.21 (2H's, dd, thiophene), δ 7.01-7.12 (4H's, dd, pyridine), δ 6.93-7.00 (2H's, s, thiophene), δ 6.70-6.80 (2H's, d, thiophene), δ 4.54-4.64 (2H's, dd, cyclobutane), δ 4.26-4.36 (2H's, dd, cyclobutane).

2.8.7 Computational studies

The HOMO and LUMO energies levels were calculated using density functional theory (DFT) (b3lyp 6-31G*) with the aid of Spartan 08 implemented on a Pentium-based Dell computer.

2.8.8 Thin film formation

A 1:1 molar solution of 4,4′-BPE and 1-(2,4,6-trihydroxyphenyl)-1-heptanone (HP) (9 mg/ml) dissolved in a 1:1 isopropanol and 1,3-dichlorobenzene solution was used to make the thin films. A spin coater from Laurell Technologies Corp. (Model no.-WS-650SZ-6NPP/LITE) was used to prepare thin films on glass slide. To prepare the thin films, two drops of the prepared solution was placed on a glass slide and spin coater was set to spin for a time of 1 minute with a rotation speed of 1000 rpm. The thin films

images were done by Suman Ghoria in collaboration with Dr. Alexei Tivanski at the University of Iowa. Images were collected in AC mode using a commercial Atomic Force Microscope (Asylum Research, MFP3D) with a Si_3N_4 tip (MikroMasch, tip radius of curvature: ~10 nm).

The thin films were photoreacted by irradiation with UV light generated from a broadband 400 W medium pressure mercury lamp. The thin films were placed in a black box constructed from black construction paper to limit UV exposure from directions other than the top. A piece of borosilicate glass was used to filter UV light below 300 nm (Figure 38). To pattern a thin film, a photomask with 10 μm spacers was placed on top of the thin film inside the black box and exposed to UV light for 2 hours. Irradiated thin films were developed in 2:1 pentane to ethyl ether solution. To confirm a [2+2]

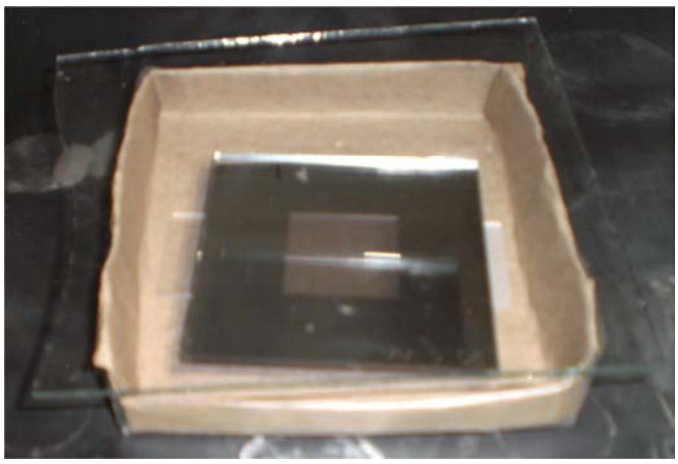

Figure 38: Apparatus for UV irradiation of thin film with photomask.

photodimerization the thin films were analyzed by electron spray ionization mass spectrometry (ESI-MS) using a solution of 1:1 water to acetonitrile with 0.1 % formic acid and by ^1H NMR spectroscopy on a Brunker Advance 400 NMR instrument in DMSO-d_6.

2.9 Results and Discussion

2.9.1 Single crystal structures involving α-PTE

2.9.1.1 Crystal structure of α-PTE

Single crystals of α-PTE were obtained by vacuum sublimation as colorless prisms. α-PTE crystallized in the monoclinic space group Pc and is directed into a herringbone packing motif by C-H···π interactions (Figure 39). The herringbone packing exhibits an angle of 63°, similar to what is seen in unsubstituted oligothiophenes.[32] The

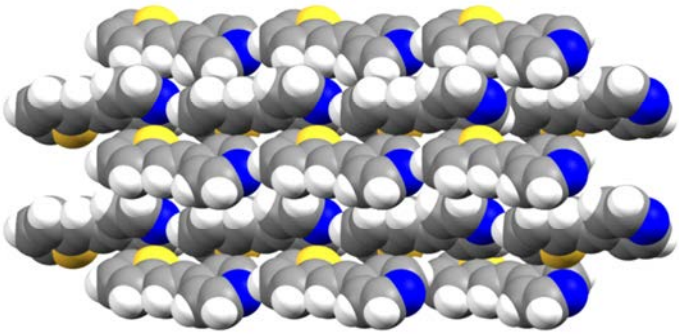

Figure 39: Crystal structure of α-PTE viewed down *a*-axis.

asymmetric unit contains one molecule, which exhibits a disorder in which the molecule is rotated 180 degrees along an axis connecting the N-atom to the C_5-atom of the thiophene ring. The molecule is planar, with a twist of 6° between the mean plane of the thiophene ring and the mean plane of the pyridine ring.

2.9.1.2 Co-crystals of α-PTE

A total of four co-crystals involving α-PTE were obtained. Specifically, crystals were collected with 4,6-diI-res, 4,6-diBr-res, 4,6-diCl-res, and 5-acetyl-res as the SCCF. Three co-crystals displayed discrete hydrogen-bonded assemblies and one displayed an 1-

D hydrogen-bonded polymer. The hydrogen bond distances for all co-crystals are summarized in Table 3.

Table 3: Interatomic distances and angles for co-crystals involving α-PTE

SCCF	O···N Bond (Å)	C=C distances in assemblies (Å)	Thiophene Pyridine twist angle (°)
4,6-diI-res	2.68(2), 2.65(2), 2.704(8), 2.681(7)	4.2 4.2	2.8, 8.8 8.0, 7.0
4,6-diBr-res	2.72(1), 2.69(1), 2.64(1), 2.82(2), 2.75(1), 2.71(1), 2.75(1), 2.66(2)	4.2 4.2 4.5 4.5	24.2, 14.6 3.5, 10.3 4.0, 9.3 1.9, 23.0
4,6-diCl-res	2.764(3), 2.728(2)	4.1	7.2, 0.6
5-acetyl-res	2.708(7)	8.2	10.3

2.9.1.2.1 Co-crystal of 2(α-PTE)·(4,6-diI-res)

Co-crystallization of α-PTE with 4,6-diI-res afforded crystals as orange blades with a 2:1 ratio of α-PTE to 4,6-diI-res in the monoclinic space group $P2_1$. The asymmetric unit contains four α-PTE molecules and two 4,6-diI-res molecules. The six molecules create two discrete assemblies of two α-PTE molecules and one 4,6-diI-res through O-H···N hydrogen bonds [O···N separations (Å): (O_1···N_1) 2.68(2), (O_2···N_2) 2.65(2), (O_3···N_3) 2.704(8), (O_4···N_4) 2.681(7)]. In one assembly, labeled 2(α-PTE)·(4,6-diI-res)-a, the mean plane of the two α-PTE molecules exhibit an angle of 16° between them. In the other assembly, 2(α-PTE)·(4,6-diI-res)-b, the mean planes of the α-PTE molecules exhibit a 28° angle (Figure 40a and b). Both angles within an assembly are less than the 62° exhibited between the planes in the crystal structure of pure α-PTE. All α-PTE molecules are relatively planar, with the largest internal twist between the thiophene and pyridine of one molecule being of 8° and the smallest being 2°. The double bonds within each assembly are aligned with the C=C distances of 4.2 Å, which fits the topochemical postulate. I···O interactions[127] [I···O separation (Å): (O_1···I_1) 3.432, (O_3···I_4) 3.405] between adjacent SCCF's further direct the discrete assemblies into 1-D assemblies that consist of either only 2(α-PTE)·(4,6-diI-res)-a or 2(α-PTE)·(4,6-diI-res)-b

(Figure 40c). The α-PTE molecules are aligned into 1-D columns with a distance of 5.6 Å separating the ethylene moieties of neighboring assemblies in columns, consisting of α-PTE-a and 5.4 Å in columns consisting of α-PTE-b. The chirality of the structure arises from all assemblies of 2(α-PTE)·(4,6-diI-res)-a aligning in one direction along the *b*-axis and all assemblies of 2(α-PTE)·(4,6-diI-res)-b pointing in the opposite direction.

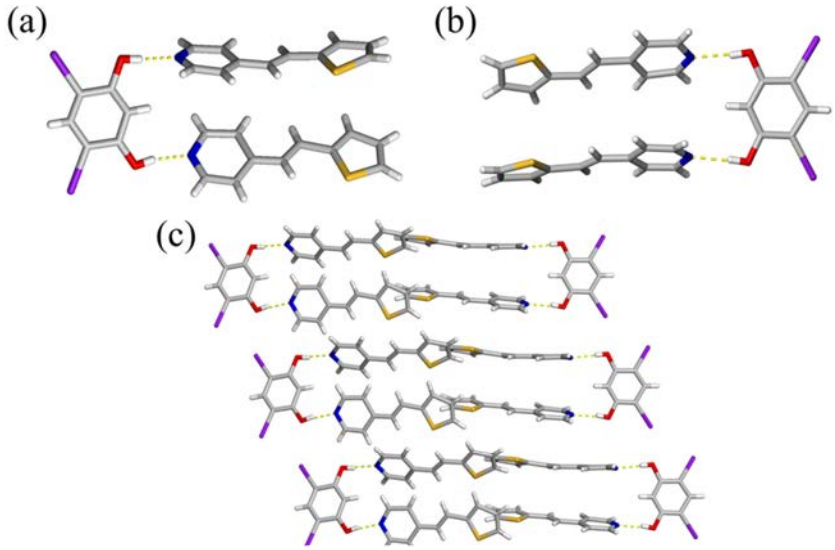

Figure 40: Crystal structure of 2(α-PTE)·(4,6-diI-res) a) assembly 2(α-PTE)·(4,6-diI-res)-a, b) 2(α-PTE)·(4,6-diI-res)-b, and c) crystal packing viewed down *c*-axis.

2.9.1.2.2 Co-crystal of 2(α-PTE)·(4,6-diBr-res)

Co-crystallization of α-PTE with 4,6-diBr-res afforded colorless plates with a 2:1 ratio of α-PTE to 4,6-diBr-res in the monoclinic space group $P2_1$. The asymmetric unit contains eight α-PTE molecules and four 4,6-diBr-res. The twelve molecules create four different discrete assemblies of two α-PTE and one 4,6-diBr-res bonded through O-H···N hydrogen bonds [O···N separations (Å): (O_1···N_1) 2.72(1), (O_2···N_2) 2.69(1), (O_3···N_3) 2.64(1), (O_4···N_4) 2.82(1), (O_5···N_5) 2.75(1), (O_6···N_6) 2.71(1), (O_7···N_7) 2.75(1), (O_8···N_8) 2.66(2)] (Figure 41). In assembly 2(α-PTE)·(4,6-diBr-res)-a, the mean planes of

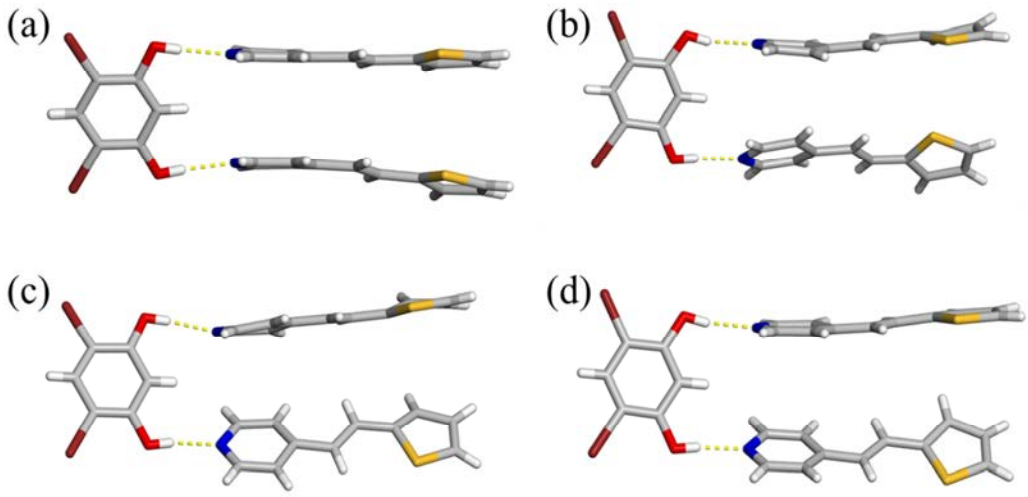

Figure 41: Assembly a) 2(α-PTE)·(4,6-diBr-res)-a b) 2(α-PTE)·(4,6-diBr-res)-b, c) 2(α-PTE)·(4,6-diBr-res)-c and d) 2(α-PTE)·(4,6-diBr-res)-d.

the α-PTE molecules are at an angle of 6^{o} and in assembly 2(α-PTE)·(4,6-diBr-res)-b the mean planes are twisted at an angle of 29^{o}. In assembly 2(α-PTE)·(4,6-diBr-res)-c and 2(α-PTE)·(4,6-diBr-res)-d the two α-PTE molecules exhibit 35^{o} and 46^{o} angles, respectively. In 2(α-PTE)·(4,6-diBr-res)-a, the olefins are aligned and separated by 4.2 Å, and in 2(α-PTE)·(4,6-diBr-res)-b the olefins separated by 4.2 Å and are aligned. In 2(α-PTE)·(4,6-diBr-res)-c and 2(α-PTE)·(4,6-diBr-res)-d the olefins are both separated by 4.5 Å. Hence, only half of the assemblies in the co-crystal meet the topochemical postulate. The assemblies pack such that there are C-H$\cdots\pi$ interactions between α-PTE molecules in neighboring assemblies causing no extended π-overlap within the crystal (Figure 42).

Figure 42: Crystal packing of 2(α-PTE)·(4,6-diBr-res) viewed down *c*-axis.

2.9.1.2.3 Co-crystal of 2(α-PTE)·(4,6-diCl-res)

Co-crystallization of α-PTE with 4,6-diCl-res afforded colorless blades with a ratio of 2:1 α-PTE to 4,6-diCl-res in the monoclinic space group $P2_1/c$. The asymmetric unit consists of two α-PTE molecules and one 4,6-diCl-res. The molecules are arranged into discrete assemblies through O-H···N hydrogen bonds [O···N separation (Å): (O_1···N_1) 2.764(3), (O_2···N_2) 2.728(2)]. Within an assembly, the α-PTE molecules are aligned such that the mean planes lie parallel with the olefins separated by 4.1 Å. However, one of the α-PTE molecules is disordered, which causes the double bonds to be crossed within the assembly 40% of the time (Figure 43a). The assemblies are propagated throughout the crystal in a manner that alternates π-overlap between pyridyl and thienyl groups of neighboring assemblies (Figure 43b).

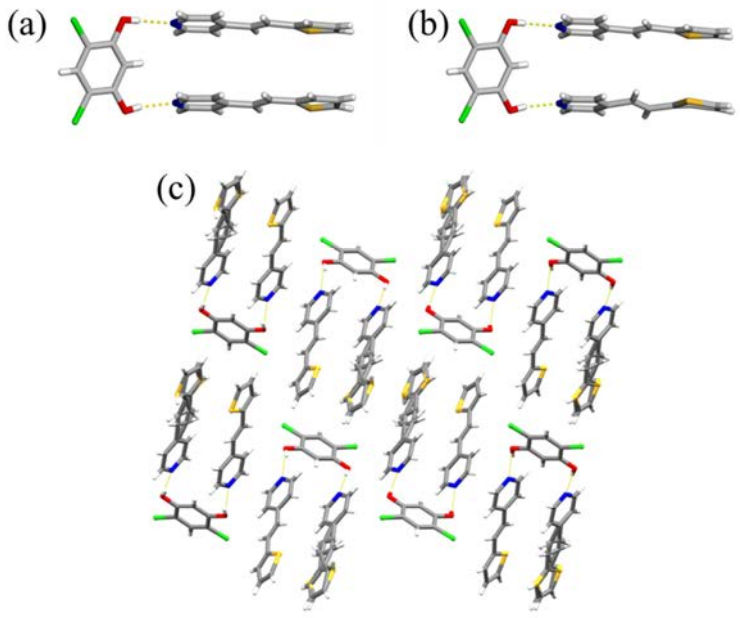

Figure 43: Crystal structure of 2(α-PTE)·(4,6-diCl-res) a) 60% occupancy assembly, b) 40% occupancy assembly and c) crystal packing viewed down *b*-axis.

2.9.1.2.4 Co-crystal of (α-PTE)·(5-acetyl-res)

Co-crystallization of α-PTE with 5-acetyl-res afforded yellow needles with a 1:1 ratio in the monoclinic space group $P2_1/c$. The crystal structure consists of 1-D assemblies propagated through O-H···O hydrogen bonds [$O_1\cdots O_3$ separation (Å): 2.685(6)] between a hydroxyl and carbonyl of neighboring 5-acetyl-res. The α-PTE molecules are bonded to the 1-D assembly through O-H···N hydrogen bonds [$O_2\cdots N$ separation (Å): 2.708(7)] creating an infinite row of α-PTE molecules (Figure 44). However, the α-PTE molecules in the row are edge-to-edge with no π-overlap in the assembly. The α-PTE molecules between neighboring rows are staggered causing little π-overlap between layers. The olefins between rows are separated by 5.4 Å and within a row by 8.2 Å, neither of which conforms to the topochemical postulate.

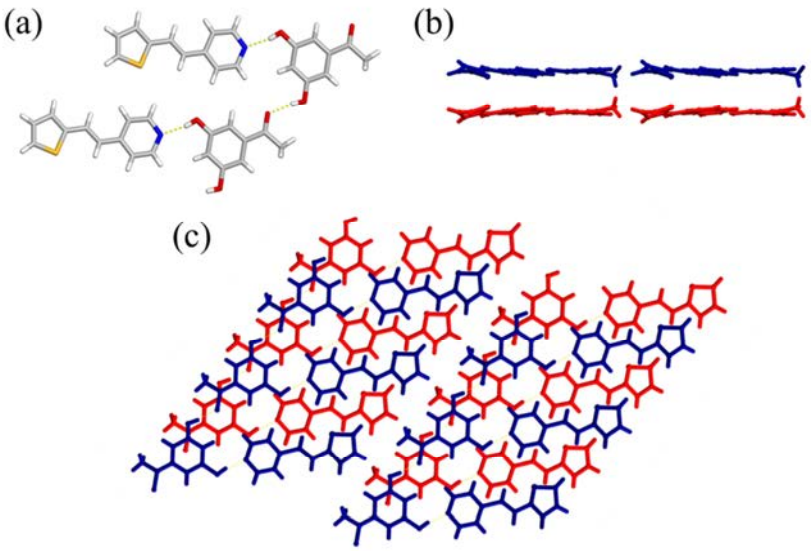

Figure 44: Crystal structure of (α-PTE)·(5-acetyl-res) a) 1-D assembly, b) packing viewed down *c*-axis, and c) packing viewed down *b*-axis.

2.9.2 Single crystal structures involving β-PTE

2.9.2.1 Crystal structure of β-PTE

Single crystals of β-PTE were grown by fast precipitation from toluene. The crystals obtained were colorless plates and β-PTE crystallized in the monoclinic space group Pc. One molecule is located in the asymmetric unit and it exhibits a disorder in which the β-PTE molecule is rotated by 180^{o} along its short axis such that the thiophene or pyridine occupies equivalent space. The molecules pack in a herringbone fashion with a 63^{o} angle between the mean planes, similar to that seen in unsubstituted α-oligothiophenes (Figure 45). The herringbone packing places the closest C=C bonds at a distance of 6.1 Å and unaligned making the compound photostable in the solid state.

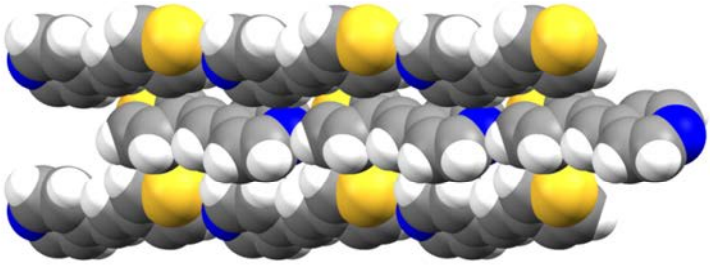

Figure 45: Crystal packing of β-PTE viewed down *a*-axis.

2.9.2.2 Co-crystal structures of β-PTE

A total of two co-crystals using β-PTE as the organic semiconductor were obtained. Specifically, crystals were collected with 4,6-diI-res, and 4,6-diCl-res acting as the SCCF. Both co-crystals displayed discrete hydrogen bonded assemblies. The hydrogen bond distances for the two co-crystals are summarized in Table 4.

Table 4: Interatomic distances and angles for co-crystals involving β-PTE

SCCF	O···N Bond Distances (Å)	C=C distances in assemblies (Å)	Thiophene-Pyridine twist angle(°)
4,6-diI-res	2.65(3), 2.72(1), 2.66(1), 2.68(1)	4.1 4.2	6.8, 12.4 4.3, 8.7
4,6-diCl-res	2.742(4), 2.705(4)	4.8	8.3, 15.3

2.9.2.2.1 Co-crystal of 2(β-PTE)·(4,6-diI-res)

Co-crystallization of β-PTE with 4,6-diI-res afforded orange blades with a 2:1 ratio of β-PTE to 4,6-diI-res in the monoclinic space group $P2_1$. The asymmetric unit contained six molecules, four β-PTE molecules and two 4,6-diI-res molecules. The six molecules pack to form two distinct discrete assemblies of two β-PTE molecules and one 4,6-diI-res through O-H···N hydrogen bonds [O···N separations (Å): (O_1···N_1) 2.65(3), (O_2···N_2) 2.72(1), (O_3···N_3) 2.66(1), (O_4···N_4) 2.68(1)]. One of the assemblies, labeled

2(β-PTE)·(4,6-diI-res)-a, the mean planes of the β-PTE molecules exhibit an angle of 32° and in the other assembly, 2(β-PTE)·(4,6-diI-res)-b, the mean plane of the β-PTE molecules exhibits an angle of 14° (Figure 46a and b). The assemblies are directed into 1-D columns through O···I interactions [O···I separation (Å): (O_1···I_1) 3.377, (O_3···I_3) 3.464] and each column consists of only one type of assembly (Figure 46c). In the

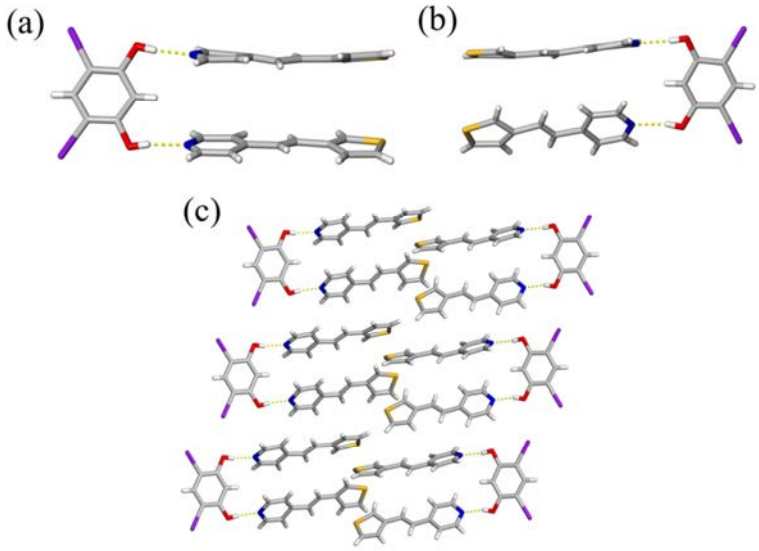

Figure 46: Crystal structure of 2(β-PTE)·(4,6-diI-res) a) assembly 2(β-PTE)·(4,6-diI-res)-a, b) assembly 2(β-PTE)·(4,6-diI-res)-b and c) crystal packing viewed down *c*-axis.

columns containing assembly 2(β-PTE)·(4,6-diI-res)-a, the C=C bonds are separated by 4.1 Å within the assembly and 5.6 Å between assemblies. In the columns containing the assemblies 2(β-PTE)·(4,6-diI-res)-b, the C=C bonds are separated by 4.2 Å within the assembly and 5.4 Å between assemblies. According to the topochemical postulate photoreaction should occur within an assembly. The chirality of the crystal is from all assemblies of 2(β-PTE)·(4,6-diI-res)-a pointing in one direction and all assemblies of 2(β-PTE)·(4,6-diI-res)-b pointing in the opposite direction along the *b*-axis.

2.9.2.2.2 Co-crystal of 2(β-PTE)·(4,6-diCl-res)

Co-crystallization of β-PTE with 4,6-diCl-res afforded rod shaped pale yellow crystals with a 2:1 ratio of β-PTE to 4,6-diCl-res in the triclinic space group $P\bar{1}$. The asymmetric unit contains one 4,6-diCl-res molecule and two β-PTE. The molecules form a discrete assembly through O-H···N hydrogen bonds [O···N separation (Å): (O_1···N_1) 2.742(4), (O_2···N_2) 2.705(4)]. Within the assembly, the mean planes of the β-PTE molecules exhibit an unusual angle of 67°, similar to what is observed in the pure compound (Figure 47a). The angle, being similar to pure β-PTE, suggests that C-H···π interactions dictated the arrangement of the β-PTE molecules within an assembly. The C=C bonds are not aligned and at a distance of 4.8 Å making the compound photostable. The edge-to-face packing is also seen between assemblies in the crystal structure (Figure 47b).

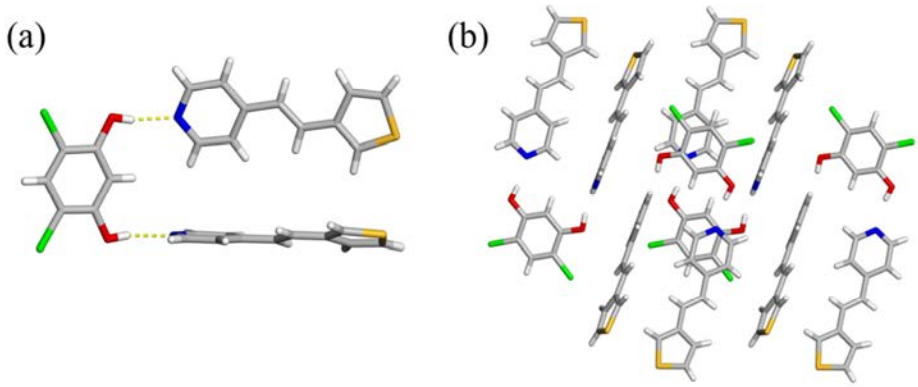

Figure 47: Crystal structure of 2(β-PTE)·(4,6-diCl-res) a) assembly and b) crystal packing viewed down *a*-axis.

2.9.3 Single crystal structures involving NPE

2.9.3.1 Co-crystal structures of NPE

A total of three co-crystals using NPE as the organic semiconductor building block were obtained. Specifically, crystals were collected with 4,6-diI-res, 4,6-diBr-res, and 4,6-diCl-res acting as the SCCF. All three of the co-crystals exhibited discrete hydrogen bonded assemblies. Moreover, 4,6-diI-res and 4,6-diBr-res yielded isostructural crystals when co-crystallized with NPE. The hydrogen bond distances for all co-crystals are summarized in Table 5.

Table 5: Interatomic distances and angles for co-crystals involving NPE

SCCF	O···N Bond Distance (Å)	C=C distances in assemblies (Å)	Pyridine-Naphthalene twist angle (^{o})
4,6-diI-res	2.72(1), 2.75(2)	4.9	7.3, 11.6
4,6-diBr-res	2.718(5), 2.777(5)	4.8	7.6, 12.1
4,6-diCl-res	2.696(5), 2.731(5)	4.8	5.1, 10.6

2.9.3.1.1 Co-crystal of 2(NPE)·(4,6-diBr-res) and 2(NPE)·(4,6-diI-res)

Co-crystallization of NPE with 4,6-diI-res or 4,6-diBr-res afforded colorless plates with a 2:1 ratio of NPE to SCCF in the monoclinic space group $Pca2_1$. The co-crystals are isostructural. The asymmetric unit contains two NPE molecules and one SCCF. The crystal structures consist of discrete assemblies in which two NPE molecules are hydrogen bonded to the SCCF through O-H···N hydrogen bonds [O···N separation (Å): 2(NPE)·(4,6-diBr-res) (O_1···N_1) 2.718(5), (O_2···N_2) 2.777(5), 2(NPE)·(4,6-diI-res) (O_1···N_1) 2.72(1), (O_2···N_2) 2.75(2)] (Figure 48a and b). The NPE molecules within a discrete assemble are directed into an edge-to-face fashion by C-H···π interactions. The mean planes of the NPE molecules in an assembly form a 57^o angle with 4,6-diBr-res as the SCCF and 59^o with 4,6-diI-res as the SCCF. The assemblies are stacked along the b-axis with a distance of 5.9 Å separating the centroids of stacked naphthalene units in both co-crystals (Figure 48c and d).

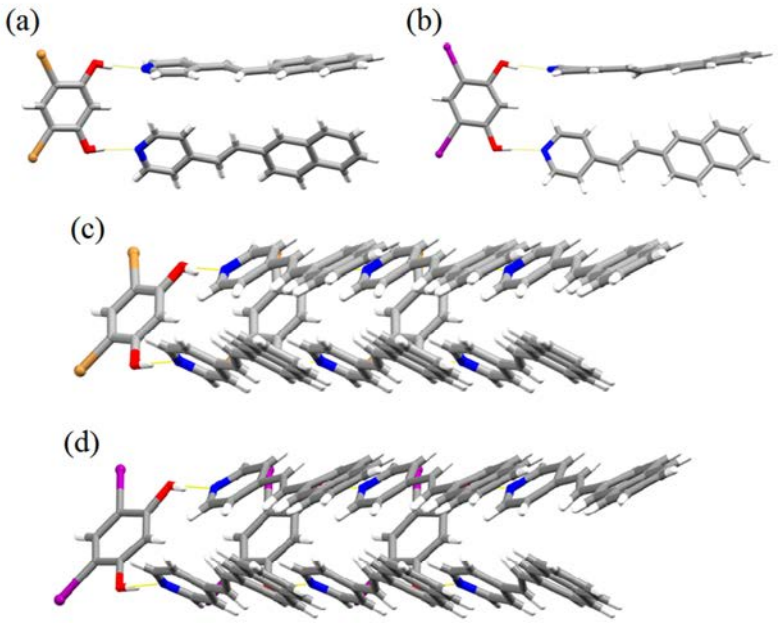

Figure 48: Assembly of a) 2(NPE)·(4,6-diBr-res) and b) 2(NPE)·(4,6-diI-res). Crystal packing of c) 2(NPE)·(4,6-diBr-res) and d) 2(NPE)·(4,6-diI-res) as viewed down *a*-axis.

2.9.3.1.2 Co-crystal of 2(NPE)·(4,6-diCl-res)

Co-crystallization of NPE with 4,6-diCl-res afforded colorless blades with a 2:1 ratio of NPE to 4,6-diCl-res in the monoclinic space group $P2_1$. The asymmetric unit contains one acetonitrile molecule, two NPE molecules and one 4,6-diCl-res molecule. Discrete assemblies are formed between the 4,6-diCl-res and the two NPE molecules through O-H···N hydrogen bonds [O···N separation (Å): (O_1···N_1) 2.696(5), (O_2···N_2) 2.731(5)]. Within the discrete assemblies, the NPE molecules are directed by C-H···π interactions into an edge-to-face orientation with an angle of 56°. The assemblies pack in such a way as to propagate the edge-to-face packing throughout the crystal (Figure 49).

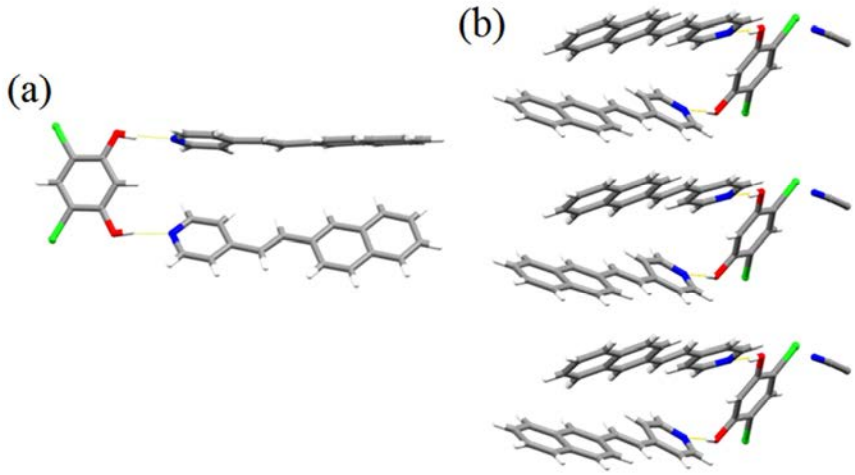

Figure 49: Crystal structure of 2(NPE)·(4,6-diCl-res) a) assembly and b) packing viewed down *a*-axis.

2.9.4 Co-crystallization with carboxylic acids

Two co-crystals were obtained using carboxylic acids as SCCFs. Specifically, co-crystals were obtained with β-PTE when benzoic acid and succinic acid, were used as SCCF. Discrete hydrogen-bonded assemblies were exhibited in both (β-PTE)·(benzoic acid) and (β-PTE)·(succinic acid) co-crystals. The interatomic distances and angles for the co-crystals are tabulated in Table 6.

Table 6: Interatomic distances and angles for co-crystals involving carboxylic acid SCCFs

SCCF	O···N bond distance (Å)	Closest C=C distances (Å)	Pyridine-Thiophene twist angle (°)
Benzoic acid	2.682(6)	7.4	35.0
Succinic acid	2.644(3), 2.682(2)	4.0	2.0, 3.2

2.9.4.1 Co-crystal of (β-PTE)·(benzoic acid)

Co-crystallization of β-PTE with benzoic acid afforded colorless prisms with a 1:1 ratio of β-PTE to benzoic acid in the monoclinic space group $P2_1/n$. The asymmetric unit contains one β-PTE and one benzoic acid molecule. A 0-D assembly is formed between benzoic acid and β-PTE through O-H···N hydrogen bonds [O···N separation (Å): 2.682(6)] (Figure 50a). The β-PTE molecule in the assembly exhibits a twist angle of 35° between the pyridine and the thiophene breaking up the conjugated unit. The assemblies pack with C-H··π interactions between the H-atoms on the benzoic acid and the π-cloud of the thiophene causing a slight herringbone motif (Figure 50b). The closest olefin distance is 7.4 Å, outside the distance stated in the topochemical postulate, so photoreaction is not observed.

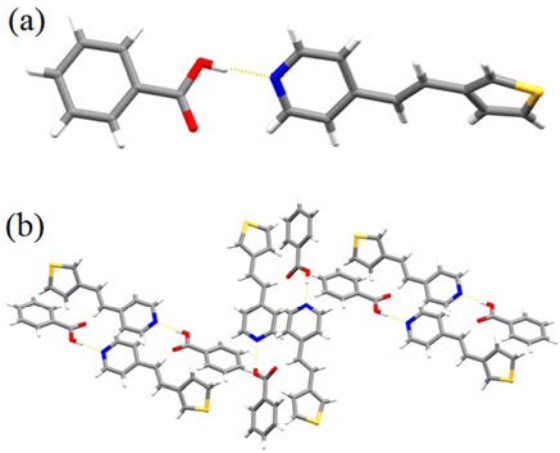

Figure 50: Crystal structure of (β-PTE)·(benzoic acid) a) assembly and b) solid-state packing viewed down *a*-axis.

2.9.4.2 Co-crystal of 2(β-PTE)·(succinic acid)

Co-crystallization of β-PTE with succinic acid afforded colorless plates with a 2:1 ratio of β-PTE to succinic acid in the monoclinic space group $P2_1/c$. The asymmetric unit contains one succinic acid and two β-PTE molecules. The β-PTE molecules are relatively flat with a twist angle between the thiophene and pyridine of 3.2° and 2.0° for the two molecules. A 0-D rod like assembly is formed between the succinic acid and two β-PTE molecules through O-H···N hydrogen bonds [O···N separation (Å): (O_1···N_1) 2.644(3), (O_2···N_2) 2.682(2)] (Figure 51a). The assemblies pack in a brick like fashion (Figure 51b and c). The arrangement in the solid state places the olefins of two β-PTE molecules parallel and at a distance of 4.0 Å, which is suitable for photoreaction. There is no long range π-stacking in the solid due to the succinic acid molecules separating β-PTE dimers.

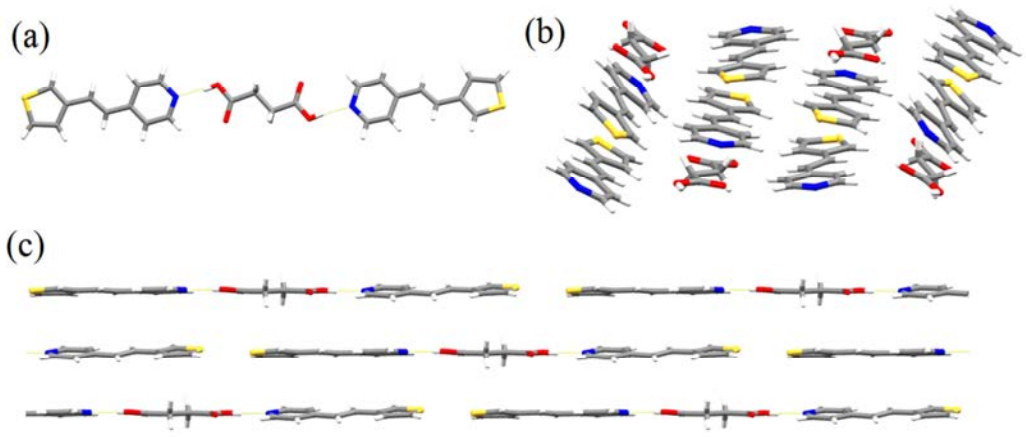

Figure 51: Crystal structure of 2(β-PTE)·(succinic acid) a) 0-D assembly, b) packing viewed down *b*-axis, and c) packing viewed down *a*-axis.

2.9.5 Photoreactivity Studies

2.9.5.1 Photoreactivity studies 2(α-PTE)·(4,6-diI-res)

There are two different assemblies within the 2(α-PTE)·(4,6-diI-res) co-crystal. The olefins within assemblies are both separated by 4.2 Å and aligned, and thus conform to the topochemical postulate. Hence, a [2+2] photoreaction is expected to occur when the co-crystal is exposed to ultraviolet light. Upon being exposed to UV light, a [2+2] photoreaction occurred as shown by ^{1}H NMR data (Figure 52). The photoreaction was characterized by the upfield shift of the H-atoms of the pyridyl and thienyl moieties consistent with the loss of conjugation in the photoproduct, as well as the appearance of peaks at 4.48 and 4.75 ppm indicating cyclobutane formation. The photoreaction reached 95% yield upon irradiation for 100 hrs based on the ratio of the area of the α-pyridyl H-atoms before and after reaction. The photoproduct was isolated by recrystallization of a

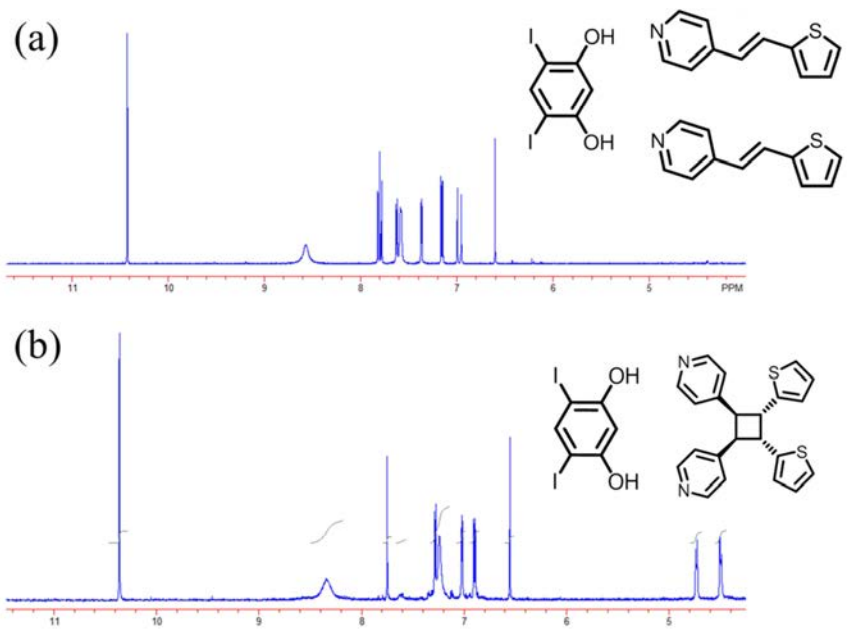

Figure 52: ^{1}H NMR spectrum of 2(α-PTE)·(4,6-diI-res) a) before and b) after 100 hrs of UV exposure.

reacted solid from a 1:1:1 toluene to acetonitrile to methanol solution and the stereochemistry of the product was determined *via* X-ray diffraction. The photoproduct obtained is the head-to-head product *rctt*-1,2-bis(4-pyridyl)-3,4-bis(2-thienyl)cyclobutane (d2Tcb) present in the form of (d2tcb)·(4,6-diI-res) (Figure 53).

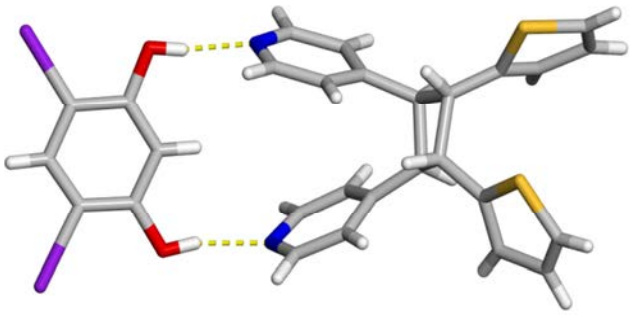

Figure 53: Crystal structure of (d2tcb)·(4,6-diI-res).

The co-crystal obtained consists of 0-D assemblies comprised of O-H···N hydrogen bonds [O···N separation (Å): O(1)···N(1), 2.666; O(2)···N(2), 2.704]. From the crystal structure it was determined that the thiophenes are located *cis*-along the cyclobutane ring. The splaying angle of the thiophenes is 75^{o} with their mean planes at an angle of 58^{o}, compared to 27^{o} before reaction.

2.9.5.2 Photoreactive studies (α-PTE)·(5-acetyl-res)

The 1-D assembly formed in the co-crystal of (α-PTE)·(5-acetyl-res) has the olefins at a distance of 8.2 Å within the assembly and at a distance of 5.3 Å between 1-D assemblies. Upon UV exposure, photodimerization is observed by the upfield shifts in the ^{1}H NMR spectrum and the appearance of peaks in the region of 4-5 ppm (Figure 54). From the ^{1}H NMR data there is a 77% yield of the photoproduct. The distance of the C=C bonds suggest a non-topochemical mechanism for the [2+2] reaction. There are several known photoreactions that occur that do not conform the topochemical postulate

(i.e. crossed double bonds and distances greater than 4.2 Å).[128-131] A suggested mechanism for a non-topochemical reaction is the molecular migration of molecules guided by the crystal lattice.[101] Molecules can migrate along glide planes within the crystal as long as the glide plane does not interlock with another layer.[131] The 1-D polymers in the co-crystals are not interlock which can allow for the movement necessary for photoreaction to occur. The stereochemistry of a photoproduct that occurs by a non-topochemical [2+2] photoreactions is difficult to predict.[130]

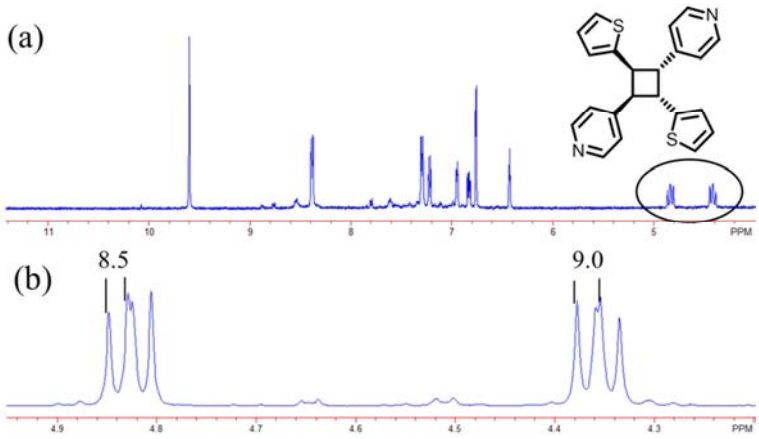

Figure 54: ^{1}H NMR spectrum of (α-PTE)·(5-acetyl-res) a) after 120 hours of UV exposure and b) peaks of cyclobutane H-atoms of photoproduct.

There are eleven total possible photoproducts resulting from the photodimerization of α-PTE, six head-to-head and five head-to-tail photoproducts (Figure 55). The cyclobutane peaks for the photoreaction in the solid 2(αPTE)·(5-acetyl-res) are different than the one obtained in the photoreaction of 2(α-PTE)·(4,6-diI-res), eliminating the head-to-head *rctt* as a possible product. The cyclobutane peaks for photoproduct appear as two peaks, both with a doublet of doublets splitting pattern with J couplings of 8 and 9.5 Hz. Since there are only two peaks for the cyclobutane H-atoms, the photoproduct must possess some degree of symmetry, thus eliminating the following

dimers; head-to-head dimers *rcct*, and *rtcc*, as well as the head-to-tail dimers *rtcc* and *rttt*. Since the splitting pattern of both peaks is doublet of doublets, each H-atom is next to two inequivalent H-atoms. Since there are only two types of H-atoms on the cyclobutane ring, the H-atoms that are equivalent are on opposite corners of the ring which is a criteria only the head-to-tail dimers meet. That leaves only the head-to-tail dimers with *rccc*, *rctt*, and *rtct* stereochemistry as the only possible products. The two different coupling values from two equivalent H-atoms suggest a *trans*-stereochemistry between the two equivalent H-atoms eliminating *rccc and rtct* as possible products. Only the head-to-tail *rctt* stereochemistry meets the criteria making *rctt*-1,3-bis(4-pyridyl)-2,4-bis(2-thienyl)cyclobutane the most probable photoproduct. The coupling values and splitting pattern of the ^{1}H NMR data is similar to reported head-to-tail cyclobutane dimers with *rctt* stereochemistry further suggesting the head-to-tail *rctt* dimer as the photoproduct.[132-134]

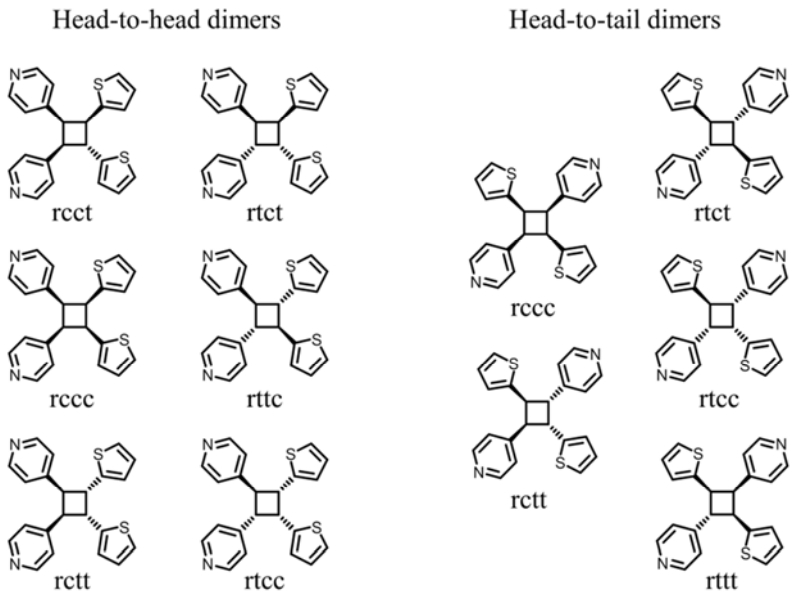

Figure 55: Possible photoproducts of [2+2] photodimerization of α-PTE.

2.9.5.3 Photoreactive studies 2(β-PTE)·(4,6-diI-res)

There are two assemblies in the co-crystal of 2(β-PTE)·(4,6-diI-res). The C=C bonds in both of the assemblies are separated by 4.1 and 4.2 Å and are parallel. Thus, both fit the topochemical postulate and are expected to undergo a [2+2] photodimerization. ^{1}H NMR data confirmed a [2+2] photoreaction upon exposure to UV light by the upfield shift of peaks and appearance of a peak in the region of 4-5 ppm signifying cyclobutane formation (Figure 56a and b). The photoreaction reached 94% yield upon irradiation for 160 hrs. The photoproduct was isolated by recrystallization of

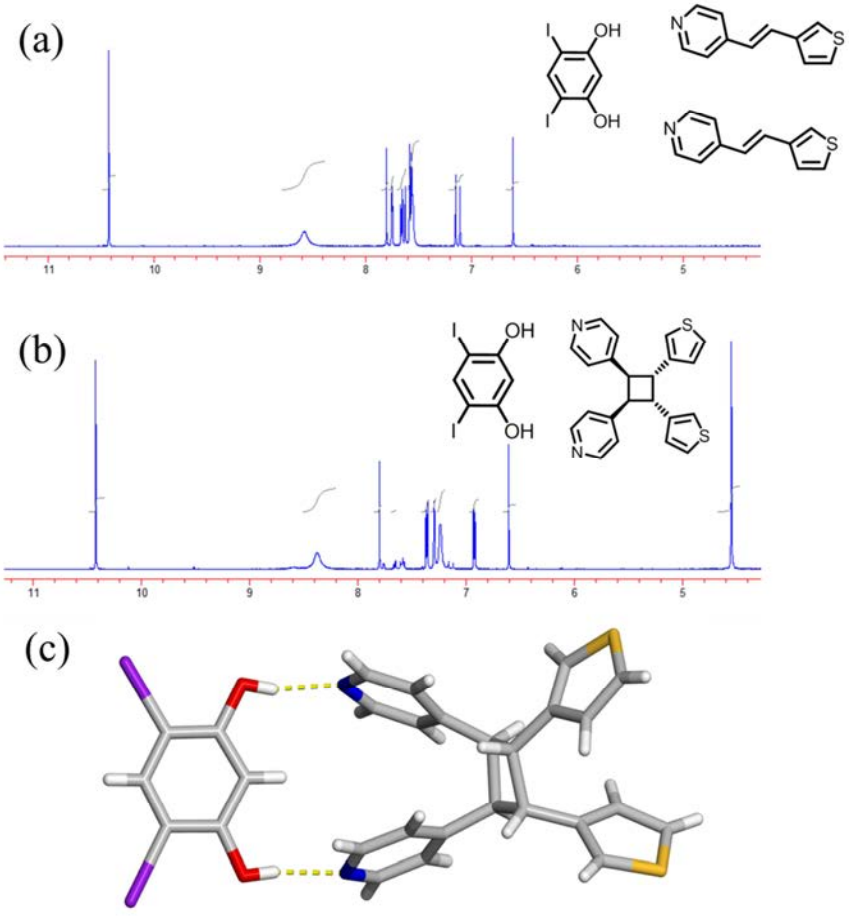

Figure 56: ^{1}H NMR spectrum of 2(β-PTE)·(4,6-diI-res) co-crystal a) before and b) after 160 hour UV exposure, and C) Crystal structure of 2(d3tcb)·4,6-diI-res.

a reacted solid from a 1:1:1 toluene to acetonitrile to methanol solution and the stereochemistry of the product was determined *via* x-ray diffraction. The obtained head-to-head photoproduct is *rctt*-1,2-bis(4-pyridyl)-3,4-bis(3-thienyl)cyclobutane (d3tcb) present in the form of (d3tcb)·(4,6-diI-res) (Figure 56c).

The co-crystal obtained consists of 0-D assemblies comprised of O-H···N hydrogen bonds [O···N separation (Å): O(1)···N(1), 2.707; O(2)···N(2), 2.683]. From the crystal structure it was determined that the thiophenes are located *cis*-along the cyclobutane ring. The splaying angle of the thiophenes in d3tcb is 72^{o} and the mean planes of the thiophenes are at an angle of 56^{o}, and increase compared to before reaction, similar to what was seen for in the photoproduct d2tcb.

2.9.5.4 Photoreactive studies of 2(β-PTE)·(succinic acid)

Within the crystal structure of 2(β-PTE)·(succinic acid) two molecules of β-PTE are aligned in a head-to-tail fashion with the olefins at a distance of 4.0 Å. When exposed to UV light, the photodimerization is observed through the upfield shift of peaks and the appearance of peaks in the region 4-5 ppm indicating cyclobutane formation. The reaction reached 86% yield of the photoproduct after 100 hours of UV exposure (Figure 57a). Due to the distance of the double bonds, the reaction is expected to be topochemically controlled and give the photoproduct *rctt*-1,3-bis(4-pyridyl)-2,4-bis(3-thienyl)cyclobutane. The cyclobutane peaks have a similar splitting pattern as the photoproduct obtained from reacting the solid of (α-PTE)·(5-acetyl-res) which was determine to have *rctt* stereochemistry around the cyclobutane (Figure 57b), suggesting *rctt*-1,3-bis(4-pyridyl)-2,4-bis(3-thienyl)cyclobutane is the photoproduct.

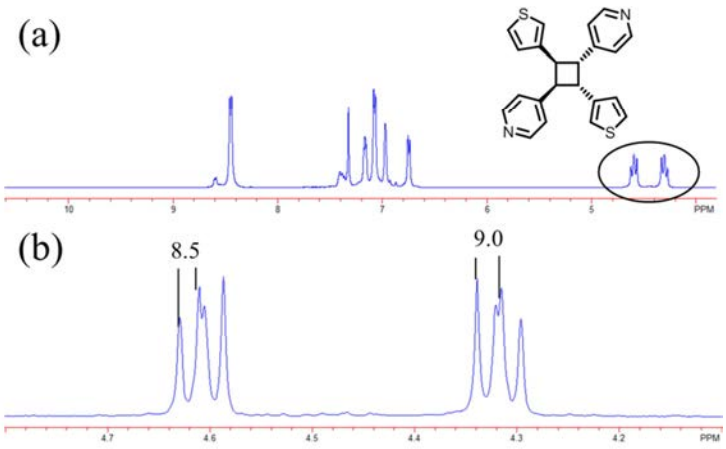

Figure 57: A) ^{1}H NMR spectrum of 2(β-PET)·(succinic acid) after 100 hours UV exposure, B) Zoom in on cyclobutane H-atoms from photoproduct.

2.9.6 Computational studies

2.9.6.1 Photodimerization

To study the effects that photodimerized has on an organic semiconductor building block, the electronic properties of α-PTE, d2tcb, β-PTE, and d3tcb were determined using DFT calculations (b3lyp 6-31G*). Before photoreaction the calculated HOMO energy level was -5.76 eV and the LUMO energy level was -1.88 eV for α-PTE. The HOMO and LUMO energy levels for β-PTE were determined to be -5.89 eV and -1.66 eV, respectively. These values give a band gap of 3.88 eV for α-PTE and 4.23 eV for β-PTE. Photodimerization of α-PTE or β-PTE caused an increase in the gap between the HOMO and LUMO energy levels. The head-to-head photodimerized product of α-PTE, obtained from UV irradiation of the 2(α-PTE)·(4,6-diI-res) co-crystals, has HOMO and LUMO energy levels of -6.19 eV and -0.95 eV, respectively. This gives the head-to-head photodimerized product of α-PTE band gap of 5.24 eV. The head-to-head photodimerized product of β-PTE has a band gap of 5.4 eV with a HOMO energy of -6.31 eV and a LUMO energy of -0.91 eV. The lower HOMO energy levels are expected

to lower the charge mobility of the photoproducts when compared to the unreacted molecules. The band gap of the starting components was verified with UV/Vis spectroscopy (Figure 58). The band gap of α-PTE was found to be 3.78 eV and β-PTE was found to be 4.03 eV. Both values are a slightly lower than the calculated band gaps suggesting that the calculations are close to the actuals.

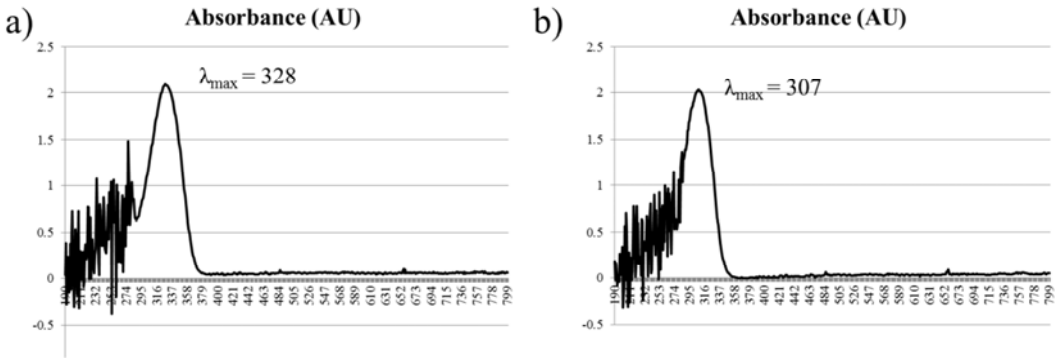

Figure 58: UV/Vis spectra for a) α-PTE and b) β-PTE

2.9.6.2 Edge-to-face orientation

The formation of the edge-to-face assembly was further studied using computational chemistry. Energy calculations were performed in the gas phase for each β-PTE dimer within an assembly for the solids 2(β-PTE)·(4,6-diI-res) and 2(β-PTE)·(4,6-diCl-res) using their crystallographic orientations. The binding energies for each dimer was determined by subtracting the energy of each β-PTE individual molecule from the total energy of the dimer. It was found that the binding energy for β-PTE of the edge-to-face orientation is 1.26 kcal/mol higher in energy then in a face-to-face orientation. Since the binding energy is the total energy gained from the interaction between the two

molecules and edge-to-face has a lower bonding energy it has less orbital-orbital interactions than the face-to-face dimer.

Given that thiophenes have shown a preference for edge-to-face packing the binding energy was calculated for each component of β-PTE (i.e. the pyridine and thiophene) based off of their crystallographic orientations. The binding energies for the thiophenes was found to be -3.02 and -2.42 kcal/mol in the face-to-face dimers and -2.90 kcal/mol in the edge-to-face dimer. The binding energies suggest thiophene has no preference for either geometry. However, the binding energies for the pyridine showed a preference for the face-to-face orientation with binding energies of -2.12 and -2.43 kcal/mol for the face-to-face orientation and -2.04 kcal/mol for the edge-to-face orientation. The observation suggests that the pyridine helps to promote the face-to-face stacking.

2.9.7 Formation of Thin Films

Thin films were created using 4,4′-BPE as the reactive component along with a template known to direct 4,4′-BPE into a photoreactive arrangement. Attempts to make thin films of 4,4′-BPE alone did not yield uniform thin films. Instead, visual inspection revealed a rough surface with crystalline domains was obtained. Since, 4,4′-BPE did not yield a uniform film, the template must aid in thin film formation along with directing 4,4′-BPE into a photoreactive arrangement. The first template that was used to attempt to make a thin film was 1,3-dihydroxyresorcinol. Attempts to form a thin film failed instead yielding isolated single crystals (Figure 59a). Since alkyl chains are known to organize through lipophilic forces,[65] HP was employed. From a previous result, we know from the crystal structure of 2(4,4′-BPE)·2(HP) that alkyl chains organize the 0-D assemblies into 1-D columns through interdigitation of the alkyl chains and that the photoreaction proceeds to an 81 % yield.[112] It was discovered that a 1:1 molar solution of 4,4’-BPE and

HP at 9 mg/ml dissolved in a 1:1 isopropanol and 1,3-dichlorobenzene solution yield the most uniform thin film (Figure 59b).

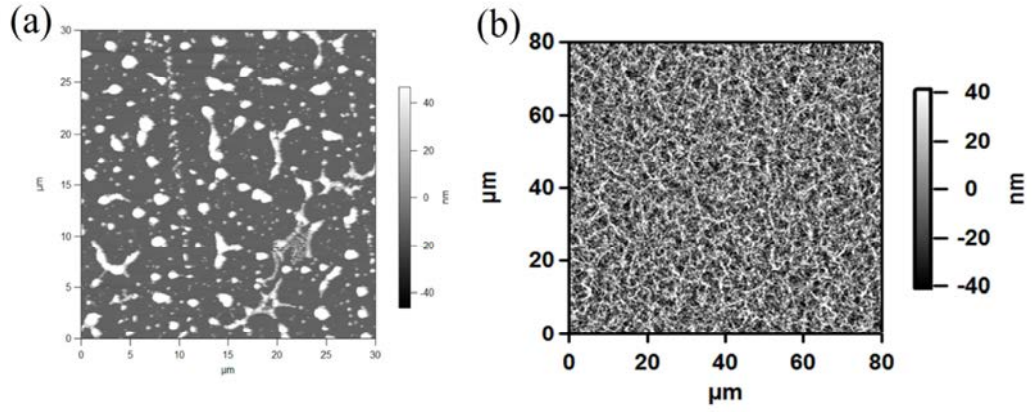

Figure 59: AFM images of spin coated slide of a) 2(BPE)·2(Res) and b) 2(BPE)·2(HP).

2.9.8 Development and Characterization of Thin Films

AFM was used to characterize the thin films along with mass spectrometry and NMR spectroscopy. The thickness of the thin films as measured by AFM varied between 70 -80 nm with a roughness of 20 nm. To ensure that the photoreactive assembly is being formed, the MS was taken on 5 combined thin films of initial thin films formed and on 5 combined thin films after 20 hrs of UV irradiation (Figure 60a and b). In the MS of the initial thin film, the peak at 183 m/z is equivalent to monoprotonated 4,4′-BPE and the peak at 239 m/z is equivalent to monoprotonated HP. After exposure to UV light a peak at 365 m/z appeared. The peak at 365 m/z corresponds to the monoprotonated photodimer of 4,4′-BPE. The peak at 239 m/z once again corresponds to the monoprotonated HP. The peak at 183 m/z after UV exposure can represent either unreacted monoprotonated 4,4′-BPE or the diprotonated photodimer. To determine the percentage of the photoreaction, ^{1}H NMR was taken on the materials from a combined 80

thin films that were exposed to UV light for 20 hrs (Figure 60c). Based on the α-pyridine H-atoms the photoreaction occurred to approximately 50% yield.

Since the ability to perform [2+2] photodimerization has been established by MS and ^{1}H NMR data, the ability to photopattern the thin film was investigated. First a suitable solvent was found that could selectively dissolve either the unreacted or reacted thin film. It was found that submerging the unexposed thin film in a 2:1 pentane: ethyl ether solution for 15s resulted in no measurable amount of thin film left on the glass

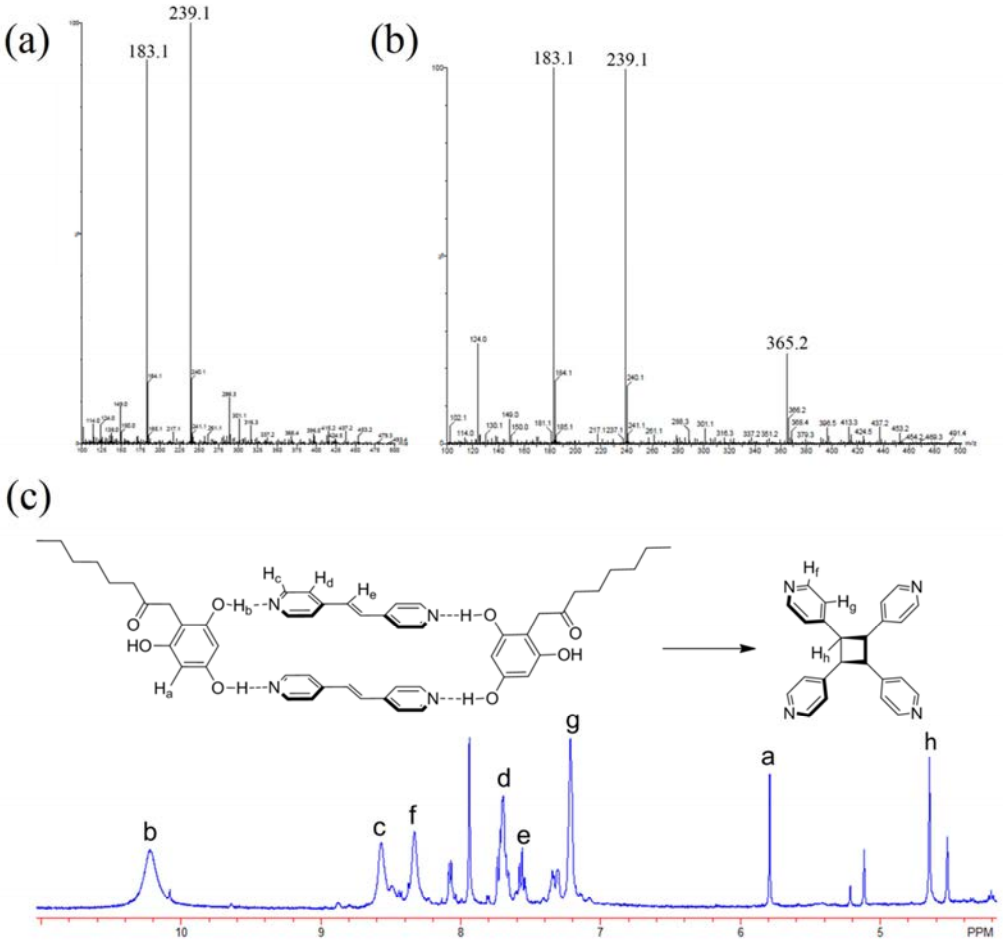

Figure 60: Mass spectra of thin film a) before reaction and b) after 20 hours UV exposure, and c) ^{1}H NMR spectrum of 80 thin films after 20 hours UV exposure.

slide. Submerging of a thin film exposed to UV light for 20 hours by the same method results in only a 10 nm change in the thickness of the thin film. To create a photopatterned film, a thin film was placed in a black box constructed from black construction paper with a 10 μm photomask placed on top of the thin film and a piece of borosilicate glass was used to cut off wavelengths below 300 nm. It was found that UV exposure for two hours gave the best results. After two hours of exposure a color change could be seen in thin film through the AFM camera, but no noticeable change in the thin film surface was detected by AFM. The patterned thin film was then submerged in the 2:1 pentane: ethyl ether solution for 15s intervals and the changes in the thin film were monitored after each washing by AFM (Figure 61). After each development the difference in height between the exposed and unexposed region increased. The regions exposed to ultraviolet light decrease in height by roughly 10 nm per 15 second washing

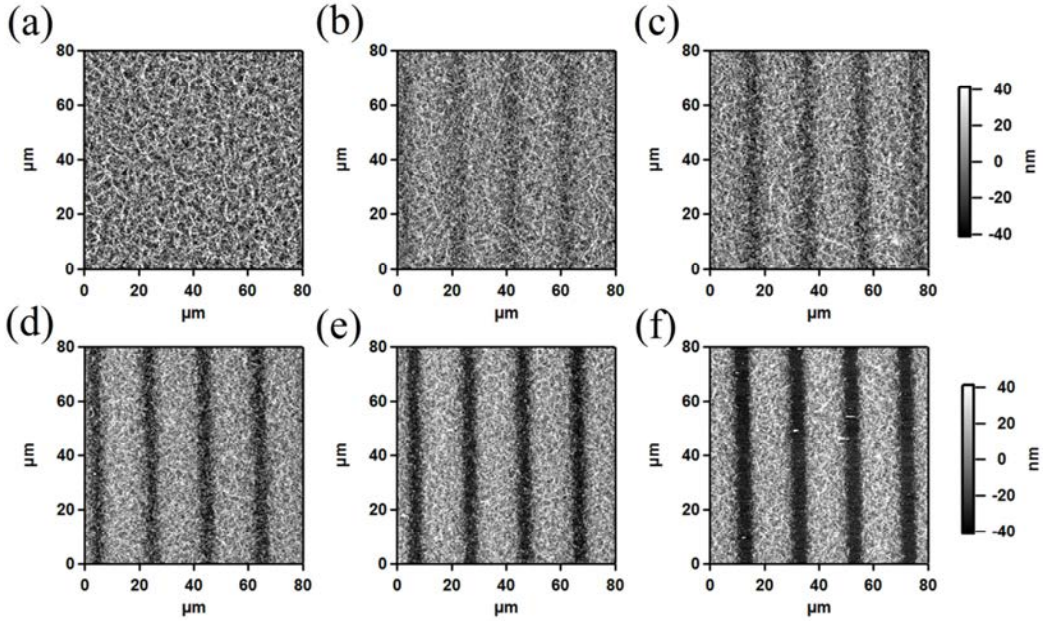

Figure 61: AFM images of a) initial film after exposure, and after b) 15s washing, c) 30s washing, d) 45s washing, e) 60s washing, and f) 75s washing.

while the unexposed regions decreased by approximately 20 nm per 15 second washing. After four washings, the unexposed regions had been mostly washed away such that glass could be detected between the exposed regions which still had a height of 40 nm (Figure 62a). A fifth washing left only the exposed regions on the glass slide. Since the patterned filmed was only exposed for two hours while the initial film was exposed for 20 hours the solubility of each film in the development solution was compared. The solubility of the exposed with photomask and exposed without a photomask is similar (Figure 62b). This suggests that the chemical makeup of the thin film at a two hour exposure time is similar to the chemical makeup of the thin film when exposed for 20 hours. Exposure through a different photomask allowed for features as small as 5 μm to be obtained.

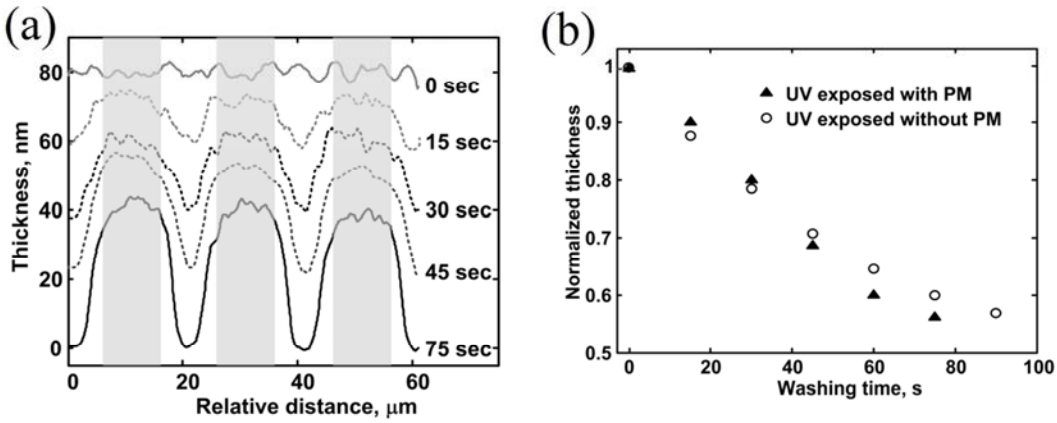

Figure 62: Graph of film thickness versus washing a) profile and b) with and without photomask.

2.10 Conclusion

We demonstrated the ability to align thiophenes for photoreaction through the use of our co-crystallization method. The modularity of our approach allowed us to switch

co-crystal formers until an appropriate one was found for near quantitative photoreaction of thiophenes. Computational studies show that the band gap between the HOMO and LUMO increases after photodimerization. The change in band gap suggests that photoreaction of thiophene compounds could function as a way to alter the mobility after processing. An added benefit of this approach is the stacking of the thiophene compounds in the co-crystal which should cause an increase in the mobility of the crystal before photoreaction. However, co-crystallization of a single resorcinol derivative with NPE did not overcome the edge-to-face packing of the naphthalene moiety. When irradiated with UV light no photoreaction was observed. Two possible methods to overcome the edge-to-face packing is the addition of a second handle to the naphthalene moiety or the introduction of a secondary intermolecular force to help stabilize the desired orientation.

We also demonstrated the ability to transfer the templating method to two-component thin films. We were able to obtain the photoreactive assembly in a thin film by using HP as a template with 4,4′-BPE. The obtained thin film could be photo patterned and the unreacted region could be washed away. The ability to selectively wash away areas of the thin film allows for possible applications of the process as a photoresist or photopattern organic semiconductors.

CHAPTER 3: ELECTRONIC PROPERTIES OF SEMICONDUCTOR CO-CRYSTALS

3.1 Introduction

The utility of organic semiconductors for applications is determined by the mobility of the material. Charge transport in organic semiconductors occurs via a hopping mechanism between conjugated π-systems of neighboring molecules. The hopping mechanism makes not only the HOMO/LUMO energy levels of the molecule but also the orientation of neighboring molecules important. Thus, to improve the mobility of organic semiconductors either the size of the conjugated π-system can be increased or the π-π overlap between adjacent molecules must be improved. A mobility of 1 $cm^2V^{-1}s^{-1}$ would match amorphous silicon, which is used in liquid crystal displays, and is considered the benchmark for organic semiconductors.[35] The benchmark has been reached by a few unsubstituted organic semiconductors, some of which are summarized in Table 7.[135]

Table 7: Selected mobilities of unsubstituted organic semiconductors

Organic Semiconductor	Mobility ($cm^2V^{-1}s^{-1}$)	Ref
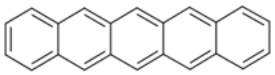	35	35
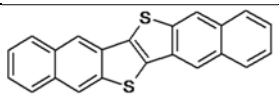	2.9	135
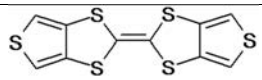	1.4	135
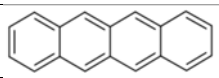	1.3	74
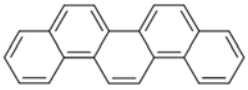	1.1	135
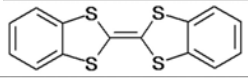	1.0	135
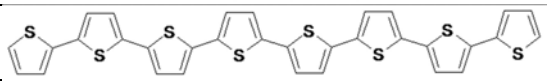	0.33	50

However, the low solubility of the large conjugated system limits the methods which can be used to form devices. This has led to research to improve the packing of smaller more soluble systems and the solubility of the larger systems through functionalization.

3.2 Overview

This chapter will cover an approach to impact the mobility of organic semiconductors through co-crystallization. The aim of the approach is to improve the π-π overlap of organic semiconductors through the addition of a semiconductor co-crystal former (SCCF). If the second component can improve π-π overlap of the organic semiconducting molecules then we expect an improvement in the mobility. The SCCF is expected to align the organic semiconductor molecules into π-stacked assemblies through hydrogen-bonds (Figure 63). Improving the mobility through increasing the amount of π-stacking has already been shown in other systems.[51,54,65] The impact of a second component on the charge transport properties of a system is studied herein.

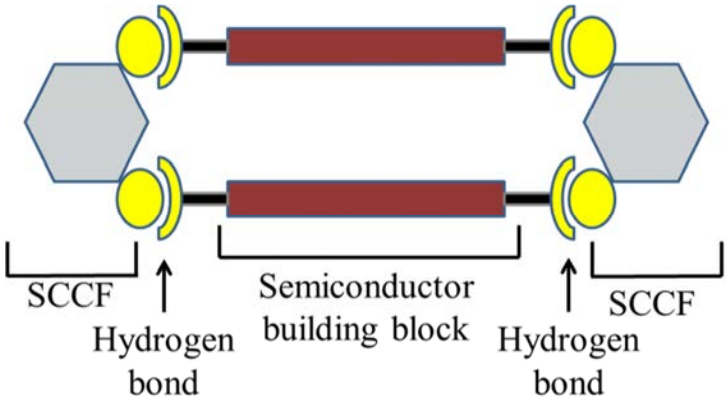

Figure 63: Scheme for hydrogen bonded assembly of 2(SBB)·2(SCCF).

3.3 Mobilities in oligothiophenes

A large number of oligothiophenes have been studied as organic semiconductors owing to ease of synthesis. The highest recorded mobility for an unsubstituted linear oligothiophene is 0.33 $cm^2V^{-1}s^{-1}$ for octithiophene.[32] To improve mobility of oligothiophenes, either the size of the conjugated system or the amount of π-overlap between neighboring molecules needs to be increased. The improvement of π-overlap between neighboring molecules through synthetic modification has been the main approach. However, it is difficult to predict how additional groups will affect overall crystal packing. Many derivatives have been made of oligothiophenes and have achieved a variety of results. The mobilities of a few oligothiophenes and oligothiophene derivatives are listed in Table 8.[65]

3.3.1 Approaches towards improving mobilities in oligothiophenes

A promising approach towards the improvement of mobility in oligothiophenes is the addition of alkyl groups to the ends of oligothiophenes chains. The addition of alkyl chains can lead to improved mobility. The improved mobility occurs because of interdigitation of alkyl chains, which increases long range order in thin films (Figure 64). However, it has been shown that the length of the alkyl chain has an impact on the mobility. The addition of an ethyl chain to sexithiophene leads to a mobility of 1.1 $cm^2V^{-1}s^{-1}$. Increasing the alky chain length by four C-atoms, to n-hexyl, drops the mobility to 1.0 $cm^2V^{-1}s^{-1}$. Further increasing the alkyl chain by another four C-atoms, to n-decyl, results in a further drop of mobility to 0.1 $cm^2V^1s^{-1}$.[65] The longer alkyl chains are needed for improved mobility in different thiophene based semiconductors. The addition of an n-octyl chain to biphenylbithiophene affords a mobility of 0.18 $cm^2V^{-1}s^{-1}$. However, the addition of a n- octyl chain to biphenylterthiophene results in a mobility of 0.019 $cm^2V^{-1}s^{-1}$.[68] The decrease in mobility would not be expected with an increase in conjugation

Table 8: Selective mobilities of organic semiconductors containing thiophenes

Organic Semiconductor	Mobility ($cm^2V^{-1}s^{-1}$)	Ref
Unsubstituted oligothiophenes		
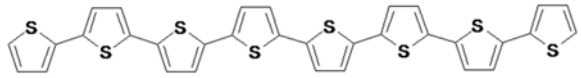	0.33	50
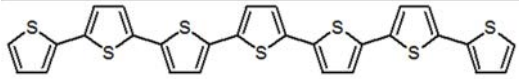	0.13	32
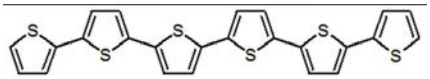	0.08	50
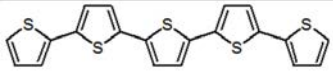	0.05	32
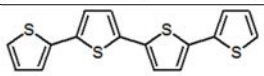	0.006	50
Alpha-alkyl chain oligothiophene		
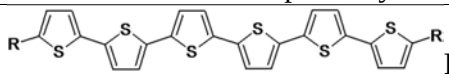 R= ethyl	1.1	65
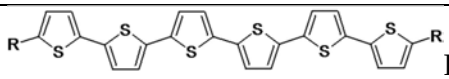 R= n-hexyl	1.0	65
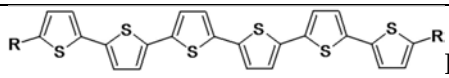 R= n-decyl	0.1	65
Hybrid system		
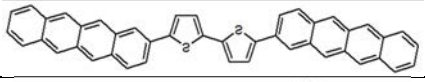	0.32	141
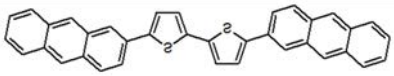	0.11	141
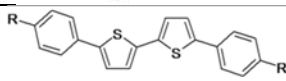 R= n-octyl	0.18	68
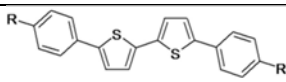 R= n-butyl	0.14	68
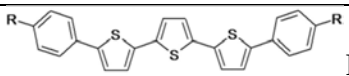 R = n-butyl	0.14	68
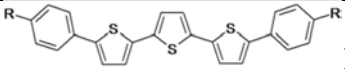 R= n-octyl	0.019	68
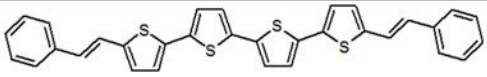	0.1	149
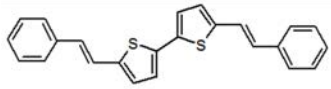	0.02	149
Hydrogen bonds in oligothiophenes		
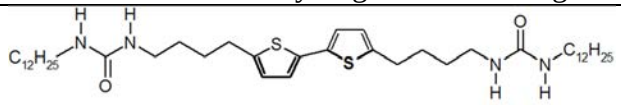	0.005	82

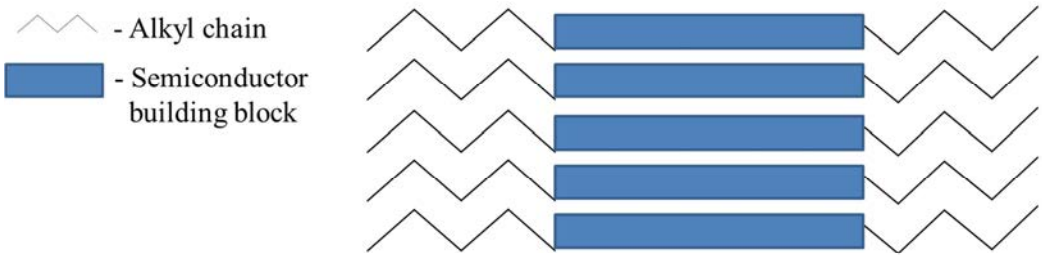

Figure 64: Scheme for interdigitation of alkyl chains.

length. The inability to predict the affects a given substituent will have on the mobility creates the need to synthesis compounds until the desired property is found.

Another approach towards improving packing is the incorporation of groups that provide strong intermolecular forces, such as hydrogen bonds. Hydrogen bonds provide an intermolecular force stronger than the C-H···π interactions, and thus, should have a greater effect dictating solid-state packing. Hydrogen bonds are introduced in such a way that molecules propagate either horizontally or vertically to prevent herringbone packing (Figure 65). Feringa *et.al.* successfully used hydrogen bonds to stack bithiophene molecules through the incorporation of urea groups. Bithiophene molecules were directed into 1-D columns through N-H···O hydrogen bonds and a mobility of 0.005

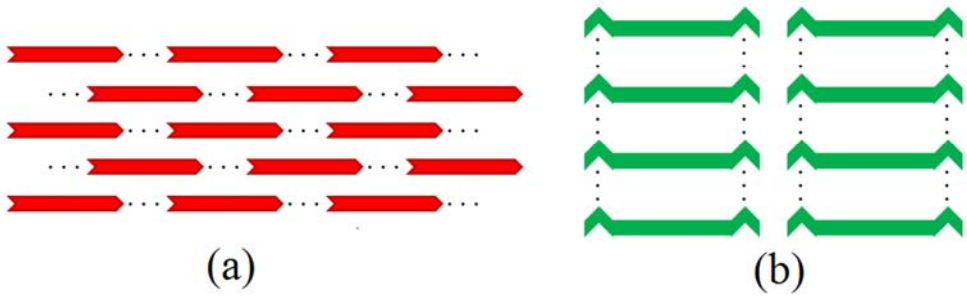

Figure 65: Directional hydrogen bonding in a) horizontal direction and b) vertical direction.

$cm^2V^{-1}s^{-1}$ was obtained, similar to quaterthiophene when measured by the same method.[82] Hydrogen bonds have also been implemented to form horizontal 1-D rows of a pyrene based structure.[136]

3.4 Effect of electronic properties on mobility and stability of organic semiconductors

Similar to inorganic semiconductors, the ability for an organic semiconductor to facilitate movement of charge is related to the energy level of HOMO and LUMO. For p-type semiconductors a HOMO energy level is typically between -4.9 and -5.5 eV. Pentacene, one of the most studied and best performing semiconductors, has a HOMO energy level of -5.14 eV.[53] A lower HOMO energy level through modification of the organic semiconductor has been shown to display higher mobilities. The lowering of the HOMO energy level can cause an increase in the HOMO-LUMO band gap, which also plays a role in the stability of the organic semiconductors. A major obstacle with organic semiconductors with low HOMO-LUMO band gaps is low stability to oxygen and water. Materials with higher HOMO-LUMO band gaps have been shown to have a greater stability and maintain their charge mobility over extended periods of time.[53]

3.5 Effect of orbital overlap in organic semiconductors

The mobility of electrons in organic semiconductors occurs through a hopping mechanism wherein electrons hop between neighboring molecules (Figure 66a). The rate of hopping can be described using Marcus theory in which k is the rate of hopping (Figure 66b).[31] Marcus theory states the rate of hopping is dependent on the temperature (T), the reorganizational energy (λ) and the effective electronic coupling matrix (V). The reorganizational energy is the energy required to modify the geometry when an electron is added or removed. Larger π-systems tend to have smaller HOMO/LUMO gaps that allow for a decrease in the reorganizational energy, however, such molecules can be prone to oxidation.[137] This has led to research to attempt to increase the effective

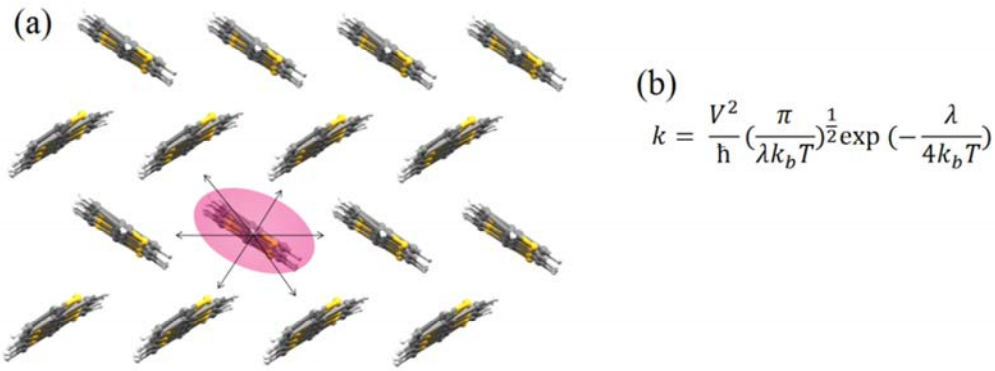

Figure 66: Hopping mechanism for organic semiconductors a) scheme for hopping and b) equation for rate of hopping.

electronic coupling matrix, which is dictated by the orbital overlap between neighboring molecules. Research has shown that the value of the effective electronic coupling matrix is related to the tilt angle between neighboring molecules (Figure 67).[138] The effective electronic coupling matrix is highest when the molecules are in a co-facial position and lowest when in a herringbone packing motif with a 60^{o} angle between molecular planes.

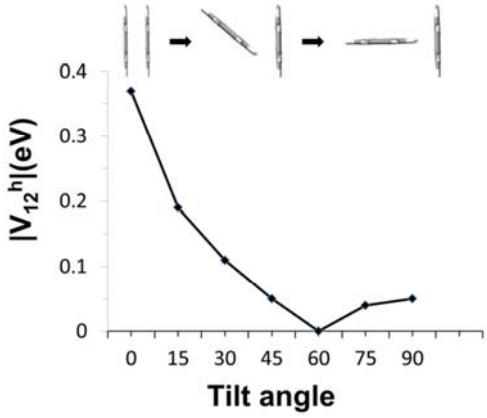

Figure 67: Graph of effective coupling constant versus tilt angle.

3.6 Towards organic semiconductor co-crystals

There have been few examples of crystalline two-component semiconductor materials. In such a system, a second component is introduced to alter packing of the organic semiconductor. For example, nanostructures comprised of semiconductor components have been reported by Fasel *et.al.* through the combination of 3,4,9.10-perylenetetracarboxylic dianhydride and either 4,4″-diamino-*p*-terphenyl or 2,4,6-tris(4-aminophenyl)-1,3,5-triazine. Hydrogen-bonded rectangular superstructures formed between 3,4,9.10-perylenetetracarboxylic dianhydride and 4,4″-diamino-*p*-terphenyl (Figure 68a).[139] A co-crystal comprised of 6,13-dihydropentacene and pentacene has also

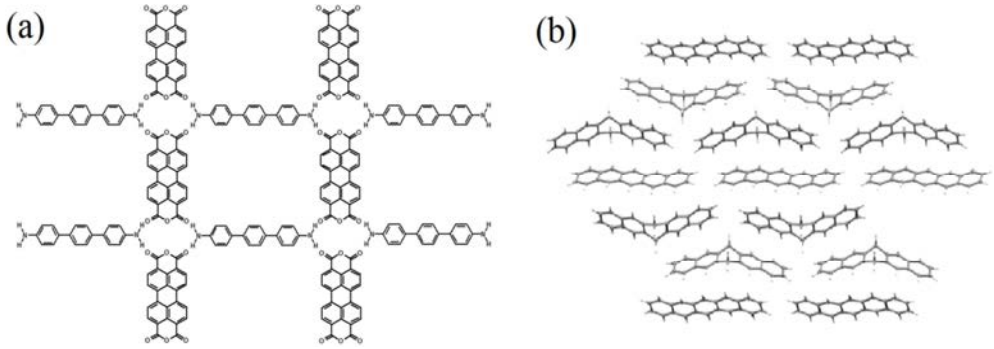

Figure 68: Packing of a) 3,4,6,10-perylenetetracarboxylic dianhydride and 4,4"-diamino-p-terphenyl and b) 2:1 co-crystal of 6,13-dihyrdopentacene to pentacene.

been characterized. A 2:1 co-crystal of 6,13-dihydropentacene to pentacene formed with pentacene layers separated by double layers of 6,13-dihydropentacene (Figure 68b).[140] However, mobility measurements were not reported for the co-crystals. Thus, there currently exits no data on the effect co-crystallization has on the mobility of organic semiconductors.

3.7 Hybrid systems

One of the obstacles that research with organic semiconductors has encountered is low solubility and lack of stability under ambient conditions. To this extent acene-thiophene hybrids have been synthesized to combine the high mobility of acenes with the solubility of substituted oligothiophenes. Recently, these hybrid acene-thiophene systems have not only achieved high mobilities but also demonstrated increased stability under atmospheric conditions (Figure 69).[66,141-143]

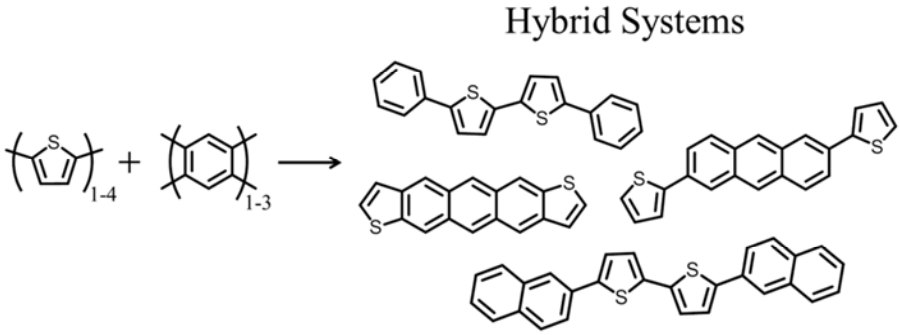

Figure 69: Selected hybrid systems.

In this context the incorporation of ethylene groups has been shown to increase the stability of organic semiconductors. Distyryl capped oligothiophenes have demonstrated no degradation of mobility for over 100 days, compared to octithiophene which showed a 70% decrease over the same period.[144] Organic semiconductors that incorporate ethynyl groups have also demonstrated long term stability to air.[145-148] The incorporation of ethylene and ethynyl groups have been shown to cause a decrease in aromaticity within individual rings.[149] The decrease in aromatic character causes an increase in π-electron delocalization over the entire molecule which helps enforce planarity in flexible systems and cause smaller band gaps.[150]

3.8 Micro- and nano-crystal organic devices

Silicon transistors used in modern electronics have features down to 45 nm. To achieve similar features with organic semiconductors a bottom up approach with crystals of micrometer and nanometer sized crystal dimensions has been suggested by several groups.[151-154] The use of small crystals provides several advantages over thin films. Charge mobility in polycrystalline thin films is often limited by traps and grain boundaries not seen in single crystals.[155] Also, the ability to establish long range order is more difficult in thin films compared to single crystals for mobility measurements. The use of small crystals also avoids a difficulty of having to grow large single crystals. Successful devices made from small crystals have been made using either drop casting or *in situ* growth by surface selective deposition (Figure 70).[156,157] Micro-ribbons of TIPS-

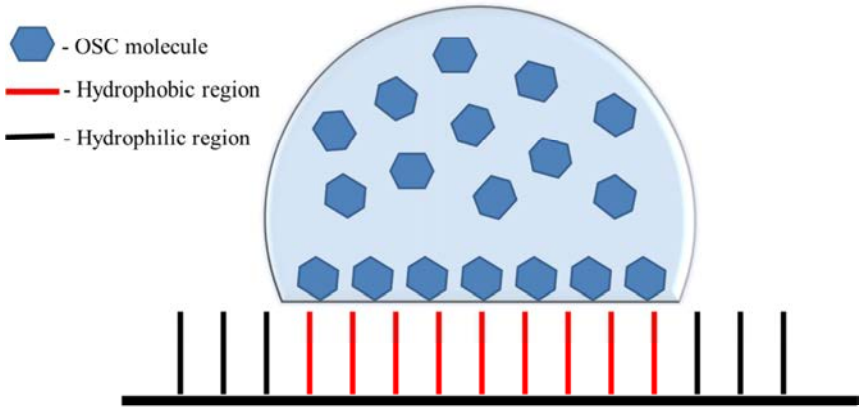

Figure 70: Selective crystal growth on a monolayer patterned glass substrate.

pentacene grown *in situ* exhibited a higher average mobility, 0.75 $cm^2V^{-1}s^{-1}$, then thin films made from TIPS-pentacene, 0.17 $cm^2V^{-1}s^{-1}$.[57,158] The *in situ* growth of TIPS-pentacene crystals has resulted in the highest mobility for a solution grown crystal at 1.42 $cm^2V^{-1}s^{-1}$.[158] The high mobility achieved by *in situ* crystal growth demonstrates the advantage of using small crystals for devices.

3.9 Chapter focus

The focus of this chapter is on how SCCF's affect the mobility of an organic semiconductor. Specifically, the chapter will focus on how different SCCFs affect the packing of *trans*-1,2-bis(2-(4-pyridyl)-thien-5-yl)ethylene (DTE) and how changes in packing relate to the changes in the mobility of single crystals. Previous work by us demonstrated the ability to form π-stacked assemblies of an anthracene and a thiophene compound through the use of hydrogen bonds.[19] Here π-stacked assemblies are formed from co-crystallization of DTE and a resorcinol used as an SCCF (Figure 71). To assess

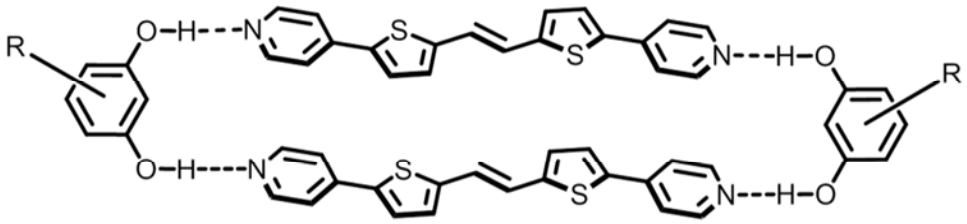

R = 4,6-diCl, 4,6-diBr, 4,6-diI, 4,6-diTbu, 5-Me

Figure 71: Scheme of hydrogen-bonded assembly 2(DTE)·2(SCCF).

the suitability of DTE as an organic semiconductor, DFT calculations were performed to determine the HOMO and LUMO energy levels. The effect the SCCF has on the mobility of the organic semiconductor was studied by obtaining mobility measurements on single crystals of DTE and co-crystals 2(DTE)·2(SCCF) by conductive-probe atomic force microscopy (cp-AFM). The crystals structures of DTE, 2(DTE)·2(4,6-diI-res), 2(DTE)·2(4,6-diBr-res), 2(DTE)·2(4,6-diCl-res), 2(DTE)·2(4,6-ditBu-res), and 2(DTE)·2(5-methyl-res) were solved. Mobility measurements were obtained for single crystals of DTE, 2(DTE)·2(4,6-diCl-res), 2(DTE)·2(4,6-diI-res), and 2(DTE)·2(4,6-ditBu-res).

3.10 Experimental Procedure

3.10.1 Synthesis of DTE

Trans-1,2-bis(2-bromo-thien-5-yl)ethylene (DBrTE) was synthesized as a precursor to *trans*-1,2-bis(2-(4-pyridyl)-thien-5-yl)ethylene (DTE). An Erlenmeyer flask covered in aluminum foil was charged with *trans*-1,2-di(2-thienyl)ethylene (1.0 g, 5.2 mmol), N-bromosuccinamide (1.9 g, 10.6 mmol) in minimal dimethylformamide (7 mL). The solution was allowed to stir at 50^{o}C for 6 hrs in the absence of light. At the end of 6 hrs the solution was poured into an ice water causing a solid to precipitate. The solid was collected by filtration to yield 1.8 g of DBrTE. ^{1}H NMR data for DBrTE ($CDCl_3$, 300 MHz): δ 6.94-9.95 (2H's, d, thiophene), δ 6.80 (2H's, s, ethylene), δ 6.77-6.79 (2H's, d, thiophene).

A 500 mL round-bottom flask was charged with DbrTE (1.8 g, 5.2 mmol) in tetrahydrofuran (150 mL), anhydrous potassium carbonate (15 g, x mmol) in deionized water (100 mL), and $PdCl_2(PPh_3)_2$ (182 mg, 5 mol %) in tetrahydrofuran (150 mL). The mixture was stirred at room temperature for five minutes then 4-pyridineboronic acid (1.6 g, 13 mmol) was added. The mixture was refluxed for five days in the absence of light. At the end of five days a red precipitate was filtered from the solution. The precipitate was further purified by sublimation to yield 715 mg (39 % yield) of DTE. ^{1}H NMR data for DTE (DMSO-d_6, 300 MHz): δ 8.57-8.60 (4H's, dd, pyridine), δ 7.79-7.81 (2H's, d, thiophene), δ 7.62-7.65 (4H's, dd, pyridine), δ 7.37-7.39 (2H's, d, thiophene), δ 7.3 (2H's, s, ethylene).

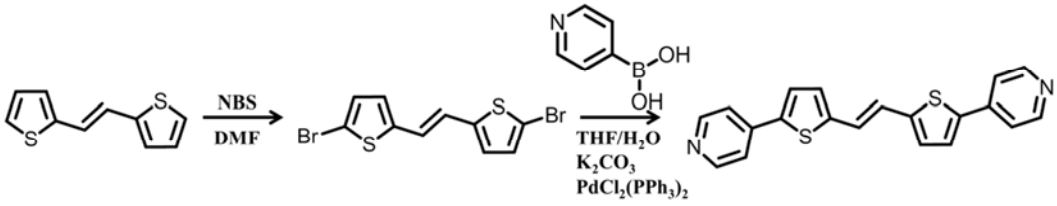

Figure 72: Scheme for synthesis of DTE.

3.10.2 Crystal growth

Single crystals of DTE were obtained *via* vapor growth (Figure 73). To obtain single crystals, the gas preheat zone was set at 255 ^{o}C, the crystallization zone was set at 100 ^{o}C, and N_2 was used as the carrier gas. Co-crystallization experiments with DTE were conducted by dissolving DTE and an appropriate SCCF in a screw-cap vial in a 1:1 ratio in a minimum amount of the appropriate solvent when heated. If no crystals formed upon cooling, the cap was removed such that the solvent could evaporate. Co-crystals involving 4,6-diiodoresorcinol (4,6-diI-Res), 4,6-dibromoresorcinol (4,6-diBr-Res), 4,6-dichlororesorcinol (4,6-diCl-Res), 4,6-ditertbutylresorcinol (4,6-ditert-Res), and 5-methylresorcinol (5-Me-Res) were obtained using a mixture of $CHCl_3$:10% MeOH as a solvent.

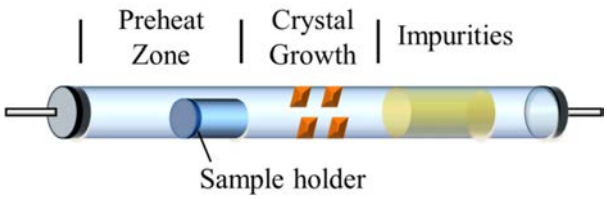

Figure 73: Experimental set-up for vapor growth of crystal.

3.10.3 X-ray crystallography

All crystal data were measured on a Nonius Kappa CCD single-crystal X-ray diffractometer at liquid N_2 temperature using MoK_α radiation (λ = 0.7107 Å). The structures were solved and refined by full-matrix lease-squares based on F^2 parameter. All non-hydrogen atoms were refined using the anisotropic model. H-atoms bonded to carbon atoms were placed in idealized positions based on the hybridization of the belonging carbon atom. H-atoms bonded to O-atoms were placed off of calculations to establish hydrogen bonds to the nearest neighboring hydrogen bond acceptor. Structure

solution was accomplished with the aid of WinGX and refinement was conducted using SHELXL-97 locally implemented on a Pentium-based IBM compatible computer.[126] Relevant crystallographic data for all crystal structures described within this chapter are present in the appendix in tables A-7 through A-9.

3.10.4 Reitveld refinement

Rietveld refinement was done by Dr. Ivan Halasz in collaboration with Dr. Robert E. Dinnebier at the Max-Planck-Institute for Solid State Research, Heisenbergstr. 1, 70569 Stuttgart, Germany. The structure was solved by powder X-ray diffraction (PXRD) on a Bruker D8 Advance powder diffactometer, $CuK\alpha_1$ radiation from a primary Ge(111)-Johannson monochromator, Vantag-1 position sensitive detector with 6^o angle opening; step mode with 0.0085^o per step. A fine powder of the sample was packed in a 0.5 mm borosilicate glass capillary. For better particle statistics the capillary was rotated during data collection. Data was collected in the angle region from 4^o to 75^o in 2θ. Rietveld refinement was performed using restraints on bond lengths and valence angles as well as planarity restraints. All calculations were performed using the program Topas, version 4.1 (Bruker-AXS, Karlsruhe, Germany).

3.10.5 Computational studies

The HOMO and LUMO energies levels were calculated using DFT (b3lyp 6-311G**) with the aid of Spartan 08 implemented on a Pentium-based Dell computer.

3.10.6 Mobility measurements

Mobility measurements were done by Dr. Chandana Karunatilaka in collaboration with Dr. Alexei Tivanski at the University of Iowa. Mobility measurements were made using cp-AFM on nanocrystals of DTE and 2(DTE)·2(SCCF). For the measurements, crystalline samples of either DTE or co-crystals of DTE were suspended in hexanes (~0.2 – 0.3 mg/mL) and deposited on thermally evaporated gold substrates. An irregular

surface of Au substrate was used to decrease the contact resistance and to facilitate the charge injection at the substrate-crystal interface. AFM images were first collected to locate a crystal and to characterize the size and morphology. Diamond- (NanoSensors Inc. CDT-CONTR, tip radius of curvature R~150 nm, spring constant k=0.2 N/m) and platinum-coated (Mikromasch, NSC19/Ti-Pt, tip radius of curvature R~30 nm, spring constant k=0.63 N/m) silicon cantilevers were used to collect the topographic images of the crystals and current *versus* voltage (*IV*) curves and using a commercial atomic force microscope (MFP 3D, Asylum Research, Santa Barbara, CA) with conducting probe module (ORCA, Asylum Research, Santa Barbara, CA). The actual cantilever spring constants were determined with the built-in thermal noise method (*S1*). Diamond coated cantilevers were used as received and the Pt cantilevers were cleaned in piranha solution (1:3 of 30% H_2O_2/98% H_2SO_4) for 2 min, rinsed in ultrapure water (>18 MΩ· cm) for additional 2 min followed by drying under vacuum. The same diamond-coated tip has been used to collect the *IV* response for the co-crystals and the pure components in the

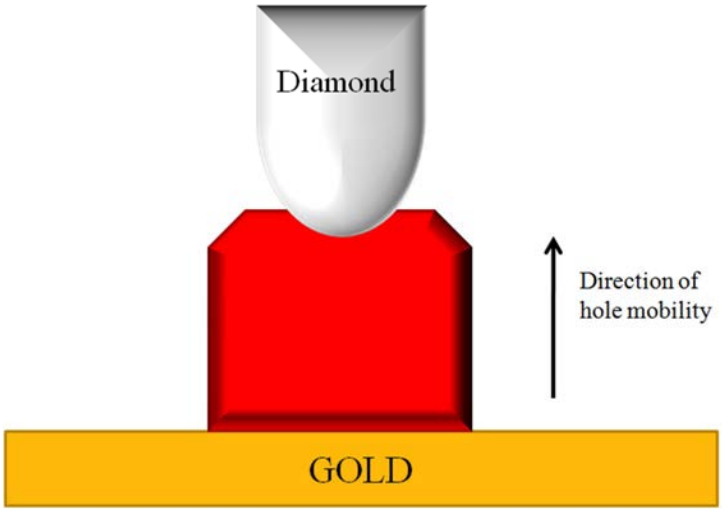

Figure 74: Schematic representation of cp-AFM set up for mobility measurement.

current study, thus avoiding AFM probe-to-probe variation in the measurements arising from the tip geometry (Figure 74). Pt-coated silicon cantilevers were used to check the variation of the charge mobility as a function of probe material, but no significant deviation was observed within the uncertainty of the measurements. The *IV* response of a total of nine different co-crystals and pure components have been measured both in bicyclohexyl solvent medium and in air, but no clear variation has been observed depending on the environment. Current-voltage curves at 50 nN loading force were collected by lowering the AFM tip onto the crystal surface and measuring the vertical current through the crystal as the surface bias was swept typically at a rate of 0.6 V/s with the maximum absolute surface bias of 10 V. A topographic image of the crystal was collected right after the conductive measurements to verify the crystal morphology remained unchanged and the *IV* measurements were collected on the crystal.

3.11 Results and Discussion

3.11.1 Electronic Properties of DTE

The electronic properties of organic semiconductors have an influence over how quickly electrons can travel through the material. The electronic properties also determine if a given semiconductor will function as a p-type or n-type semiconductor. A typical p-type semiconductor has a HOMO level between -4.9 and -5.5 eV. For an n-type semiconductor the LUMO energy level is typically -3 and -4 eV. The HOMO energy level for DTE was determined to be -5.74 eV and the LUMO energy level was calculated as -2.72 eV. The calculations show that DTE has a HOMO/LUMO gap of 3.02 eV which should give DTE a higher stability to air when compared to other organic semiconductors (e.g. pentacene and octithiophene). The energy gap of DTE was a confirmed by UV/Vis spectroscopy (Figure 75). The maximum absorption was found at 411 nm which corresponds to a band gap of 3.02 eV.

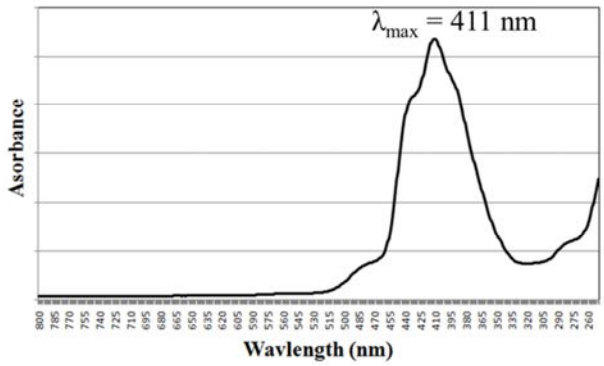

Figure 75: UV/Vis spectrum for DTE.

3.11.2 Single crystal structures of DTE

3.11.2.1 Crystal structure of pure DTE

Single crystals of DTE grown by vapor growth exhibited a blade shape and were yellow in color. DTE crystallized in the monoclinic space group C2/c and packed in a herringbone motif as directed by C-H$\cdots\pi$ interactions (Figure 76). One molecule is located in the asymmetric unit and exhibits a disorder that shifts the molecule along its long axis. The shift causes a thiophene or pyridine to occupy crystallographic equivalent positions. Due to the poor diffraction of the single crystals a R_{obs} = 0.13 was the lowest that could be obtained. To help solve the crystal structure Reitveld refinement was performed on the powder pattern diffraction by Ivan Halasz in collaboration. Reitveld refinement confirmed the correct crystal structure assignment. DTE is relatively planar with the thiophenes and ethylene moieties lying in the same plane and the pyridines slightly tilted out of plane by 3.7^o. The herringbone packing exhibits an angle of 54^o which is similar to what is seen in oligoacenes.

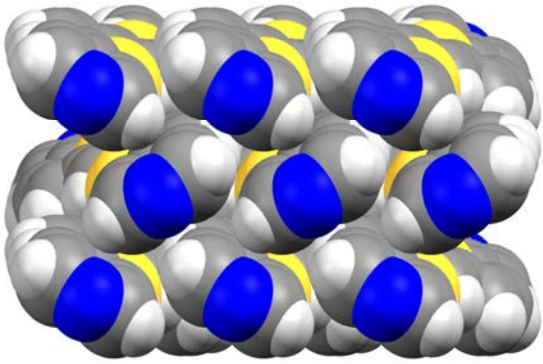

Figure 76: Crystal packing of DTE viewed down the *a*-axis.

3.11.2.2 Co-crystal structures of DTE

A total of five co-crystal structures were collected with DTE with various resorcinols. Specifically, co-crystal structures were collected with 4,6-diI-res, 4,6-diBr-res, 4,6-diCl-res, 4,6-ditbu-res, and 5-methyl-res. All five co-crystals exhibit discrete assemblies in a 1:1 ratio of DTE to SCCF sustained by O-H···N hydrogen bonds (Table 9). The structures for the co-crystals of DTE with 4,6-diI-res, 4,6-diBr-res, and 4,6-diCl-res are isostructural. The use of 4,6-ditbu-res and 5-methyl-res as SCCF yielded unique structures.

Table 9: Interatomic distances and angles for co-crystals involving DTE

SCCF	O···N Bond Distances (Å)	Thiophene Twist from ethylene (°)	Pyridine Twist from ethylene (°)
4,6-diI-res	2.708(2), 2.652(3)	1.6, 1.8	6.6, 11.3
4,6-diBr-res	2.700(3), 2.665(2)	0.0, 2.2	7.2, 10.7
4,6-diCl-res	2.708(3), 2.690(3)	1.0, 2.4	6.6, 9.2
4,6-ditBu-res	2.745(2), 2.800(2)	2.3, 2.6	2.1, 4.2
5-methyl-res	2.752(3), 2.772(3)	1.5, 10.0	11.0, 11.5

3.11.2.2.1 Co-crystal structure of DTE with dihalide resorcinols

Co-crystals of DTE with 4,6-diCl-res, 4,6-diBr-res, or 4,6-diI-res afforded isostructural crystals with a 1:1 ratio of DTE to SCCF in the monoclinic space group $P2_1/n$. The asymmetric unit contains one DTE molecule and one SCCF with no disorder. Discrete assemblies of 2(DTE)·2(SCCF) are formed through O-H···N hydrogen bonds [O···N separation (Å): 2(DTE)·2(4,6-diCl-res) ($O_1\cdots N_1$) 2.708(3), ($O_2\cdots N_2$) 2.690(3), 2(DTE)·2(4,6-diBr-res) ($O_1\cdots N_1$) 2.700(3), ($O_2\cdots N_2$) 2.665(2), 2(DTE)·2(4,6-diI-res) ($O_1\cdots N_1$) 2.708(2), ($O_2\cdots N_2$) 2.652(3)]. Within each discrete assembly the molecules are π-stacked with a distance of 4.0 Å separating the centroid of each molecule (Figure 77).

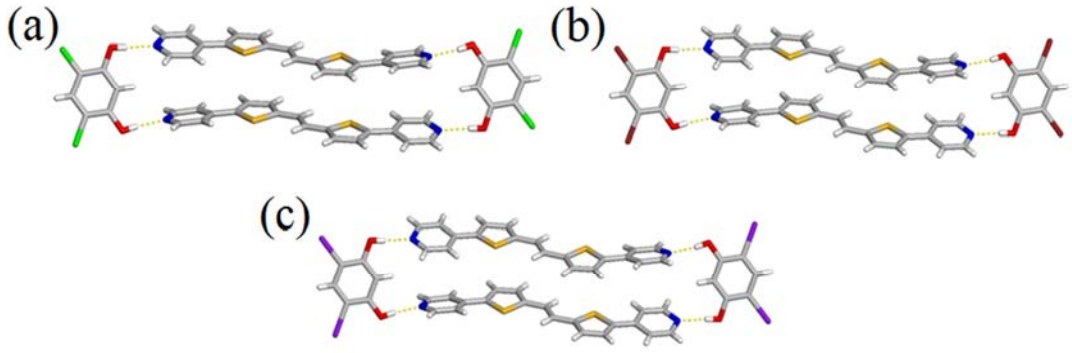

Figure 77: Assembly of a) 2(DTE)·2(4,6-diCl-res), b) 2(DTE)·2(4,6-diBr-res), and c) 2(DTE)·2(4,6-diI-res).

The discrete assemblies are stacked into a 1-D column through O···X interactions [O···X separation (Å): (O···Cl) 2.983, (O···Br) 2.963, (O···I) 3.044)] (Figure 78). The distance between centroids of nearest neighbors in adjacent assemblies is 5.2 Å with 4,6-diCl-res 5.4 Å with 4,6-diBr-res, and 5.7 Å with 4,6-diI-res. The increase in distance between neighboring assemblies is due to the increase in atomic radius of the halide.

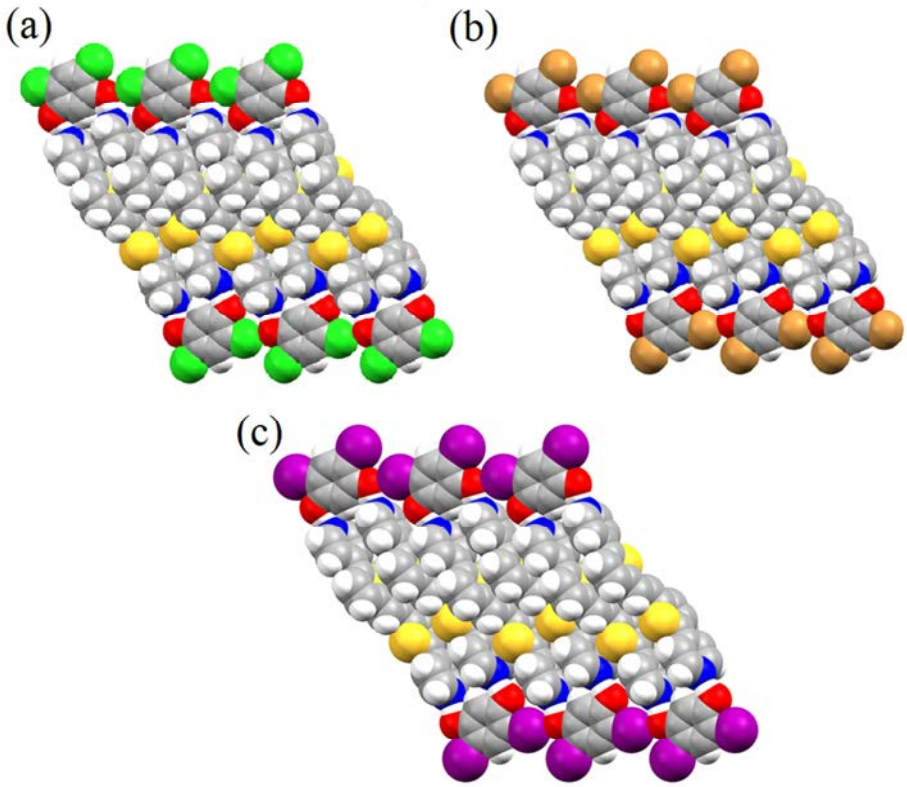

Figure 78: Crystal packing of a) 2(DTE)·2(4,6-diCl-res), b) 2(DTE)·2(4,6-diBr-res), and c) 2(DTE)·2(4,6-diI-res) viewed down *c*-axis.

3.11.2.2.2 Co-crystal structure of 2(DTE)·2(4,6-ditbu-res)

Co-crystallization of DTE with 4,6-ditbu-res afforded red-orange prisms with a 1:1 ratio of DTE to 4,6-ditbu-res in the triclinic space group $P\bar{1}$. The asymmetric unit contains one DTE molecule and one 4,6-ditbu-res with no disorder. 0-D assemblies of 2(DTE)·2(4,6-ditbu-res) are formed through O-H···N hydrogen bonds [O···N separation (Å): (O_1···N_1) 2.745(2), (O_2···N_2) 2.800(2)]. Within each assembly, the DTE molecules are π-stacked with the centroid of each molecule separated by 4.1 Å. The assemblies are

stacked along the *a*-axis with a distance of 6.4 Å separating the nearest DTE molecule in neighboring assemblies (Figure 79).

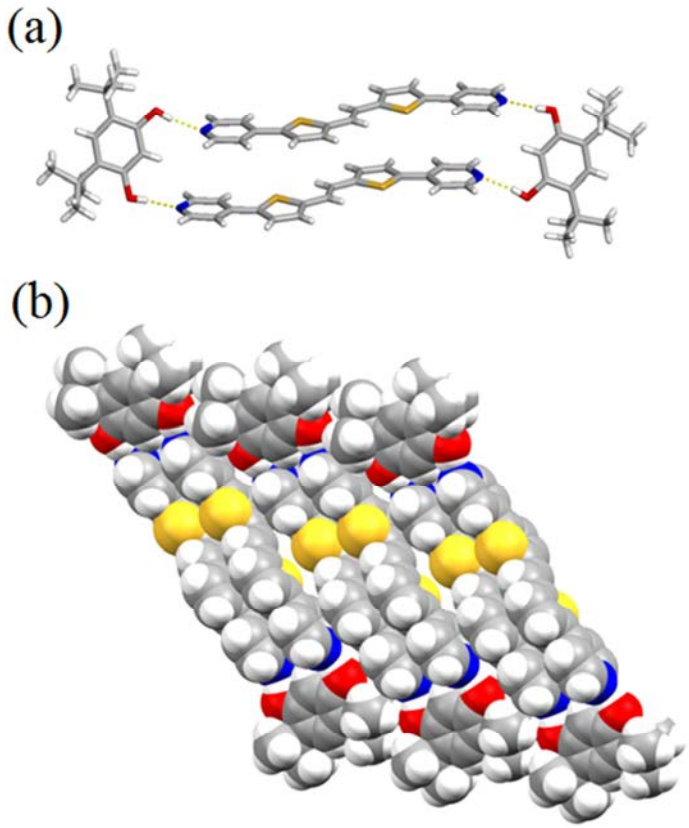

Figure 79: 2(DTE)·2(4,6-ditbu-res) a) assembly and b) crystal packing viewed down *b*-axis.

3.11.2.2.3 Co-crystal structure of 2(DTE)·2(5-methyl-res)

Co-crystallization of DTE with 5-methyl-res afforded red-orange rods with a 1:1 ratio of DTE to 5-methyl-res in the triclinic space group $P\bar{1}$. The asymmetric unit contains one DTE molecule and one 5-methyl-res with no disorder. 0-D assemblies of 2(DTE)·2(5-methyl-res) are formed through O-H···N hydrogen bonds [O···N separation

(Å): ($O_1\cdots N_1$) 2.752(3), ($O_2\cdots N_2$) 2.772(3)]. Within each assembly the DTE molecules are π-stacked with the centroid of each molecule separated by 3.9 Å. The assemblies are stacked along the a-axis with a distance of 5.6 Å separating the nearest DTE molecule in neighboring assemblies (Figure 80).

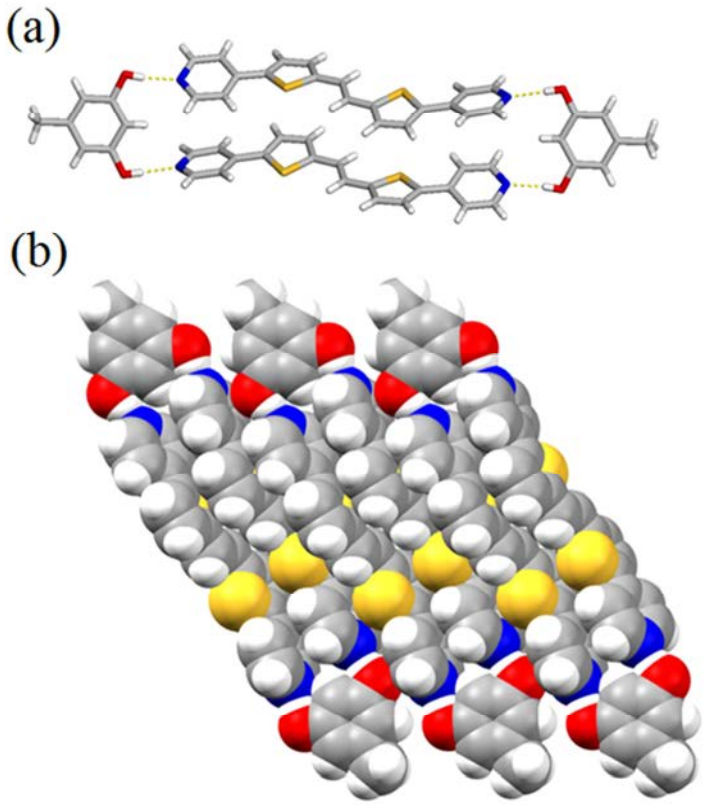

Figure 80: 2(DTE)·2(5-methyl-res) a) assembly and b) crystal packing viewed down *b*-axis.

3.11.3 Mobility of DTE crystals

Mobility measurements were performed on nano-crystals of DTE and co-crystals of 2(DTE)·2(SCCF) using cp-AFM. The current was measured using cp-AFM as the bias voltage was swept between -10 and 10 V. The charge carrier mobility for the nano-

crystal was then extracted from the data using steady-state space charge limited current (SCLC) model.[159] In this model the current is typically dependent on the voltage, carrier density, and carrier mobility of the system at a high positive bias voltage. The SCLC regime can then be approximated as a quadratic with appropriate combinations of electrode material and sample geometry. The quadric regime can be described by using the Mott-Gurney law (Figure 81). Where *I* is the measured current through the crystal, σ

$$I = \frac{9}{8}\sigma\varepsilon\varepsilon_o\mu\frac{V^2}{L^3}$$

Figure 81: Mott-Gurney law.

is the cross-sectional area, ε is the relative dielectric constant, ε_o is the permittivity of free space, μ is the charge mobility, *V* is the applied bias voltage, and *L* is the height of the crystal. The height of the crystal was obtained using AFM topographic imaging and the cross-sectional area was calculated using Hertzian elastic constant model using the spherical tip radius (r ~ 150 nm) and the effective modulus of the tip and crystal. The relative dielectric constant was set to 3, which is common for organic semiconductors. The interface between the diamond tip and crystal surface was found to be a plane-parallel geometry instead of tip-plane geometry which confirms the cubic dependence of height of the crystal on the observed current (Figure 82).

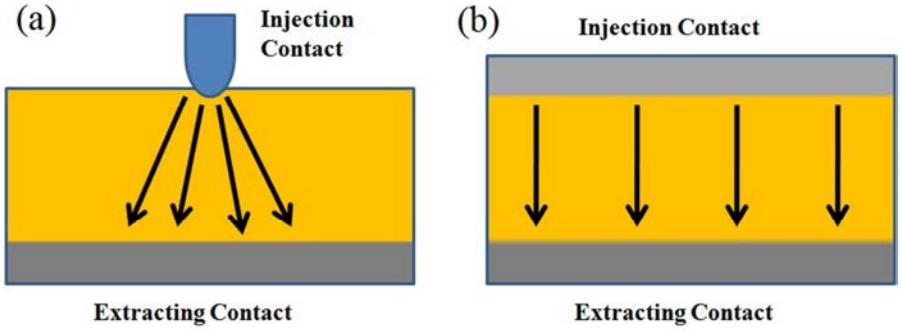

Figure 82: Types of contact geometry a) tip-plane and b) plane-parallel.

3.11.3.1 Mobility measurements of single crystals of DTE

Single crystals of DTE used for cp-AFM were formed by precipitation from a 10:1 chloroform: methanol solution. PXRD pattern was performed on the crystalline powder obtained by precipitation. The obtained PXRD matches the simulated pattern from the single crystal data, thus, the tested crystals match the single crystal data (Figure 83a). For single crystals of DTE, mobility was only observed when a positive surface bias was applied. A maximum current observed for single crystals of DTE was 1 nA at a 10 V bias (Figure 83c). The charge carrier mobility was extracted from the data by using the SCLC model. From the SCLC model the carrier mobility for single crystals of DTE (Figure 83b) was found to be $6.7(\pm 2.1) \times 10^{-4}$ cm^2 V^{-1} s^{-1} (Figure 83d).

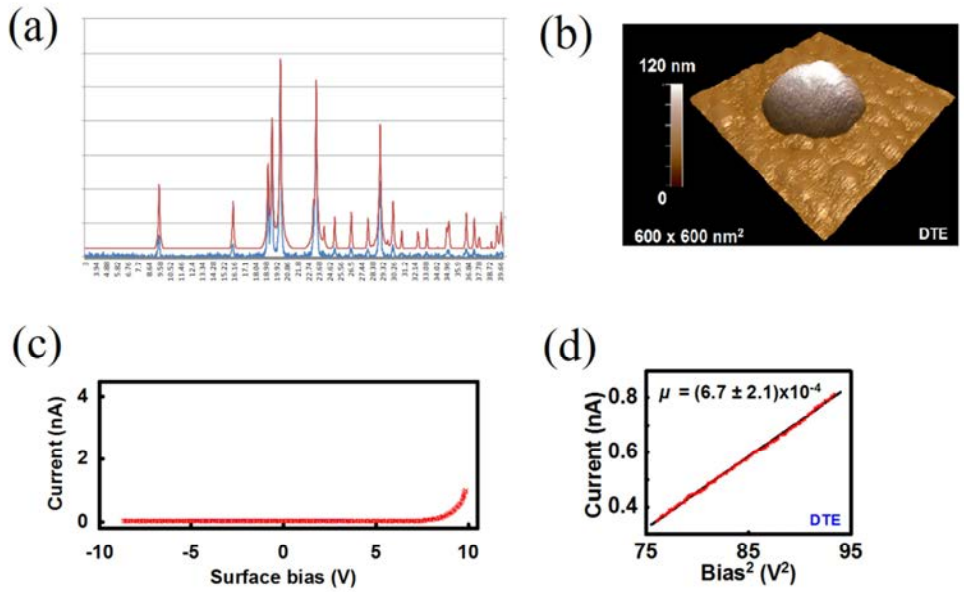

Figure 83: Pure DTE a) red simulated PXRD and blue PXRD of crystalline powder, b) AFM image of nano-crystal, c) measured current versus voltage plot, and d) current versus voltage squared plot.

3.11.3.2 Mobility for crystals of 2(DTE)·2(4,6-diCl-res)

Single crystals of 2(DTE)·2(4,6-diCl-res) studied by cp-AFM were grown from a 10:1 chloroform: methanol solution. The PXRD of the obtained crystals were compared to the simulated PXRD for the single-crystal data to ensure the measured crystals match the single crystal data (Figure 84a). For single crystals of 2(DTE)·2(4,6-diCl-res) (Figure 84b), mobility was only seen when a positive bias was applied suggesting a p-type semiconductor. Mobility was seen at a lower applied bias than the one required to observe mobility in crystals of pure DTE. A 10 fold increase in the maximum current was also observed when comparing the 2(DTE)·2(4,6-diCl-res) co-crystal to pure DTE with an increase from 1 to 10 nA at a 8 V bias (Figure 84c). Plotting the current versus

voltage square and applying the SCLC model a charge carrier mobility was found to be 1.2 (± 0.02) x 10^{-1} cm^2 V^{-1} s^{-1} a 300 fold improvement over pure DTE (Figure 84d).

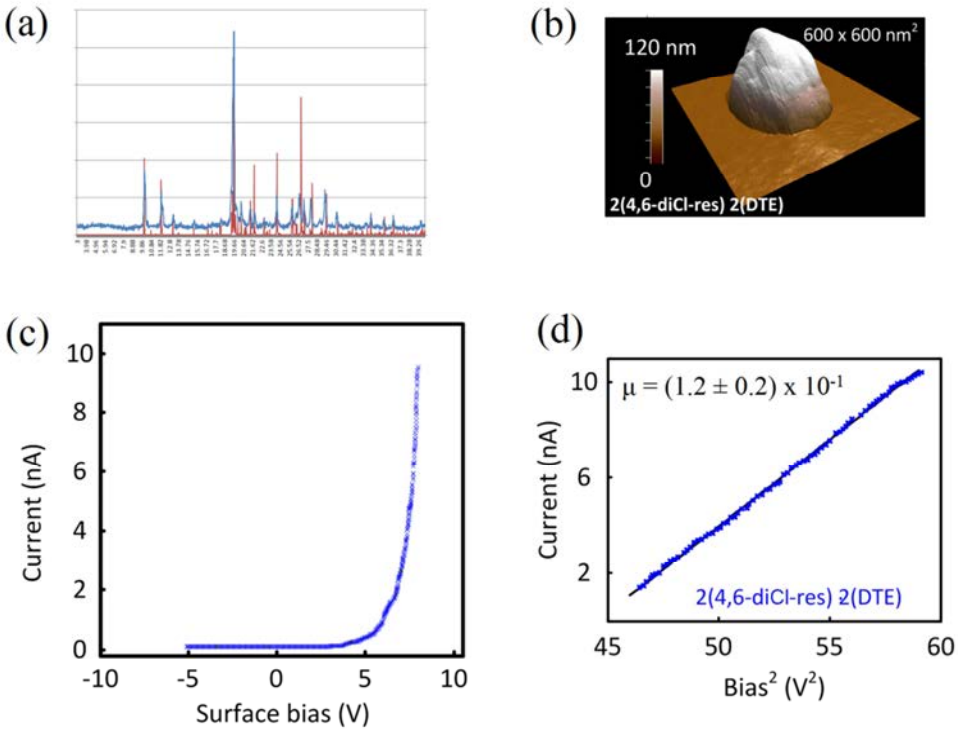

Figure 84: 2(DTE)·2(4,6-diCl-res) a) red simulated PXRD and blue PXRD of crystalline powder, b) AFM image of crystal, c) measured current versus voltage plot, and d) current versus voltage squared plot.

3.11.3.3 Mobility for crystals of 2(DTE)·2(4,6-diI-res)

Single crystals of 2(DTE)·2(4,6-diI-res) studied by cp-AFM were obtained from evaporation of a 10:1 chloroform: methanol solution. The PXRD of the obtained crystalline powder was compared to the simulated PXRD from the single crystal data (Figure 85a). The PXRDs match so the crystal structure of the tested crystals matches that of the collected single crystal. The mobility of single crystals of 2(DTE)·2(4,6-diI-

res) (Figure 85b) was only seen when a positive bias was applied. A maximum current of 5.3 nA was observed at a bias of 8 V, lower than the one observed for 2(DTE)·2(4,6-diCl-res) but higher than DTE alone (Figure 85c). Plotting the current versus voltage squared and applying the SCLC model, the charge carrier mobility was found to be 2.1 (± 0.4) x 10^{-2} cm^2 V^{-1} s^{-1} (Figure 85d).

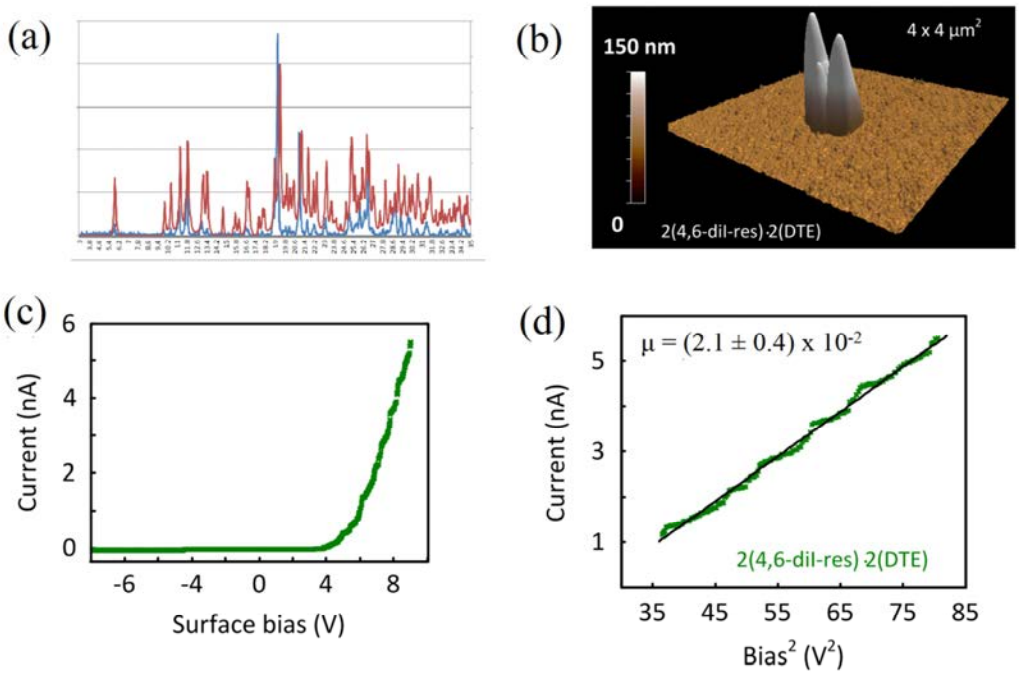

Figure 85: 2(DTE)·2(4,6-diI-res) a) red simulated PXRD from crystal and blue PXRD of crystalline powder, b) AFM image of crystal, c) measured current versus voltage plot, and d) current versus voltage squared plot.

3.11.3.4 Mobility for crystals of 2(DTE)·2(4,6-ditbu-res)

Single crystals of 2(DTE)·2(4,6-ditbu-res) measured by cp-AFM were obtained by evaporation of a 10:1 chloroform: methanol solution. The PXRD of the obtained crystals matches the simulated PXRD from the single crystal data (Figure 86a). This

means that the crystals used for the mobility measurements match the crystal used for single crystal diffraction. The mobility of single crystals of 2(DTE)·2(4,6-ditbu-res) was only seen when a positive bias was applied. A maximum current of 2.5 nA was observed at a bias of 5 V, the lowest one observed for a co-crystal of DTE but still higher than DTE alone (Figure 86c). Plotting the current versus voltage square and applying the SCLC model the charge carrier mobility was found to be 5.9 (± 2.6) x 10^{-3} cm^2 V^{-1} s^{-1} (Figure 86d).

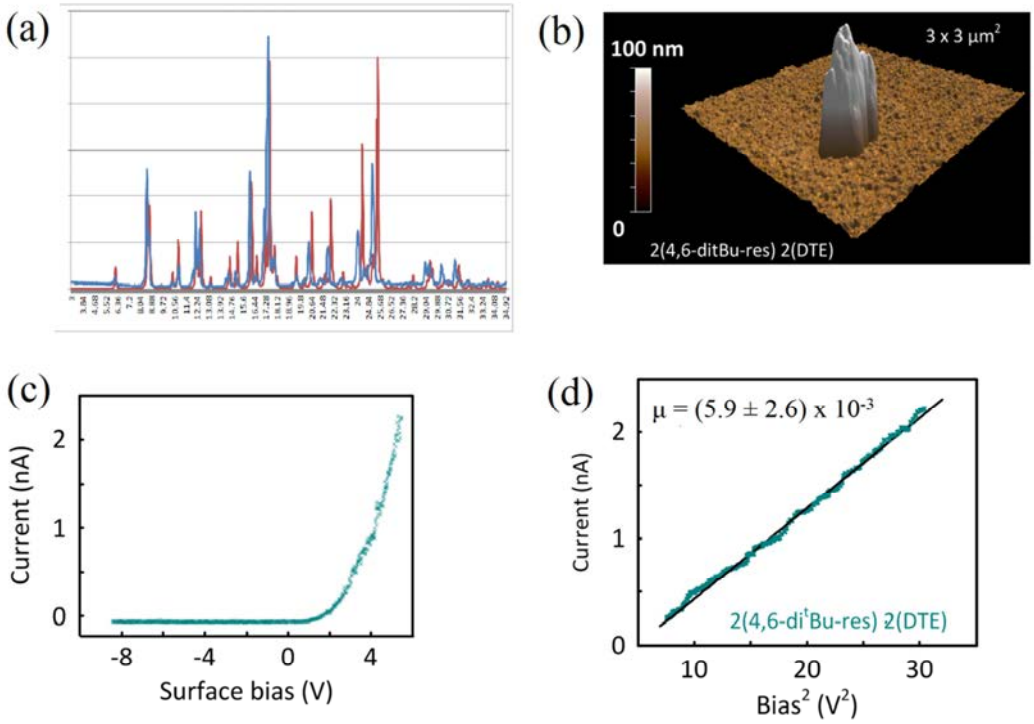

Figure 86: 2(DTE)·2(4,6-ditBu-res) a) red simulated PXRD from crystal and blue PXRD of crystalline powder, b) AFM image of crystal, c) measured current versus voltage plot, and d) current versus voltage squared plot.

3.11.4 Effect of SCCF on Mobility

The introduction of the SCCF directs DTE into π-stacked assemblies expected to increase the orbital-orbital interactions between neighboring molecules. The increase in orbital-orbital interaction should increase the effective electronic coupling matrix and lead to a higher mobility. Notably, the SCCF is not expected to act as a semiconductor. Therefore, in order for the SCCF to improve the overall mobility, the benefit from improved π-overlap must outweigh the possible impedance the SCCF causes on the mobility. Table 10 summarizes all of the relevant intermolecular distances and mobilities for DTE and the co-crystals test by cp-AFM.

Table 10: Summary of distances and mobilities measured by cp-AFM

SCCF	Stacking angle (^{o})	Centroid distance to closest molecule (Å)	Between assembly centroid distance (Å)	Measured mobility ($cm^2V^{-1}s^{-1}$)
DTE	54.6	3.8	N/A	$6.7 (\pm 2.1) \times 10^{-4}$
2(DTE)·2(4,6-diCl-res)	0.0	4.0	5.2	$1.2 (\pm 0.2) \times 10^{-1}$
2(DTE)·2(4,6-diI-res)	0.0	4.0	5.7	$2.1 (\pm 0.4) \times 10^{-2}$
2(DTE)·2(4,6-ditBu-res)	0.0	4.1	6.4	$5.9 (\pm 2.6) \times 10^{-3}$

The mobility measurements show that the inclusion of a SCCF is a viable way to improve the mobility of an organic semiconductor. The stacking angle for DTE molecules was reduced from 54^o in the pure DTE to 0^o for the co-crystals. According to theory, the reduction in stacking angle to 0^o will create an increase in the effective coupling matrix leading to a higher mobility. The increase in the effective coupling matrix is supported by the increase in mobility for each co-crystal when compared to pure DTE. To determine how the effective coupling matrix changed between the co-crystals, the interaction between assemblies must also be compared.

The co-crystals 2(DTE)·2(4,6-diCl-res) and 2(DTE)·2(4,6-diI-res) are isostructural. The difference between the two crystals is that the iodine atoms cause the distance between DTE molecules of neighboring assemblies from 5.2 and 5.7 Å. The increase in distance accounts for the lower mobility in the 2(DTE)·2(4,6-diI-res) crystals compared to crystals of 2(DTE)·2(4,6-diCl-res). Crystals of 2(DTE)·2(4,6-ditbu-res) had the lowest mobility out of the three co-crystals measured. There are two reasons for the observed decrease in mobility. First, the distance between DTE molecules of neighboring assemblies is further increased. Secondly, there is an increased shift along the long and short axis of DTE when 4,6-ditbu-res is used as the SCCF. The closest DTE molecules of neighboring assemblies are not directly over each other in a column. In the crystals of 2(DTE)·2(4,6-diCl-res) and 2(DTE)·2(4,6-diI-res), there is a slight shift along the long axis creating thiophene-pyridine overlap (Figure 87a). In the crystals of

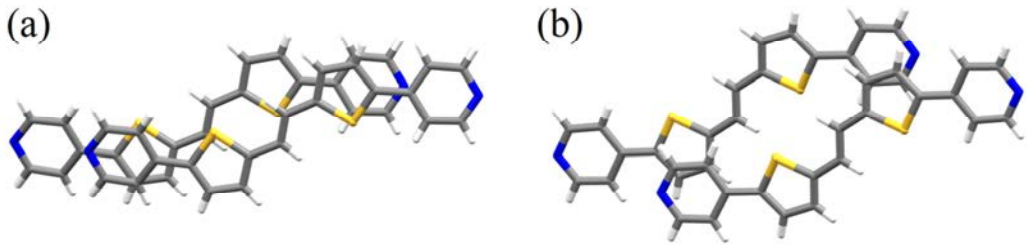

Figure 87: Overlay of DTE between neighboring assemblies for a) 2(DTE)·2(4,6-diCl-res) and b) 2(DTE)·2(4,6-ditbu-res).

2(DTE)·2(4,6-ditbu-res), there is larger shift along the long axis and also shift along short axis of DTE (Figure 87b). The shifts decrease the overlap of DTE molecules between neighboring assemblies. The increase in distance between assemblies and shifts account for the decrease in mobility of 2(DTE)·2(4,6-ditbu-res) compared to 2(DTE)·2(4,6-diCl-res).

Another possible effect the SCCF has on improving the mobility of the material is helping to effectively funnel the charge through a column by creating a preferred charge transport route. A top down view of the created columns shows that each DTE molecule is surrounded by six SCCF molecules (Figure 88). A 70^{o} angle exists between the plane of the DTE molecule and plane of the SCCF molecule. The angle between a DTE and 4,6-diCl-res molecule has a lower effective electronic coupling value then the angle between two DTE molecules. Also the SCCF is a small molecule, with a smaller conjugated core when compared to DTE, making it poorer semiconductor then DTE. The prevention of the herringbone packing motif and the formation of π-stacked assemblies due to the inclusion of the SCCF are the most likely causes for the improve mobility.

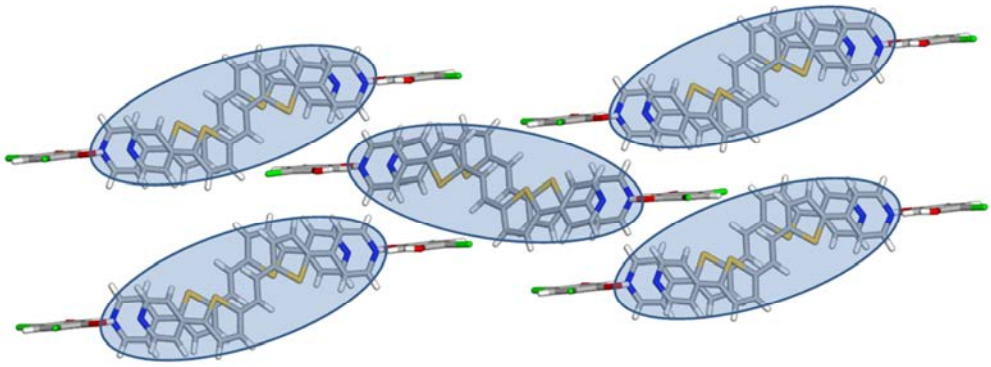

Figure 88: Top view of 2(DTE)·2(4,6-diCl-res) showing formation of isolated stacked columns.

3.12 Conclusion

Here, we demonstrated the ability to achieve π-stacked assemblies of DTE along with the ability to obtain 1-D columns through O···X interactions. Each SCCF directed two DTE molecules into a π-stacked assembly with the mean planes separated by approximately 4.0 Å. The packing of the assemblies within the crystal was dependent on

the substituents placed on the resorcinol. Mobility measurements on the single crystals conducted by cp-AFM allowed us to probe the effect of the SCCF on mobility. We discovered that the addition of an SCCF to form an organic semiconductor co-crystal is a viable way to improve the mobility of an organic semiconductor. We were able to achieve mobility improvements up to 200 fold through the addition of a SCCF. The packing of the assemblies within the crystal determined how much of an improvement in mobility was seen. When co-crystallized with 4,6-diCl-res the distance between planes of DTE in neighboring assemblies was only 3.4 Å with only a slight shift along the long axis of the molecule. As the distance increased and overlap decreased between DTE molecules in neighbor assemblies there was a reduction in mobility compared to 2(DTE)·2(4,6-diCl-res) co-crystal. However, even with bulky tertiary-butyl groups in the co-crystal, an improvement in the mobility was still seen when compared to crystals of only DTE.

CHAPTER 4: CO-CRYSTALS AS MEDIA TO ISOLATE AND CHARACTERIZE CONFORMATIONS OF OLIGOTHIOPHENES

4.1 Introduction

Polymorphism occurs when a molecule packs in two or more crystal structures. Flexible organic semiconductors, such as oligothiophenes, have backbones that can adopt multiple conformations, which can impact solid-state packing. Research has shown that changes in conformation can lead to changes in electronic properties.[160,161] Oligothiophenes can exhibit rotational disorder in the oligothiophenes backbone in which the more stable *anti*-conformation converts to a *syn*-conformation (Figure 89). The ability to control the major conformation present in a solid-state material is important for control of charge transport. Moreover, a facile non-destructive testing method for identifying conformations of thiophenes in solids could be used to screen polymorphs and, eventually, lead to a more rational design of organic semiconducting materials.

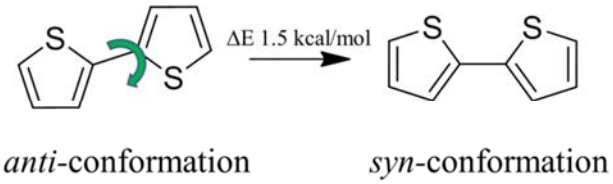

Figure 89: Torsional conversion of bithiophene from the *anti*-conformation to the higher energy *syn*-conformation.

4.2 Overview

The chapter herein will cover an approach to utilize semiconductor co-crystals as a means to achieve different conformations of a given bithiophene and the use of IR spectroscopy to identify conformations of the bithiophene in the solid. During the course

of our studies to develop co-crystals based on a bithiophene, we have determined that a higher energy conformation of the bithiophene can be crystallized out by switching the SCCF used to obtain the co-crystals. The addition of the SCCF can alter the crystal packing to stabilize the higher energy conformation in the solid. These different conformations of the bithiophene have been determined to affect the atomic vibrations that are IR active. The use of a SCCF could then act as a way to select a conformation of an oligothiophene present in a solid.

4.3 Polymorphism

It has been stated that the number of polymorphs of a molecule is related to the number of different crystallization experiments performed.[162] As the role of organic semiconductors increases in electronics so likely will the number of polymorphs. A molecule exhibits polymorphism when the molecule can exist in two or more crystal packings. Polymorphism has been observed in both rigid semiconductors (i.e. pentacene) as well as flexible semiconductors (i.e. oligothiophenes) and has been a major area of study in pharmaceutical chemistry for a number of years.[10,163,164] The prevalence of study is because physical properties exhibited in the solid state (e.g. dissolution, color, stability, charge mobility) have been shown to change with the crystal packing.[165,166] The control of polymorphism in related thin films is important because the presence of multiple polymorphs can induce defect sites which would reduce overall mobility of the film. Flexible systems can also exhibit conformational polymorphism.

Since polymorphs exist only in the solid state, the molecular conformation in the solid is not necessarily the global minimum found in the gas phase.[167] Hence, molecules that possess torsional freedom have multiple conformations that can be isolated by crystallization. Conformational polymorphism occurs when polymorphs are caused by a change in molecular conformation.[167,168] The ability to change conformation gives

Table 11: Conformational polymorphs of oligothiophenes

Polymorph I	Polymorph II	Ref
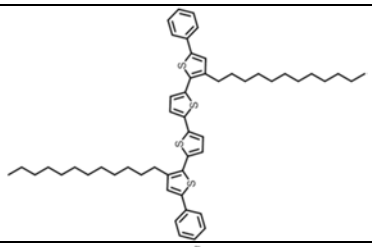	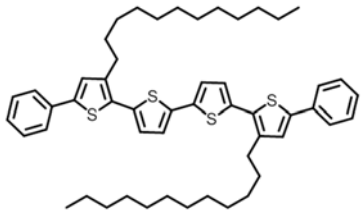	170
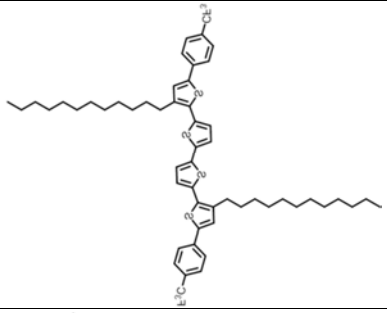	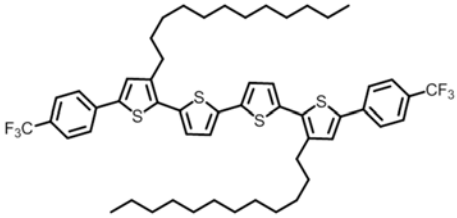	170
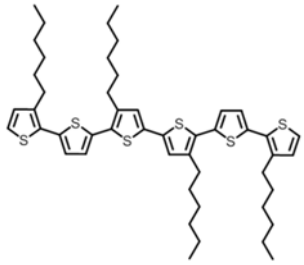	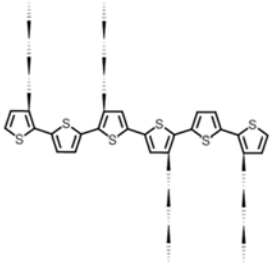	161
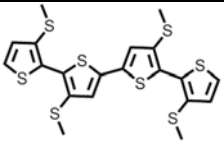	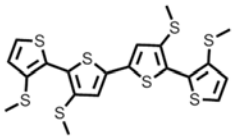	171, 172
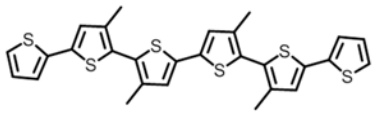	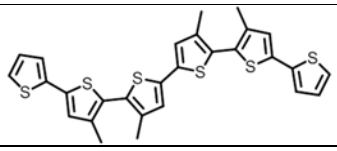	174
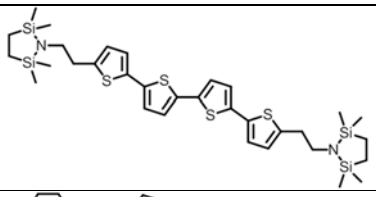	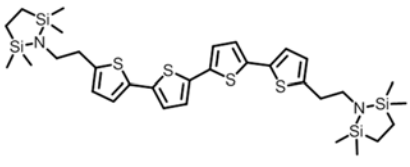	176
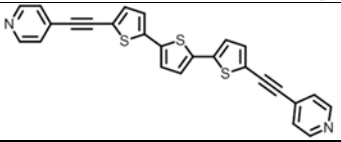	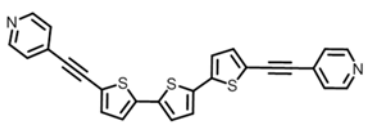	178

conformationally flexible molecules access to a greater number of packing arrangements compared to rigid molecules.[169] The flexible nature of oligothiophenes makes them more prone to conformational polymorphism then the rigid oligoacenes. Alternate conformations and packing arrangements can lead to changes in charge mobility in oligothiophenes.

4.3.1 Conformational Polymorphism in oligothiophenes

Nine oligothiophenes have been found to exhibit polymorphism. Of the nine, seven are conformational polymorphs (Table 11). The conformational changes arise from either rotations in the oligothiophene backbone or a change in the orientation of the substituents relative to the backbone.[161,170] The twisting within the oligothiophene backbone can affect the overlap of the conjugation π-system. The loss of planarity causes an increase in the band gap of the material by reducing the number of p-orbitals in conjugation. Changes in conformation of the substituents can affect the overall packing of the materials and can also affect the HOMO/LUMO energy levels. However, since twisting has an effect on the HOMO/LUMO energy levels of oligothiophene[27] we will focus on conformational polymorphs in which changes in the oligothiophene backbone occur.

4.3.1.1 β-substituted oligothiophenes

Tetramethylsulphanylquarterthiophene (TMS4T), synthesized by Barbarella *et al*. in 1996, was the first substituted thiophene to exhibit conformational polymorphism. Two polymorphs of TMS4T are known.[171,172] The first polymorph was reported as orange crystals that crystallize in the triclinic space group $P\bar{1}$ (Figure 90a). The second polymorph was reported as yellow crystals in the monoclinic space group $P2_1/c$ (Figure 90b). In the orange polymorph, the interior thiophene rings lie in a co-planar *anti*-conformation with the exterior rings being rotated by 28 degrees. The yellow polymorph, however, exhibits a *syn-anti-syn*-conformation, an uncommon conformation

for oligothiophenes, with outer rings twisted by 57^{o} with respect to the co-planar interior thiophene rings. The strong deviation from planarity causes the yellow polymorph to adopt an unusual sandwich-type packing. The orange polymorph adopts the more common herringbone packing. Also, the methylsulphanyl groups crystallize planar to respective rings in the orange polymorph allowing for electron donation into the

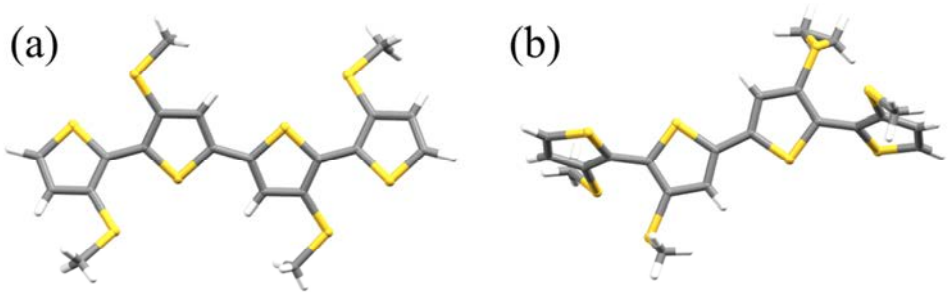

Figure 90: Conformational polymorph of TMS4T a) orange polymorph and b) yellow polymorph.

thiophene rings from the adjacent S-atoms. The deviation from planarity of the rings and change in methylsulphanyl group orientation cause the HOMO-LUMO gap to be blue shifted by 140 nm in the yellow polymorph compared to the orange polymorph.[173]

Similar to the previously discussed TMS4T, tetramethylsexithiophene (TM6T) has been determined to exhibit two conformational polymorphs.[174] TM6T shares the same β-substitution pattern as TMS4T with substitutions on the interior four thiophene rings. The two polymorphs of TM6T appear as either orange-yellow or yellow-green crystals. The orange-yellow polymorph crystallizes in an all *anti*-conformation in the triclinic space group $P\bar{1}$ (Figure 91a). The yellow-green polymorph crystallizes in an *anti-syn-anti-syn-anti*-conformation in the monoclinic space group C2/c (Figure 91b). Each polymorph of TM6T shares similar packing and optical properties compared to the

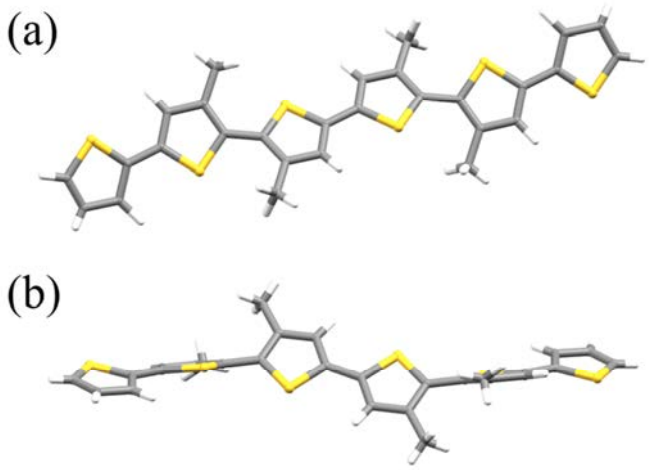

Figure 91: conformational polymorph of TM6T a) obtained as orange-yellow crystal and b) obtained as yellow-green crystal.

TMS4T counterpart. The torsion angle between the *syn*-thienyl rings in the yellow-green polymorph is 52.2^{o}, compared to 57.0^{o} for the *syn*-conformation of TMS4T. The difference in conformation leads to differences in the packing and properties of each crystal. The orange-yellow polymorph crystallizes such that the coplanar interior rings lie face-to-face with the corresponding subunit of neighboring molecules. Meanwhile, the yellow-green polymorph packs in a sandwich packing, in which the molecules roughly face each other and are shifted by one molecule. The differences in packing and conformation lead to a HOMO-LUMO gap that is 210 meV higher for the yellow-green polymorph when compared to the orange-yellow polymorph.[173]

4.3.1.2 α-substituted oligothiophenes

The first α-substituted oligothiophene to exhibit conformational polymorphism is 5,5‴-bis[(2,2,5,5-tetramethyl-1-aza-2,5-disila-1-cyclopentyl)ethyl]-2,2′:5′,2″:5″,2‴-quarterthiophene (Aza4T). Aza4T crystallizes in a thin film into either a *syn-anti-syn* or

all-*anti* conformation (Figure 92). Surprisingly, the *syn*-*anti*-*syn*-conformation is the stable conformation.[175,176] The stability of the *syn*-*anti*-*syn*-conformation compared to the all-*anti*-conformation is attributed to the presence of the bulky terminal groups. Single crystals suitable for structure determination have only been obtained for the *syn*-*anti*-*syn*-conformation. All four thiophenes in the structure are co-planar, unlike the β-substituted *syn*-conformations which exhibit large twists in the oligothiophene backbone. The molecules pack in an edge-to-face fashion in the solid.[177] The all-*anti*-conformation was discovered in a thin film due the different film morphology of the two polymorphs. The *syn*-*anti*-*syn*-conformation forms 3D grains during thin film growth and the all-*anti*-conformation film is dominated by growth of small islands. The percentage of the two conformations in a film are depended on substrate temperature and deposition rate.[175]

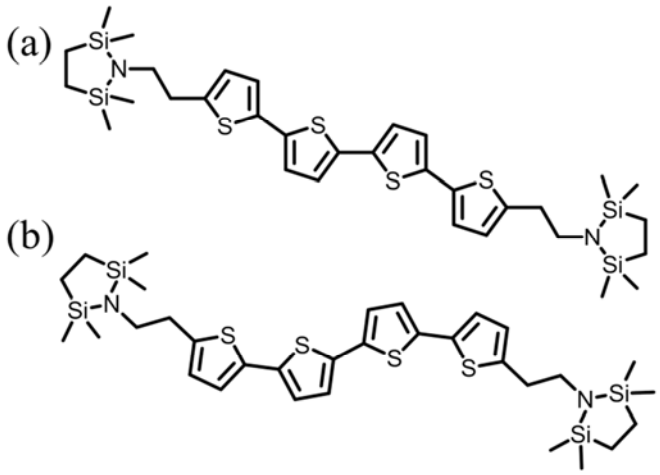

Figure 92: Aza4T a) S-all-*anti*-conformation and b) S-*syn*-*anti*-*syn*-conformation.

An additional α-substituted oligothiophene that exhibits conformational polymorphism is 2,5″-bis(4-pyridyl-ethynyl)-5,2′,5′,2″-terthiophene (DPTT).[178] Two different polymorphs have been discovered by us for DPTT; namely, an achiral orange and a chiral yellow form. The achiral form exhibits an all-*anti*-conformation, while, the

yellow form exhibits a rare *syn-anti*-conformation. The all *anti*-conformation has inter-ring twist angle of 13.2^{o} while the *syn-anti*-conformation has inter-ring twist of 8.3 and 7.2^{o} for the *syn*- and *anti*-rings, respectively (Figure 93).[178] The two polymorphs differ in the amount of π-overlap present in each crystal. The achiral phase demonstrates π-π interactions between thiophene rings of neighboring molecules along with C-H··π interactions between thiophene rings and pyridines. The chiral phase, however, only contains C-H··π interactions between nearest neighbors. The π-π interactions in the achiral phase are expected to aid in possible charge transport.

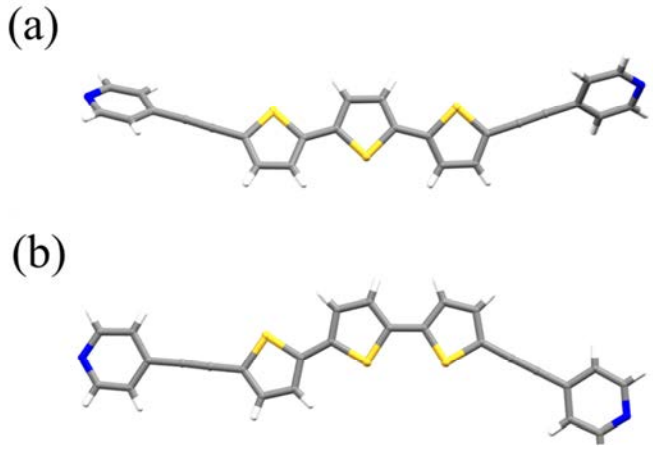

Figure 93: DPTT a) all-*anti*-conformation, b) *anti-syn*-conformation.

4.4 Effect of changes in conformation on band gap and ionization potential

It has been established that solid-state packing has an impact on the charge carrier mobility of an organic semiconductor.[27] For rigid organic semiconductors, such as oligoacenes, molecular packing is the main factor in determining charge mobility in addition to the electronic properties of the molecule. However, the conformations of

flexible organic semiconductors can also affect mobility. In particular, the crystal structure of bithiophene contains a slight disorder in which the higher energy *syn*-conformation has a 15% occupancy.[179] Calculations have shown that the *syn*-conformation is 0.88 kcal/mol higher in energy than the *anti*-conformation.[180] The conformation of oligothiophenes plays an important role in the HOMO/LUMO band gap of the molecule. A large twist in the oligothiophene backbone creates a disruption in the conjugated p-orbitals (Figure 94). Moreover, calculations have shown that shortening the conjugation of a system increases the HOMO/LUMO band gap.[27] The band gap of

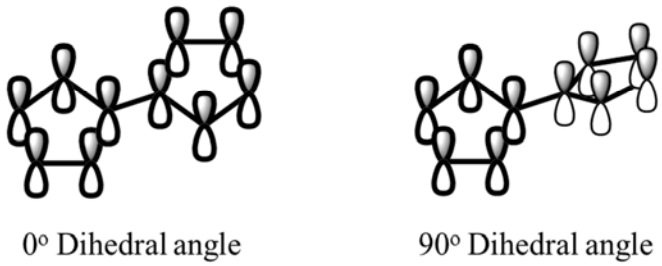

Figure 94: Scheme of conjugation of p-orbitals at 0^o and 90^o dihedral angle.

bithiophene is at a minimum when the thiophenes are co-planar and a maximum when the two thienyl moieties exhibit a 90^o dihedral angle.

4.5 Orbital splitting versus orientation of bithiophene dimer

The vibrational coupling constant can be estimated from the energy difference of the orbitals created by the interaction of the frontier orbitals of two molecules when in a dimer.[181] The degree of overlap between the HOMOs (or LUMOs) of neighboring molecules determines the degree of splitting of the HOMO and HOMO-1 (or LUMO and LUMO+1) (Figure 95). For p-type semiconductors the vibrational constant is approximated from the splitting of the HOMOs, and for n-type semiconductors it is

approximated from the splitting of LUMOs. At different orientations, the amount of orbital overlap between molecules changes which causes a change in the degree of orbital splitting.

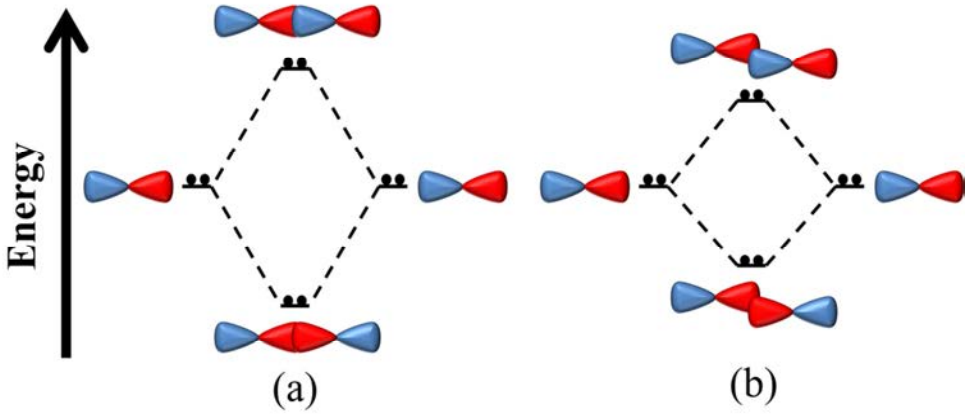

Figure 95: Orbital splitting scheme for a) maximum orbital overlap and b) partial orbital overlap.

When an 180^{o} rotation occurs around the single bond in bithiophene the *anti*-conformation switches to a *syn*-conformation. The change in conformation causes an overall change in orientation of the bithiophene dimer. When both bithiophenes of a dimer are present in the *anti*-conformation, it is possible for both S-atoms to be stacked directly above each other. If one of the bithiophenes is in a *syn*-conformation, then the arrangement is unattainable if π-π stacking is to be maintained (Figure 96). A change in orientation will change the frontier orbitals that interact in the dimer. Calculations have shown that dimers of bithiophene can show a broad range of splitting values despite having structure similarities.[181] The range makes being able to isolate and study different conformations of bithiophenes important to further the understanding of charge transport in organic semiconductor materials.

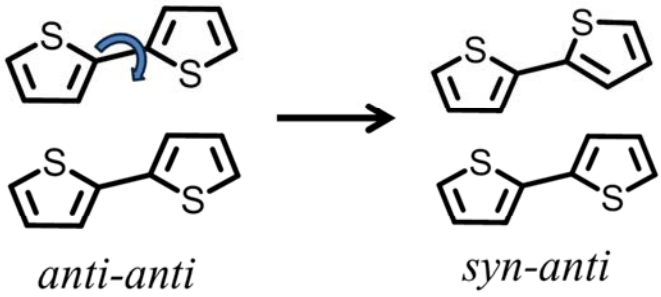

Figure 96: Change in bithiophene dimer with rotation of one to *syn*-conformation.

4.6 Use of spectroscopy to identify the conformations of thiophenes

4.6.1 Calculated infrared spectrum for bithiophene

Calculations have shown that different spectral properties are expected for the *anti*-conformation and *syn*-conformation of bithiophene. Specifically, the *syn*-conformation is expected to exhibit extra IR active stretching modes owing to a loss of symmetry. Millefiori *et al.* calculated the IR spectra for five different conformations of bithiophene; namely, *anti*, *anti-gauche*, perpendicular, *syn-gauche*, and *syn* (Figure 97).[182] The dihedral angle for the bithiophene was constrained to 180^{o} for the *anti*-conformation, 148^{o} for the *anti-gauche* conformation, 90^{o} for the perpendicular, 36^{o} for the *syn-gauche* conformation, and 0^{o} for the *syn*-conformation. It was found that as the dihedral angle decreases from 180 to 0^{o}, changes in the $C_{\beta}=C_{\alpha}-C_{\alpha'}=C_{\beta'}$ carbons ($C_{\alpha}-C_{\alpha'}$ are the carbons in the single bond connecting the thiophenes), anti-symmetric C-S (ν-C-S) stretches and out-of-plane C-H (γ-C-H) bends occurred.

In particular, the peak at 1244 cm^{-1} of the *anti*-conformation corresponds to the deformation of the $C_\beta=C_\alpha-C_{\alpha'}=C_{\beta'}$ fragment. The peak at 1192 cm^{-1} correlates to the same deformation but is only IR active in the perpendicular-, *syn-gauche-*, and *syn*-conformation, but absent in the *anti*-conformation. The appearance of the peak at 1192 cm^{-1} is due to the dipoles of the thiophenes no longer pointing in opposite directions. Another difference in the spectra arises from changes in the ν-C-S and γ-C-H, which

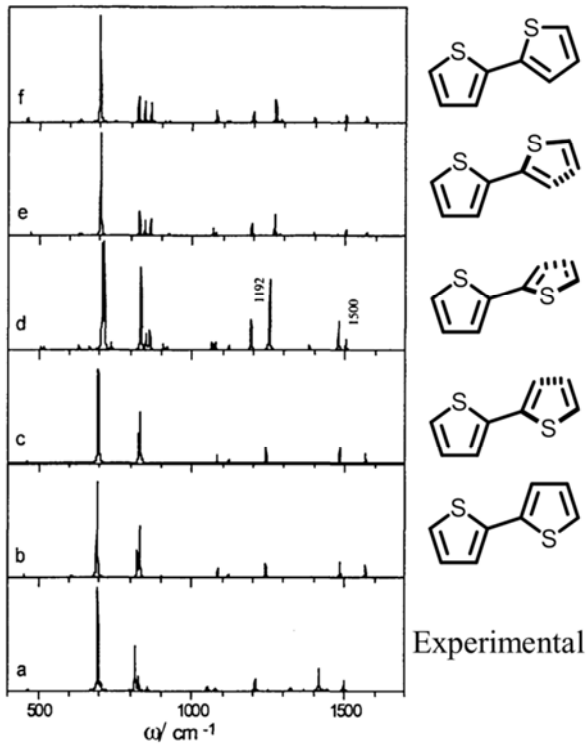

Figure 97: Calculated IR spectrum of A) experimental B) *anti*-, C) *anti-gauche*-, D) perpendicular-, E) *syn-gauche*-, and F) *syn*-conformation. Reprinted with permissions from Wiley.

occur between 830 - 870 cm^{-1}. The *anti*-conformation of bithiophene exhibits a peak at 863 cm^{-1}, which corresponds to ν-C-S and γ-C-H stretches. The perpendicular-, *syn-gauche-*, and *syn*-conformation ν-C-S and γ-C-H stretches occur at 833, 850 and 862 cm^{-1}, that result in extra peaks in the 830 – 870 cm^{-1} region of the spectra. The changes are

consistent to the experimental IR of bithiophene. Crystallographic evidence suggests that the *anti*-conformation makes up 85% of the bithiophene molecules, with the *syn*-conformation making up 15%.[179] The small amount of the *syn*-conformation explains the low intensity of the corresponding peaks in the IR spectrum of bithiophene.

4.6.2 Experiments for detecting thiophene conformations using IR spectroscopy

Hotta *et al.* discovered that Aza4T exhibits conformational polymorphism in which one polymorph exhibit all-*anti*-conformation and the other exhibits an *syn*-*anti*-*syn*-conformation.[175] In addition to our work,[178] the study is one of the few examples of an α-substituted oligothiophene that exhibits conformational polymorphism. Controlling the deposition temperature and rate determined which polymorph was the major conformation in a thin film. It was determined that the conformations could be distinguished by IR spectroscopy. An IR active C=C vibration at 1440 cm^{-1} in the all-*anti*-Aza4T shifts to 1460 cm^{-1} in the *syn*-*anti*-*syn*-Aza4T spectrum (Figure 98).

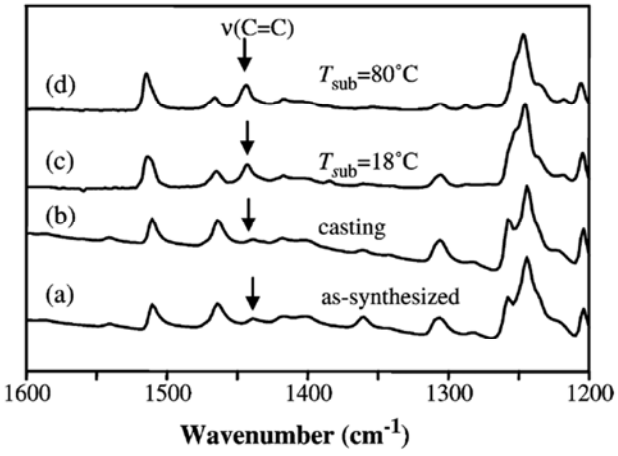

Figure 98: Infrared spectra of Aza4T a) as synthesized, b) casting, c) T_{sub}=18 ^{o}C , and d) T_{sub}= 80 ^{o}C. Reprinted with permission from J. Heterocyclic. Chem.

4.7 Chapter Focus

The focus of this chapter is on the use of co-crystallization as a means to achieve different conformations of a given thiophene in the solid state and the use of IR spectroscopy to identify the conformations. Specifically, the chapter will focus on co-crystallization of *trans*-1-(4-pyridyl)-2-(5-(2,2'-bithienyl))ethylene (P2TE) with different SCCFs based on resorcinol affects the conformation of the bithiophene moiety, and the use of IR spectroscopy to detect the change (Figure 99). It was discovered that when P2TE was co-crystallized with different SCCFs, the amount of the bithiophene moiety in the higher energy *syn*-conformation in the co-crystal was different. Specifically, the amount of the bithiophene in the *syn*-conformation increased in the co-crystals going from 2(P2TE)·(4,6-diBr-res), 2(P2TE)·(4,6-diI-res), 2(P2TE)·(4-Cl-res), to 2(P2TE)·(4,6-diCl-res). IR spectroscopy was performed on each co-crystal to determine

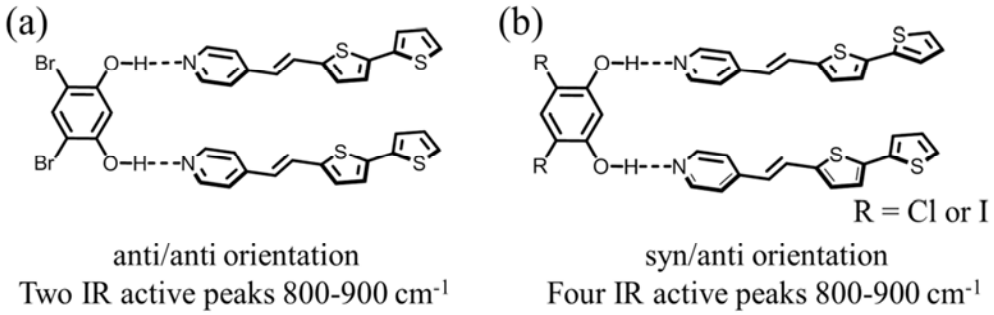

Figure 99: Co-crystals to obtain different conformations a) all *anti*-conformation with two IR active vibrations and b) *anti*- and *syn*-conformation with four IR active vibrations.

how the change in conformation affected the IR spectra of the crystal. It was found that as the bithiophene moiety of P2TE switched from an *anti*-conformation to a *syn*-conformation a greater number of γ-C-H vibrations were IR active. IR spectra of the two conformational polymorphs of DPTT were assigned. IR spectroscopy was also

performed on our previously reported conformational polymorphs of DPTT. The chiral polymorphs display the same increase in γ-C-H peaks compared to the achiral polymorph.

4.8 Experimental Procedure

4.8.1 Synthesis of P2TE

Trans-1-(4-pyridyl)-2-(5-(2,2'-bithienyl))ethylene (P2TE) was synthesized according to the following procedure. A round-bottom flask was charged with 2-bromo-5,2′-bithiophene (1.48 g, 6.0 mmol), distilled 4-vinylpyridine (700 mg, 6.6 mmol), $PdCl_2(PPh_3)_2$ (210 mg, 5 mol %), and anhydrous potassium carbonate (2.5 g, 18 mmol) in 30 mL dimethylformamide. The solution was refluxed overnight. The solution was poured onto ice and the resulting precipitate was filtered. The solid was further purified via column chromatography using silica powder with 2:1 mixture of acetone to hexane as an eluent. Evaporation of solvent yielded an orange solid (421 mg, 26% yield) confirmed to be P2TE by ^{1}H NMR spectroscopy and ^{13}C NMR spectroscopy. ^{1}H NMR data for P2TE ($CDCl_3$, 300 Mhz): δ 8.61-8.64 (2H's, dd, pyridine), δ 7.40- 7.47 (1H, d, ethylene), δ 7.36-7.39 (2H's, dd, pyridine), δ 7.31-7.34 (1H, dd, thiophene), δ 7.27-7.30 (1H, dd, thiophene), δ 7.16-7.18 (1H, d, thiophene), δ 7.09-7.14 (2H, m, thiophene), δ 6.81-6.88 (1H, d, ethylene). ^{13}C NMR data for P2TE ($CDCl_3$): δ 149.5, 140.2, 138.5, 137.0, 129.5, 128.0, 126.2, 125.2, 125.0, 124.3, 120.7.

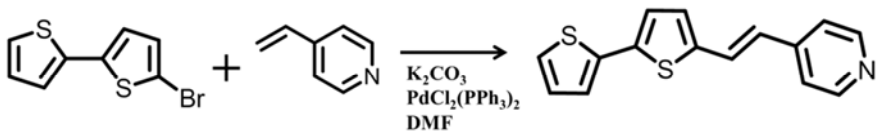

Figure 100: Scheme for synthesis of P2TE.

4.8.2 Crystal growth

Single crystals of P2TE were obtained *via* vapor growth. To obtain single crystals, a copper pipe was fitted over a glass tube to create a temperature gradient. The copper pipe was heated to 150 ^{o}C at one end while using N_2 as the carrier gas (Figure 101). Single crystals of P2TE were collected down in the glass tube from the initial

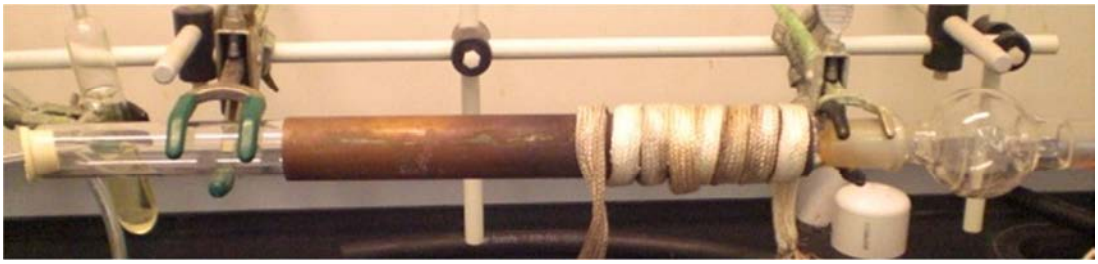

Figure 101: Apparatus for vapor growth

heating site. Co-crystals of P2TE were done by dissolving P2TE and a SCCF (2:1 ratio) in a screw cap vial in a minimal amount of hot acetonitrile. If a solid did not form upon cooling, the cap was loosened and the solvent was allowed to evaporate until a precipitate formed. When 4,6-diBr-res was used as a SCCF two different polymorphs were obtained. The use of a concentrated solution (10 mg/ml) such that crystals formed within minutes of cooling a hot solution to room temperature yielded form α-2(P2TE)·(4,6-diBr-res). When the concentration was lowered (3 mg/ml) such that crystal growth occurred after a few days *via* slow evaporation, the β-2(P2TE)·(4,6-diBr-res) form was obtained. The co-crystals examined were 2(P2TE)·(4,6-Cl-res), α-2(P2TE)·(4,6-diBr-res), β-2(P2TE)·(4,6-diBr-res), 2(P2TE)·(4,6-diI-res) and 2(P2TE)·(4-chlororesorcinol) [2(P2TE)·(4-Cl-res)].

4.8.3 X-ray crystallography

All crystal data were measured on a Nonius Kappa CCD single-crystal X-ray diffractometer at liquid N_2 temperature using MoK_α radiation (λ = 0.7107 Å). The structures were solved and refined by full-matrix lease-squares based on F^2 parameter. All non-hydrogen atoms were refined using the anisotropic model. Hydrogen atoms bonded to carbon atoms were placed in idealized positions based on the hybridization of the belonging carbon atom. Hydrogen atoms bonded to oxygen atoms were placed based on calculations to establish hydrogen bonds to the nearest neighboring hydrogen bond acceptor. Structure solution was accomplished with the aid of WinGX and refinement was conducted using SHELXL-97 locally implemented on a Pentium-based IBM compatible computer.[126] Relevant crystallographic data for all crystal structures described within this chapter are present in the appendix in Tables A-10 through A-11.

4.8.4 Computational studies

The HOMO/LUMO energies levels and IR spectra were calculated using density functional theory (b3lyp cc-pVTZ) with the aid of Spartan 08 implemented on a Pentium-based Dell computer. The basis cc-pVTZ was used to obtain accurate IR spectra.

4.8.5 IR spectroscopy measurements

IR spectra were taken of the solids using KBr pellets on a Nicolet 380 single beam FT-IR spectrophotometer.

4.9 Results and Discussion

4.9.1 Single crystal structures of P2TE

4.9.1.1 Crystal structure P2TE

Single crystals of P2TE were grown *via* vapor growth crystallization using N_2 as a carrier gas to yielded colorless needles. P2TE crystallized in the space group $Pna2_1$ in a

herringbone packing motif with an angle of 55° between molecules in the asymmetric unit (Figure 102). The bithiophene moieties in the P2TE molecules are relatively planar with inter-ring angles of 3.1° and 3.8° respectively. In one of the P2TE molecules, the bithiophene lies in an *anti*-conformation. The second P2TE molecule exhibits disorder in the bithiophene, resulting in a 50:50 mixture of the *anti*- and *syn*-conformation. Therefore, 75% of the bithiophene moieties in the solid lie in the more stable *anti*-

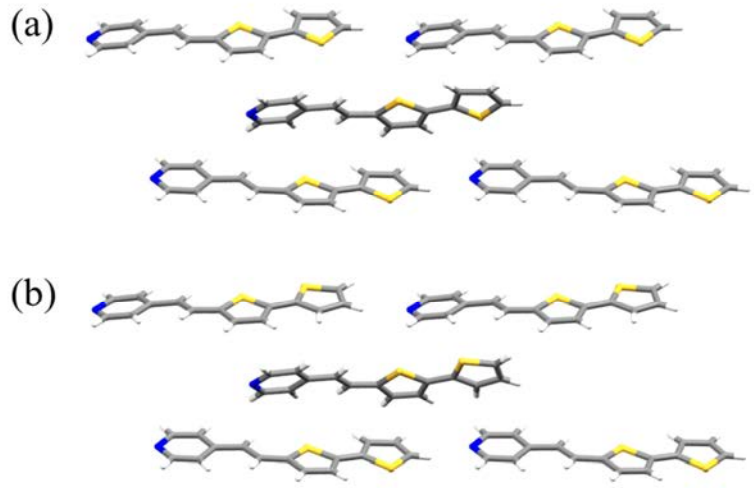

Figure 102: Packing of P2TE as viewed down the *a*-axis with a) both bithiophenes in *anti*-conformation and b) in *anti*-conformation and *syn*-conformation.

conformation, with the remaining in the less stable *syn*-conformation.

4.9.1.2 Co-crystal structures of P2TE

Single crystal structures were collected for five different co-crystals involving P2TE and a SCCF. Specifically, co-crystals were collected with 4-Cl-res, 4,6-diCl-res, 4,6-diBr-res, and 4,6-diI-res acting as the SCCF. Two polymorphs were obtained when 4,6-diBr-res was used as a SCCF. All five co-crystals displayed discrete hydrogen-bonded assemblies. The hydrogen bond distances for the co-crystals are summarized in Table 12.

Table 12: Interatomic distances and percent conformation for co-crystals involving P2TE

SCCF	O···N Bond Distances (Å)	Percent *anti*/*syn*-conformation
4-Cl-res	2.692(4), 2.785(3)	50/50
4,6-diCl-res	2.695(2), 2.765(2)	36/64
α-4,6-diBr-res	2.749(9), 2.727(9)	100/0
β-4,6-diBr-res	2.660(5), 2.683(6) 2.670(5), 2.738(5)	100/0
4,6-diI-res	2.704(9), 2.67(1)	57/43

As with the pure compound, both *anti*- and *syn*-conformations of the bithiophene moiety were observed in the co-crystals. It was discovered that the amount of the bithiophene moiety in the higher energy *syn*-conformation varied depending on which SCCF was used. In the solid 2(P2TE)·(4,6-diCl-res), the *syn*-conformation was present to a greater extent, and 2(P2E)·(4-Cl-res) the *anti*- and *syn*-conformation were present in equal amounts.

4.9.1.2.1 Co-crystal structure of 2(P2TE)·(4-Cl-res)

Co-crystallization of P2TE with 4-Cl-res afforded orange plates with a 2:1 ratio of P2TE to 4-Cl-res in the monoclinic space group $P2_1/c$. The asymmetric unit contains two molecules of P2TE and one molecule of 4-Cl-res. The two P2TE molecules were directed into π-stacked 0-dimensional assemblies *via* O-H···N hydrogen bonds [O···N separation (Å): (O_1···N_1) 2.692(4), (O_2···N_2) 2.785(3)] with 4-Cl-res (Figure103a). Within the assembly, one P2TE molecule displays an *anti*-conformation in the bithiophene moiety while the other P2TE molecule displays the less stable *syn*-conformation. Within the hydrogen bonded assembly, the P2TE molecules are separated by 3.8 Å. The assemblies propagate down the b-axis to form π-stacked columns with a distance of 5.6 Å separating the centroids of nearest P2TE molecules (Figure 103b).

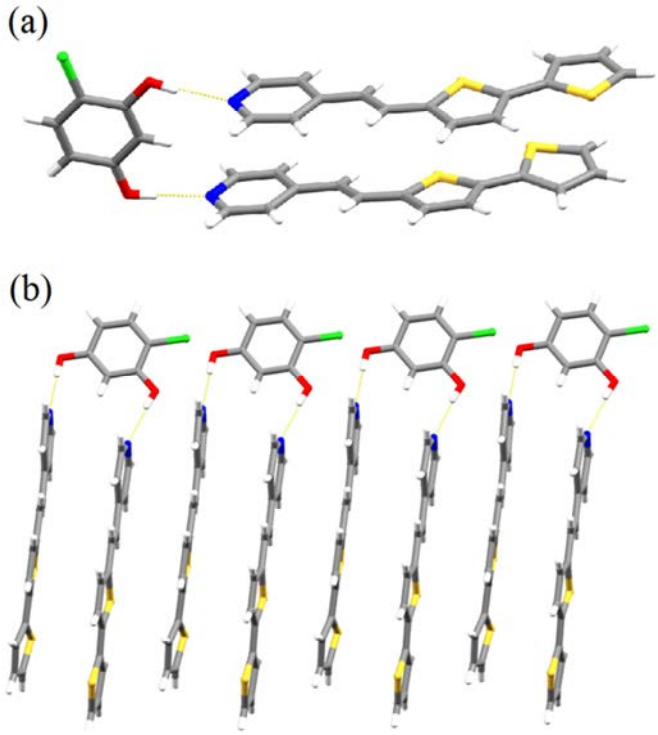

Figure 103: Crystal structure of 2(P2TE)·(4-Cl-res) a) hydrogen-bonded assembly and b) crystal packing viewed down *a*-axis.

4.9.1.2.2 Co-crystal structure of 2(P2TE)·(4,6-diCl-res)

Co-crystallization of P2TE with 4,6-dichlororescorinol afforded red-orange prisms with a 2:1 ratio of P2TE of 4,6-Cl-res in the monoclinic space group $P2_1/c$. There are two P2TE molecules and one 4,6-diCl-res molecule in the asymmetric unit. The two P2TE molecules form a 0-dimensional assembly, with a 4,6-diCl-res molecule through O-H···N hydrogen bonds [O···N separation (Å): (O_1···N_1) 2.695(2), (O_2···N_2) 2.765(2)]. In each assembly one of the P2TE bithiophene moieties lies in the syn-conformation with a rotation angle of 12.3° between thiophenes. The other P2TE molecule contains a disorder in the end thiophene ring such that the bithiophene moiety lies in the *anti*-conformation for 72% of the molecules and the *syn*-conformation the other 28% (Figure

104a and b). The less stable *syn*-conformer makes up 64 % of the bithiophene moieties in the solid. A distance of 3.9 Å separates the centroid of the bithiophene molecules in the π-stacked assembly. The assemblies propagate along the b-axis, with a distance of 5.6 Å separating the nearest P2TE molecules (Figure 103c and d).

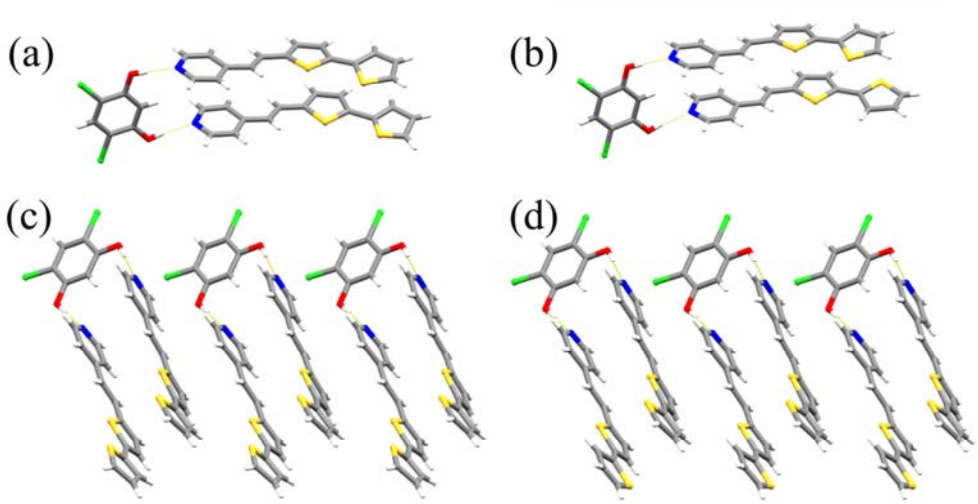

Figure 104: Crystal structure of 2(PT2E)·(4,6-diCl-res) a) assembly with both P2TE in *syn*-conformation, b) assembly of one P2TE *syn* and one P2TE *anti*, c) packing with *syn*-conformation down *a*-axis and d) packing with only *anti*-conformation down *a*-axis.

4.9.1.2.3 Co-crystal structures of polymorphs of 2(P2TE)·(4,6-diBr-res)

Two different polymorphs for 2(P2TE)·(4,6-diBr-res) were obtained depending on the rate of precipitation. Form α-2(P2TE)·(4,6-diBr-res) was obtained by rapid precipitation of P2TE with 4,6-diBr-res from hot acetonitrile. The crystallization afforded yellow blades with a 2:1 ratio of P2TE to 4,6-diBr-res in the monoclinic space group $P2_1/c$. The asymmetric unit contains two P2TE molecules and one molecule of 4,6-diBr-res. 0-dimensional π-stacked assemblies comprised of O-H···N hydrogen

bonds [O···N separation (Å): (O_1···N_1) 2.749(9), (O_2···N_2) 2.727(9)] between 4,6-diBr-res and two P2TE molecules is formed (Figure 105a). The bithiophene moiety in both P2TE molecules in the asymmetric unit lies in the *anti*-conformation. The bithiophene moiety in each P2TE molecule is relatively planar with a dihedral angle less than 3°. The distance between the centroids of the π-stacked bithiophene units in an assembly is 3.8 Å. There is both edge-to-face and face-to-face stacking between assemblies resulting in no extended π-overlap in the solid (Figure 105b).

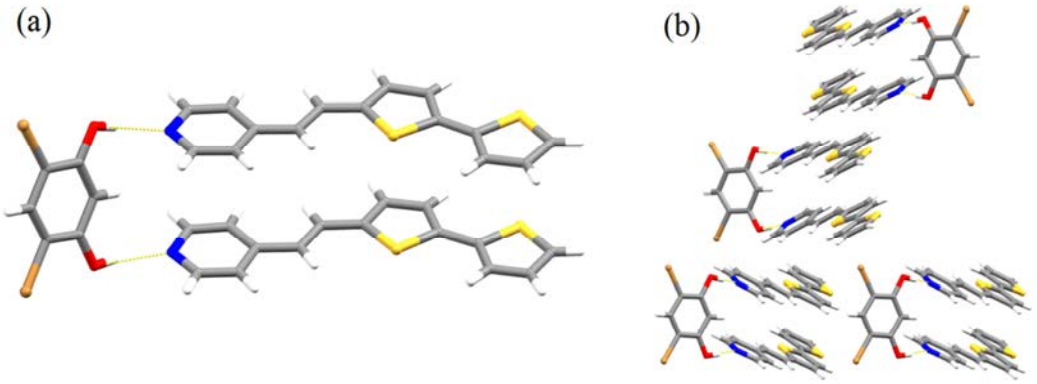

Figure 105: Crystal structure of α-2(P2TE)·(4,6-diBr-res) a) asymmetric unit and b) packing as view down the c-axis.

Polymorph β-2(P2TE)·(4,6-diBr-res) was obtained as red-orange plates *via* slow evaporation of P2TE and 4,6-diBr-res from room temperature acetonitrile over a few days. The co-crystal exhibited a 2:1 ratio of P2TE:4,6-diBr-res, however, the molecules crystallized in the chiral monoclinic space group $P2_1$. The asymmetric unit contains four molecules of P2TE and two molecules of 4,6-diBr-res. Each 4,6-diBr-res forms a 0-dimensional assembly with two P2TE molecules through O-H···N hydrogen bonds [O···N separation (Å): (O_1···N_1) 2.660(5), (O_2···N_2) 2.683(6), (O_3···N_3) 2.670(5), (O_4···N_4) 2.738(5)] yielding two discrete assemblies in the form of β-a and β-b (Figure

106a and b). The P2TE molecules in assembly β-a lie 5.0 Å apart and at an angle of 2.8^{o} with the bithiophenes in an *anti*-conformation. In assembly β-b, the P2TE molecules lie 5.0 Å apart and at an angle of 2.4^{o} with the bithiophenes in an *anti*-conformation. The 5.0 Å distance between P2TE molecules in β-2(P2TE)·(4,6-diBr-res) is greater compared to α-2(P2TE)·(4,6-diBr-res). The chirality arises from β-a and β-b pointing in only one direction in the crystal lattice. The crystal has only edge-to-face packing between assemblies (Figure 106c).

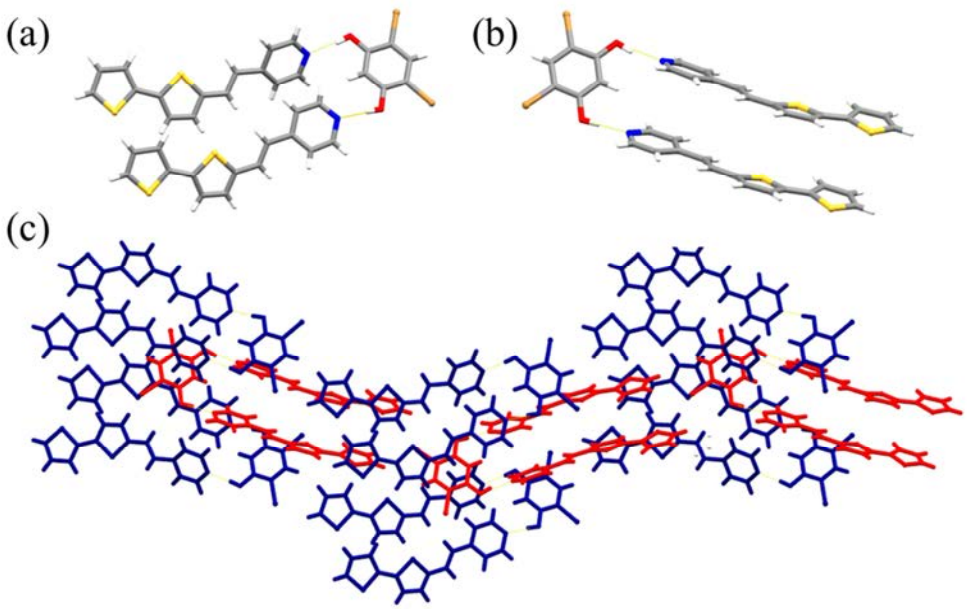

Figure 106: Crystal structure of β-2(P2TE)·(4,6-diBr-res) a) assembly β-a, b) assembly β-b and c) crystal packing down *a*-axis β-a blue and β-b red.

4.9.1.2.4 Co-crystal structure of 2(P2TE)·(4,6-diI-res)

Co-crystallization of P2TE with 4,6-diI-res afforded yellow-orange plates with a 2:1 ratio of P2TE to 4,6-diI-res in the monoclinic space group $P2_1/n$. The asymmetric unit contained one molecule of 4,6-diI-res and two molecules of P2TE. The three molecules in the asymmetric unit form a 0-dimensional assembly through O-H···N

hydrogen bond [O···N separation (Å): (O_1···N_1) 2.704(9), (O_2···N_2) 2.67(1)]. Both P2TE molecules exhibited disorder in the bithiophene moiety in which the terminal thiophene ring is rotated to give either a twisted *anti*- or *syn*-conformation. In one of the P2TE molecules, 51% are present in the twisted *anti*-conformation with a torsion angle of 22° between the two thiophenes. The twisted syn-conformation makes up the last 49% and also displays a torsion angle of 22° in the bithiophene moiety. The second molecule of P2TE displays a disorder of 62% twisted *anti*-conformation and 38% twisted syn-conformation in the bithiophene moiety. A torsion angle of 35° and 23° is observed in the bithiophene moiety for the twisted *anti*-conformation and twisted *syn*-conformation respectively. The disorder creates a situation where the bithiophene moieties within an assembly are in an *anti-anti*-, *anti-syn*-, *syn-anti*-, or *syn-syn*-conformation with the *anti-anti*-conformation being the major orientation (Figure 107a). The assemblies pack to form stacked columns along the c-axis (Figure 107b).

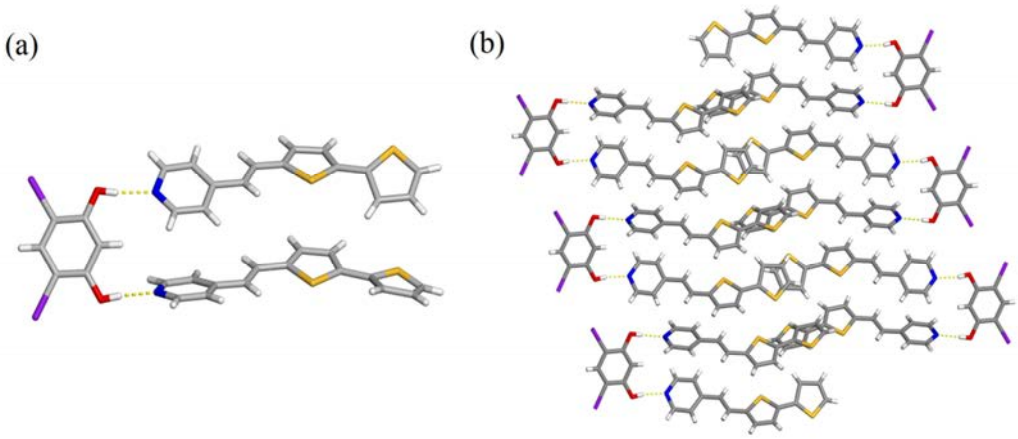

Figure 107: Crystal structure of 2(P2TE)·(4,6-diI-res) a) hydrogen bonded assembly and b) crystal packing view down the *a*-axis.

4.9.2 Calculated electronic properties of P2TE

To further understand effects of change in conformation, DFT calculations were performed on the two conformations of P2TE. The electronic properties and IR spectra of each conformation were, thus, calculated at the B3LYP cc-pVTZ level. The *anti*-conformation was found to be 0.71 kcal/mol lower in energy then the *syn*-conformation. The *syn*-conformation is higher in energy due to increase in steric interactions between H-atoms between thiophene rings. The calculated HOMO and LUMO energy levels for the *anti*-conformation are -5.62 eV and -2.40 eV, respectively. The band gap for the *anti*-conformation is, thus, 3.22 eV. For the *syn*-conformation the HOMO energy level is -5.65 eV and the LUMO energy level is -2.36 eV. The band gap for the *syn*-conformation of P2TE is, thus, 3.29 eV, which is larger than the band gap for the *anti*-conformation. HOMO energy levels for p-type semiconductors are typically between -4.9 and -5.5 eV and for n-type semiconductors the LUMO energy level is typically between -3- -4 eV.[53] The lower HOMO/LUMO energy levels suggest that the *anti*-conformation is the more ideal conformation for charge transport. A UV/Vis spectrum of P2TE has a lambda max at 431 nm which gives a band gap of 2.88 eV (Figure 108). This is lower than either of the calculated band gaps suggesting that the best conformation for charge transport is not seen in the single crystal.

The IR spectrum for each conformation was examined using DFT calculations. Focusing on the region 800 to 900 cm^{-1} where the γ-C-H and ν-C-S stretches appear there are changes in the IR spectra for the *anti*- and *syn*-conformations (Figure 108). The calculated IR spectrum for the *anti*-conformation bithiophene of P2TE exhibits peaks at 810, 826, 841, 844, and 874 cm^{-1}. The peaks at 810, 826, and 841 cm^{-1} are due to γ-C-H vibrations. The peak at 844 cm^{-1} is due to the ν-C-S vibration. The vibration at 874 cm^{-1} is from symmetric stretching of the pyridine moiety (Figure 110a). Changing the bithiophene to the *syn*-conformation in P2TE, the calculated IR spectrum exhibit peaks at 811, 828, 843, 851 and 875 cm^{-1} in the 800 to 900 cm^{-1} region. The γ-C-H vibrations and

symmetric pyridine stretching appear in similar locations at 811, 828, 843, and 875 cm^{-1} respectively (Figure 110b). The ν-C-S stretch, however, demonstrates a shift from the *anti*- to *syn*-conformation. In the *anti*-conformation the ν-C-S stretch is calculated at 844 cm^{-1}, close to the γ-C-H at 841 cm^{-1}, but in the *syn*-conformation the ν-C-S stretch appears at 851 cm^{-1}. The shift suggests that the ν-C-S peak will be isolated in the *syn*-conformation and will be useable to distinguish between the two conformations.

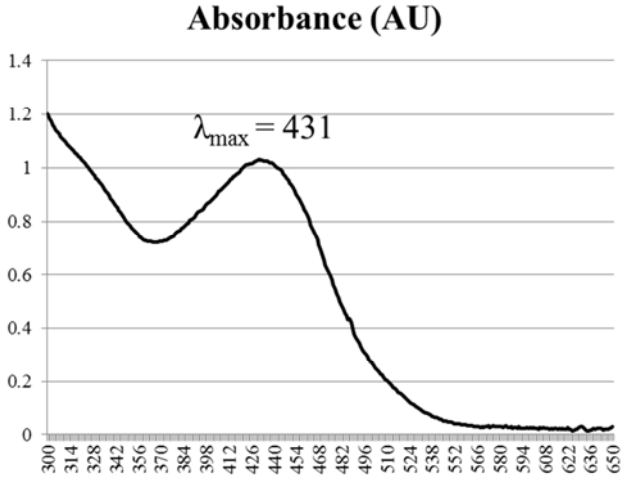

Figure 108: UV/Vis spectrum for P2TE

Table 13: Calculated IR vibrations for P2TE conformations from 800 to 900 cm^{-1}

Conformation	γ-C-H	γ-C-H	γ-C-H	ν-C-S	Pyridine
anti-conformation	810 cm^{-1}	826 cm^{-1}	841 cm^{-1}	844 cm^{-1}	874 cm^{-1}
syn-conformation	811 cm^{-1}	828 cm^{-1}	843 cm^{-1}	851 cm^{-1}	875 cm^{-1}

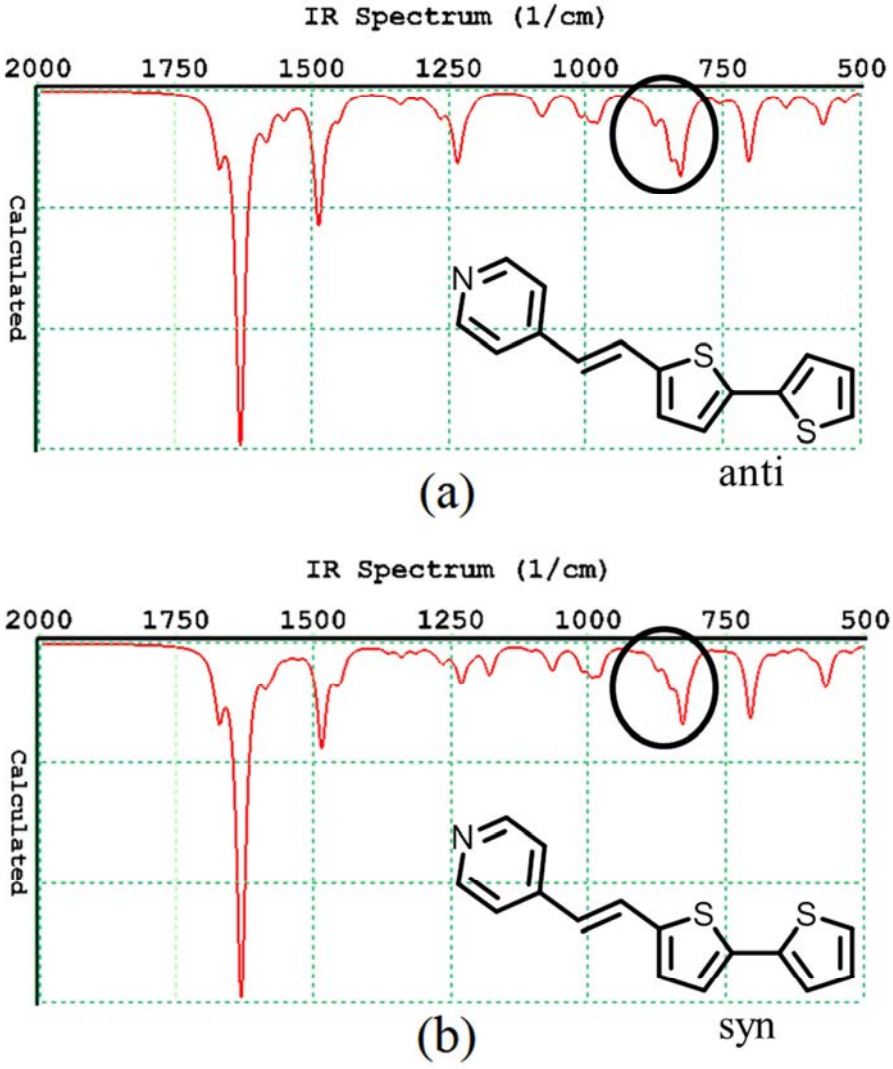

Figure 109: Calculated IR spectrum for P2TE with a) bithiophene in *anti*-conformation, and b) bithiophene in the *syn*-conformation.

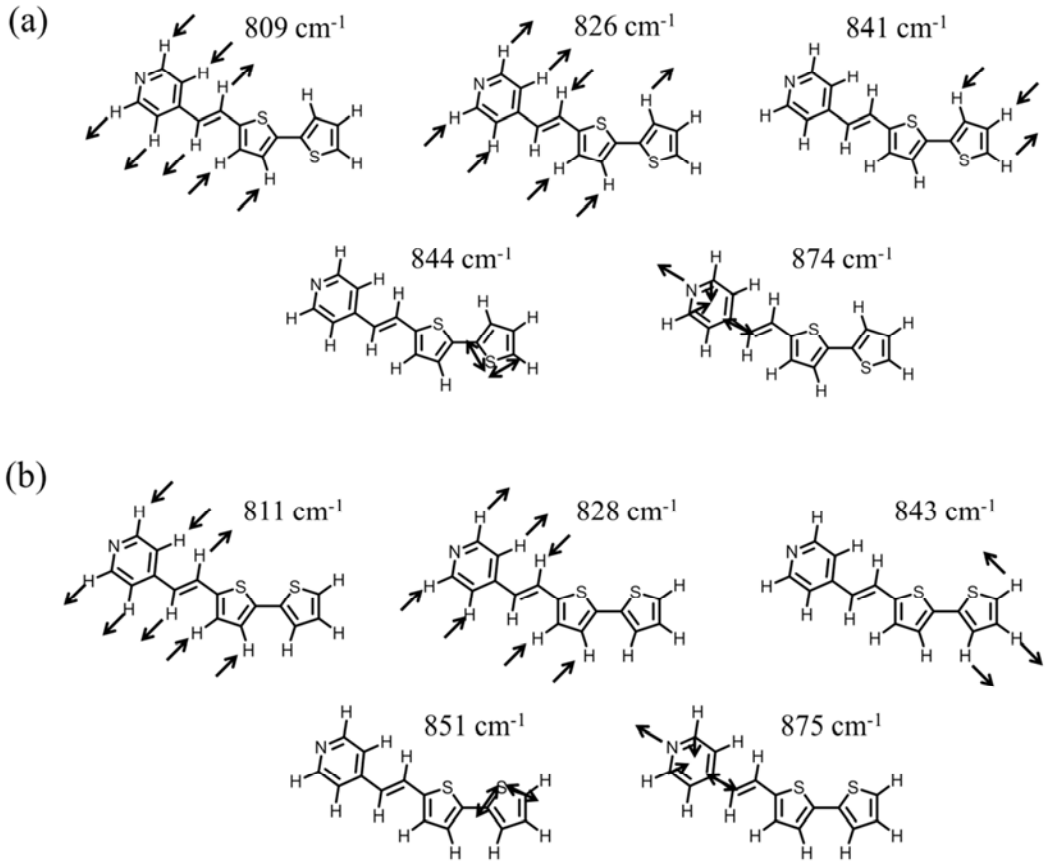

Figure 110: Vibrational stretches between 800 – 900 cm^{-1} for P2TE with bithiophene moiety in a) *anti*-conformation and b) *syn*-conformation.

The region from 1100 to 1300 cm^{-1} in the IR spectra also shows a variation with the change from *anti*- to *syn*-conformation. The *syn*-conformation has four unique peaks at 1105, 1179, 1246, and 1270 cm^{-1} in this region of the IR spectrum. The *anti*-conformation has calculated peaks at 1084 and 1225 cm^{-1} that are unique to the configuration. The unique peaks in the regions from 800-900 cm^{-1} and 1100 to 1300 cm^{-1} suggests that IR spectrometry could be used to identify which conformations are present in a given solid.

4.9.3 IR spectroscopy of pure P2TE and P2TE co-crystals

Since IR spectroscopy can be used to distinguish between the *anti*- and *syn*-conformations of P2TE, IR spectra were obtained for pure P2TE and co-crystals of P2TE. It is expected that since the amount of the *anti*- and *syn*-conformation of the bithiophene moiety varied with different SCCF, the different IR active γ-C-H bends and ν-C-S stretches from 800 to 900 cm^{-1} would likely be observed and could be assigned. Due to the weakness of the vibrations at in the region from 1100 to 1300 cm^{-1} only the region from 800 to 900 cm^{-1} was examined. Stacked spectra of each co-crystal with the pure components with labeled peaks are given in Appendix B (Figure B.1 – B.3).

4.9.3.1 IR spectrum of P2TE

The crystal structure of P2TE confirmed the *anti*- and *syn*-conformations of P2TE to be present in the solid (relative ratio 75:25). The IR spectrum of P2TE displayed peaks at 807, 825, 841, 856, 869, and 889 cm^{-1} between 800 to 900 cm^{-1} (Figure 111). The peak at 889 is assigned to the symmetric vibration of pyridine and the intense peak at 807 cm^{-1} is a γ-C-H of bithiophene.[183,184] The peak at 869 cm^{-1} can be assigned to the

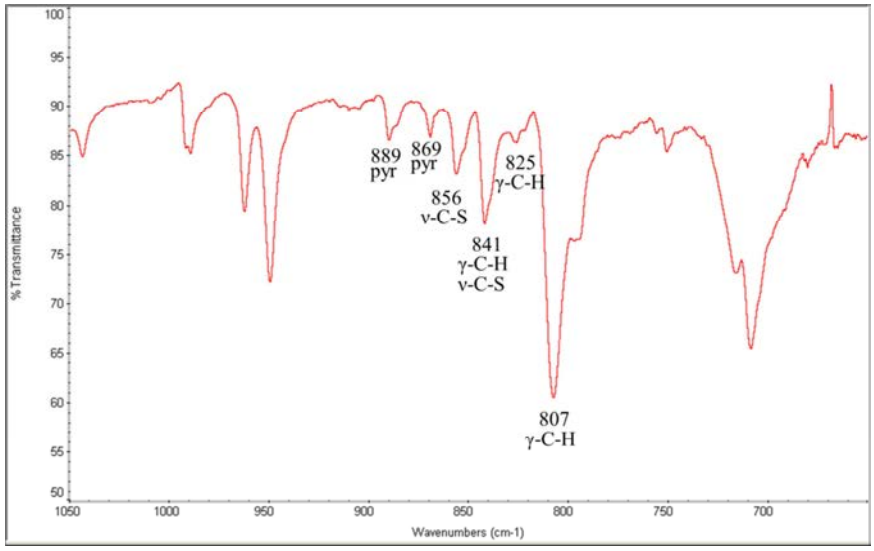

Figure 111: Experimental IR spectrum of P2TE in solid state.

pyridine from the calculated spectrum. The peaks at 825, 841, and 856 cm^{-1} are assigned to γ-C-H and ν-C-S vibrations from the bithiophene moiety in either the *anti- or syn-* conformation.

4.9.3.2 IR spectrum of β-2(P2TE)·(4,6-diBr-res)

The co-crystals of β-2(P2TE)·(4,6-diBr-res) contain only the *anti*-conformation of the bithiophene moiety. Peaks associated with P2TE are, thus, expected to correspond to the bithiophene moiety in an *anti*-conformation. Analyzing the region 800 to 900 cm^{-1} of the IR spectrum of β-2(P2TE)·(4,6-diBr-res) will allow for identification of the peaks that correspond to only the *anti*-conformation (Figure 112). The IR spectrum of 2(P2TE)·(4,6-diBr-res) has a strong peak at 807 cm^{-1} from a γ-C-H bend and weaker peaks at 823, 840 and 864 cm^{-1}. The peak at 864 cm^{-1} is correlates to the pyridine from the calculated spectra. The γ-C-H bends and ν-C-S stretch of bithiophene in the *anti-* conformation corresponds to the peaks at 823 and 840 cm^{-1}.

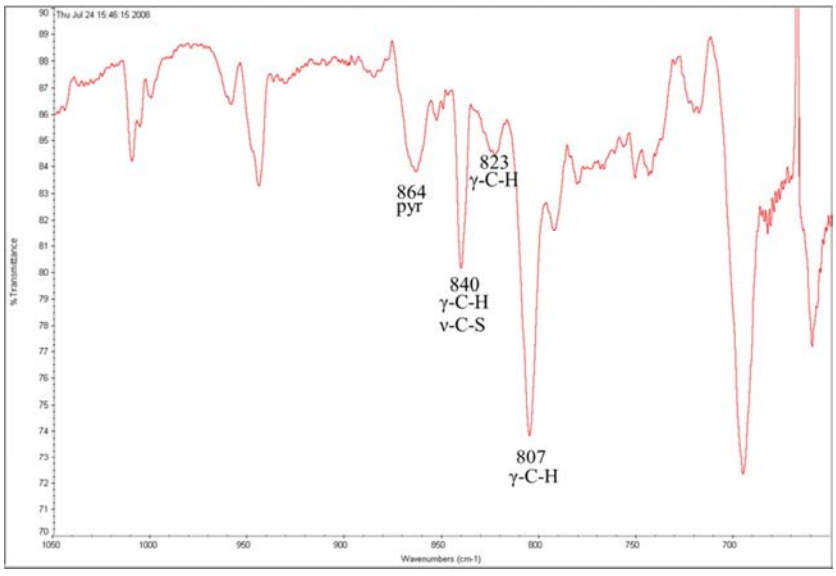

Figure 112: Experimental IR spectrum of 2(P2TE)·(4,6-diBr-res) in solid state.

4.9.3.3 IR spectrum of 2(P2TE)·(4,6-diCl-res)

In single-crystal of 2(P2TE)·(4,6-diCl-res), the *syn*-conformation of P2TE predominates, the solid being the only material wherein the *syn*-conformation is the major conformation. The IR spectrum of 2(P2TE)·(4,6-diCl-res) exhibits peaks at 800, 816, 836, 844, 851, 858, and 875 cm^{-1} (Figure 113). Moreover, the strong γ-C-H stretch that was located at 807 cm^{-1} has blue shifted to 799 cm^{-1}, a change of 8 cm^{-1}. A blue shift is seen in all of the γ-C-H stretches and pyridine compared to the previous spectra. Based off of the IR spectrum of 2(P2TE)·(4,6-diBr-res) the peaks at 816, 836 and 858 cm^{-1} can

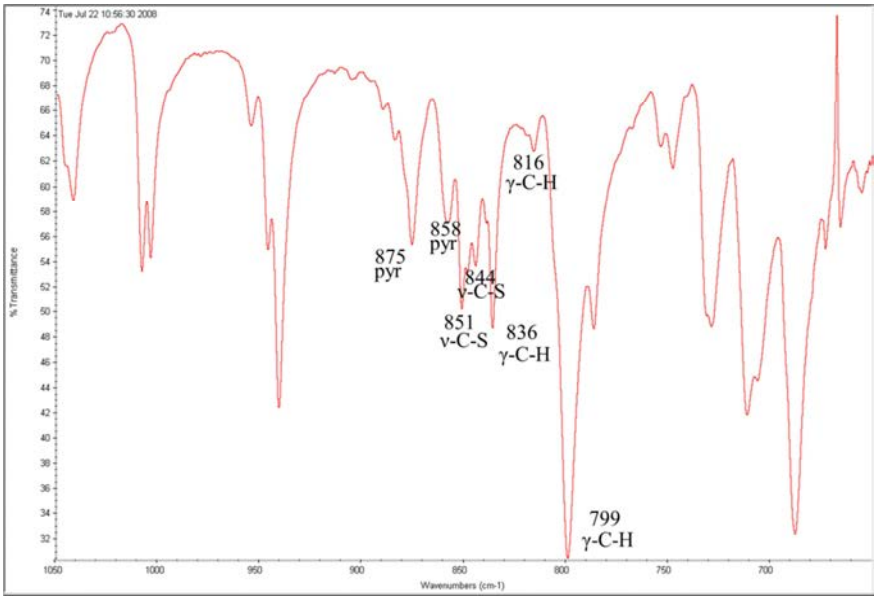

Figure 113: Experimental IR spectrum of 2(P2TE)·(4,6-diCl-res) in solid state.

be assigned as γ-C-H, and pyridine stretches. This leaves the peaks at 844, 851, and 875 to be assigned. The peak at 875 cm^{-1} corresponds to the pyridine vibration in the *syn*-conformation based off of the calculated IR spectrum. The peaks 844 at 851 cm^{-1} can both be assigned as ν-C-S vibrations. The ν-C-S at 844 cm^{-1} is from the *anti*-

conformation based off of the calculated IR, the blue shift of the γ-C-H allows for it to be seen in the spectra. The peak at 851 cm^{-1} can be as the ν-C-S of the *syn*-conformation.

4.9.3.4 IR spectrum of 2(P2TE)·(4,6-diI-res)

Single crystals of 2(P2TE)·(4,6-diI-res) displayed disorder in both of the P2TE molecules in the asymmetric unit. The disorder creates a 57:43 ratio of the *anti*- to *syn*-conformation. However, the bithiophene moiety of P2TE is twisted in both conformations, unlike the bithiophene moiety in the previous solids. The IR spectrum for 2(P2TE)·(4,6-diI-res) exhibits peaks at 807, 843, 851, 863, and 875 cm^{-1} (Figure 114).

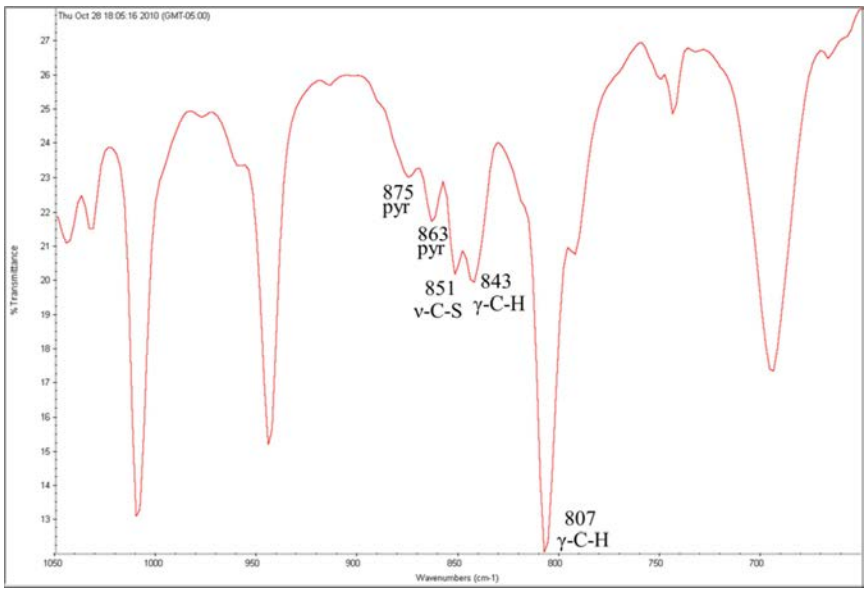

Figure 114: Experimental IR spectrum of 2(P2TE)·(4,6-diI-res) in solid state.

The peak for the strong γ-C-H stretch is at 807 cm^{-1}, where it has been seen in all of the solids in which the *anti*-conformation has been the major conformation. The peaks for the γ-C-H, ν-C-S, and pyridine stretches for the *anti*-conformation are at 843 and 863 cm^{-1}. For the *syn*-conformation peaks appear at 851 and 875 cm^{-1} that can be assigned as the ν-C-H and pyridine vibration.

4.9.4 Changes in IR spectra compared to P2TE conformation

As seen in the IR spectra of the P2TE co-crystals, there are changes in the spectra as the amount of the *syn*-conformation increases in the solid state. From the calculated spectrum the peak at 851 cm^{-1} from a ν-C-S vibration is unique to the *syn*-conformation. Comparing the calculated peaks to the experimental peaks allows for assignment of the peaks so that IR can be used to distinguish between the two conformations. From the IR spectrum of β-2(P2TE)·(4,6-diBr-res), the vibrations from the *anti*-conformation could be assigned. The IR spectrum shows peaks at 807, 840, and 864 cm^{-1}, which correspond to γ-C-H, ν-C-S, and pyridine stretches. Comparison of the peaks in the IR spectrum of 2(P2TE)·(4,6-diBr-res) to the peaks in the IR spectrum of 2(P2TE)·(4,6-diCl-res) allows for assignment of peaks unique to the *syn*-conformation of the bithiophene in P2TE (Figure 115). The peaks at 851 and 875 cm^{-1} are seen only when the *syn*-conformation is present in the crystal. Based off of the calculated IR spectrum the peak at 851 cm^{-1} is due to ν-C-S vibrations and the peak at 875 cm^{-1} can be assigned to the pyridine. Due to the two peaks at 851 and 875 cm^{-1} being unique to the *syn*-conformation IR spectroscopy can, thus, be used to distinguish between the two conformations of P2TE.

The solid of the co-crystal of 2(P2TE)·(4,6-diI-res) has only a slight excess of the *anti*-conformation. However, the bithiophene moieties of P2TE display a twist greater than 20^{o} for both the *anti* and *syn*-conformation. Examining the IR spectrum of 2(P2TE)·(4,6-diI-res), the location of the peaks are at 807, 843, 852, 863 and 875 cm^{-1}. Despite the twist in the thiophene backbone the peaks are in the same location as previously seen. The strong γ-C-H stretch is at 807 cm^{-1} and the γ-C-H, ν-C-S, and pyridine stretches are at 843 and 863 cm^{-1} for the *anti*-conformation. The peaks at 851 and 875 cm^{-1} can be assigned as ν-C-S stretch and the pyridine for the *syn*-conformation. This suggests that the peaks at 851 cm^{-1} and 875 can be used to detect the presence of the *syn*-conformation in P2TE even when there is a twist in the bithiophene.

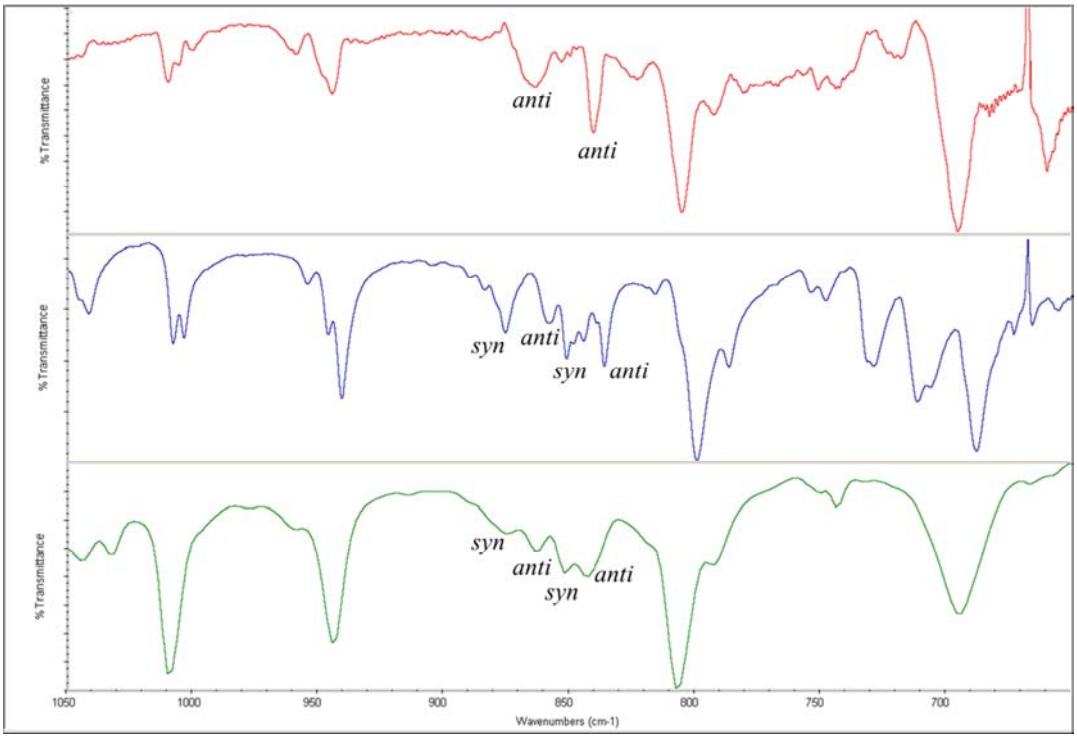

Figure 115: Overlay of IR spectrum of 2(P2TE)·(4,6-diBr-res) (red), 2(P2TE)·(4,6-diCl-res) (blue), 2(P2TE)·(4,6-diI-res) (green).

4.9.5 Infrared spectroscopy of polymorphs of DPTT

The two polymorphs of DPTT provide an opportunity to determine how the introduction of a *syn*-conformation into a terthiophene affects the γ-C-H stretches (Figure 116). The achiral polymorph that contains only the *anti*-conformation displays two peaks at 793 and 805 cm^{-1} for γ-C-H vibration. The same region in the IR spectra for the chiral polymorph of DPTT that is in the *syn*-*anti*-conformation displays three peaks at 790, 796, and 804 cm^{-1}. These results are similar to the calculated IR spectrum for the *anti*- and *syn*-conformation of bithiophene. There are more peaks in the γ-C-H region for the chiral polymorph with the anti-syn conformation then for the achiral polymorph which only has the anti-conformation. There were peaks located around 1440 cm^{-1}, which was the area

used to distinguish the two polymorphs of Aza4T. However, there was not enough variation in the region to distinguish between the two polymorphs of DPTT.[178]

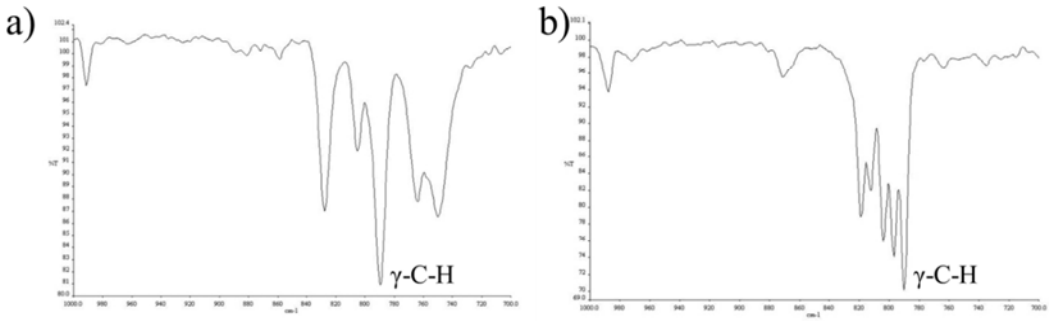

Figure 116: IR spectrum of DPTT a) achiral polymorph and b) chiral polymorph.

4.10 Conclusions

It has been shown that co-crystallization can be used to stabilize a higher energy conformation of P2TE. Specifically, by switching the SCCF the amount of the higher energy *syn*-conformation of the bithiophene moiety of P2TE present in the solid could be changed. The ability to control the conformation is important because different conformations create different interactions between P2TE molecules in the solid and can alter the mobility of the material. The change in conformation of the P2TE can be monitored by IR spectroscopy. It was found that the γ-C-H, ν-C-S, and pyridine stretches between 800 to 900 cm^{-1} could be used to suggest which conformations are present in the solid-state. The peak at 851 cm^{-1} resulting from the ν-C-S is unique to the IR spectrum for P2TE when the bithiophene moiety is in the *syn*-conformation. A change in position of the pyridine stretch is also noticeable. The ability to detect the changes in conformation is important for polymorph screening for device manufacturing.

CHAPTER 5: CONCLUSION AND FUTURE WORK

We demonstrated the ability to perform a [2+2] photodimerization reaction on thiophenes in the solid state with yields in excess of 90 % through the use of co-crystallization. The reactive alignment was achieved through the formation of a 0-D hydrogen-bonded assembly between either α-PTE or β-PTE and a resorcinol based SCCF. Despite the formation of a 0-D assembly between a resorcinol based SCCF and NPE, a reactive alignment was not obtained. Changing the SCCF from a resorcinol based system to a carboxylic acid allowed for isolation of an alternate photoproduct for β-PTE. Calculations showed that the photoproduct of either α-PTE or β-PTE had an increased band gap compared to α-PTE or β-PTE. The ability to change the solid state properties of an organic semiconductor can allow for patterning of a thin film after deposition through exposure to UV light.

To show the utility of [2+2] photodimerization the photopatterning of a thin film was performed. Specifically, we showed the ability to create a thin film by spin coating a 1:1 mixture of BPE to HP onto a glass substrate and patterning the film through selective UV light exposure. Patterning was done by reacting selected regions with UV light *via* a photomask. It was found that the exposed regions became less soluble in a 2:1 pentane to diethyl ether solution compared to the unexposed regions. By development of a patterned thin film in the 2:1 solution, we were able to selectively remove areas of the thin film and obtain features as small as 5μm.

We demonstrated that the addition of a second component can have a positive impact on an organic semiconductor. To probe the impact of the second component of a co-crystal, the mobility of DTE was compared to mobility of 2(DTE)·2(4,6-diCl-res), 2(DTE)·2(4,6-diI-res), and 2(DTE)·2(4,6-ditBu-res). Each co-crystal consists of 0-dimensional hydrogen bond assemblies in which two SCCFs direct two DTE molecules into π-stacked conformation. It was found that the mobility of each two-component

crystal exceeded the mobility of DTE alone. The co-crystal 2(DTE)·2(4,6-diCl-res) had the highest mobility of 0.12 $cm^2V^{-1}s^{-1}$, which was 178 times higher than pure DTE. In the co-crystal 2(DTE)·2(4,6-diCl-res), the assemblies are further organized by halogen-oxygen interactions to create π-stacked columns. The improvement in mobility is attributed to the improved π-stacking in each crystal.

We discovered that the conformation of the bithiophene moiety of P2TE can be altered by co-crystallizing it with different SCCFs. Specifically, it was found that the amount of the higher energy *syn*-conformation obtained in the solid could be changed by switching SCCFs. This change in orientation was then detected with IR spectroscopy by monitoring the γ-C-H, ν-C-S, and pyridine stretches from the bithiophene. It was found that the *syn*-conformation demonstrates a unique peak at 851 cm^{-1} that corresponds to the ν-C-S stretch. The unique peak allows for identifying what conformation is present in the solid state. Monitoring the changes in γ-C-H and ν-C-S peaks has the potential to be used as a screening method for conformational polymorphs.

This work is expected to help progress towards a method to modify stable, high mobility organic semiconductors after deposition through means of UV irradiation. Ideally a high mobility co-crystalline thin film that is UV reacted will be created. The co-crystal former will serve no only to align the organic semiconductor into π-stacked assemblies but also aid in the formation of the thin film. UV light could then be shined to turn off specific regions of the thin film to minimize cross talk and create preferred pathways for charge transport in an OTFT. IR spectroscopy could then be used to insure that the quality of the bulk sample. An easily patterned high mobility transistor would allow for the commercial development of flexible electronics.

REFERENCES

(1) Desiraju, G. R. *Angew. Chem. Int. Ed.* **1995**, *34*, 2311.

(2) Desiraju, G. R. *Angew. Chem. Int. Ed* **2007**, *46*, 8342.

(3) Reddy, D. S.; Craig, D. C.; Desiraju, G. R. *J. Am. Chem. Soc.* **1996**, *118*, 4090.

(4) Simard, M.; Su, D.; Wuest, J. D. *J. Am. Chem. Soc.* **1991**, *113*, 4696.

(5) El-Kaderi, H. M.; Hunt, J. R.; Mendoza-Cortes, J. L.; Cote, A. P.; Taylor, R. E.; O'Keeffe, M.; Yaghi, O. M. *Science* **2007**, *316*, 268.

(6) Pintre, I. C.; Serrano, J. L.; Ros, M. B.; Martinez-Perdiguero, J.; Alonso, I.; Ortega, J.; Folcia, C. L.; Etxebarria, J.; Alicante, R.; Villacampa, B. *J. Mater. Chem.* **2010**, *20*, 2965.

(7) Trivedi, D. R.; Fujiki, Y.; Fujita, N.; Shinkai, S.; Sada, K. *Chem. Asian J.* **2009**, *4*, 254.

(8) Glaser, R. *Acc Chem Res* **2007**, *40*, 9.

(9) Aakeroy, C. B. *Acta Crystallogr., Sect. B: Struct. Commun.* **1997**, *53*, 569.

(10) Dunitz, J. D.; Bernstein, J. *Acc. Chem. Res.* **1995**, *28*, 193.

(11) Vishweshwar, P.; McMahon, J. A.; Oliveira, M.; Peterson, M. L.; Zaworotko, M. J. *J. Am. Chem. Soc.* **2005**, *127*, 16802.

(12) Braga, D.; Maini, L.; Polito, M.; Scaccianoce, L.; Cojazzi, G.; Grepioni, F. *Coord. Chem. Rev.* **2001**, *216*, 225.

(13) Dunitz, J. D. *Crystengcomm* **2003**, *5*, 506.

(14) Desiraju, G. R. *Crystengcomm* **2003**, *5*, 466.

(15) Aakeroy, C. B.; Salmon, D. J. *Crystengcomm* **2005**, *7*, 439.

(16) Almarsson, O.; Zaworotko, M. J. *Chem. Commun.* **2004**, 1889.

(17) Vishweshwar, P.; McMahon, J. A.; Bis, J. A.; Zaworotko, M. J. *J. Pharm. Sci.* **2006**, *95*, 499.

(18) Zyss, J.; Ledoux-Rak, I.; Weiss, H. C.; Blaser, D.; Boese, R.; Thallapally, P. K.; Thalladi, V. R.; Desiraju, G. R. *Chem. Mater.* **2003**, *15*, 3063.

(19) Sokolov, A. N.; Friscic, T.; MacGillivray, L. R. *J. Am. Chem. Soc.* **2006**, *128*, 2806.

(20) Chiarella, R. A.; Davey, R. J.; Peterson, M. L. *Cryst. Growth Des.* **2007**, *7*, 1223.

(21) Varughese, S.; Pedireddi, V. R. *Tetrahedron Letters* **2005**, *46*, 2411.

(22) Friscic, T.; Jones, W. *Cryst. Growth Des.* **2009**, *9*, 1621.

(23) Drury, C. J.; Mutsaers, C. M. J.; Hart, C. M.; Matters, M.; de Leeuw, D. M. *Appl. Phys. Lett.* **1998**, *73*, 108.

(24) Reese, C.; Roberts, M.; Ling, M.-m.; Bao, Z. *Mater. Today* **2004**, *7*, 20.

(25) Katz, H. E.; Bao, Z.; Gilat, S. L. *Acc. Chem. Res.* **2001**, *34*, 359.

(26) Jurchescu, O. D.; Baas, J.; Palstra, T. T. M. *Appl. Phys. Lett.* **2004**, *84*, 3061.

(27) Bredas, J. L.; Calbert, J. P.; da Silva, D. A.; Cornil, J. *Proc. Nat. Acad. Sci. U.S.A.* **2002**, *99*, 5804.

(28) Hutchison, G. R.; Ratner, M. A.; Marks, T. J. *J. Am. Chem. Soc.* **2005**, *127*, 16866.

(29) Yang, X. D.; Wang, L. J.; Wang, C. L.; Long, W.; Shuai, Z. G. *Chem. Mater.* **2008**, *20*, 3205.

(30) Deng, W. Q.; Goddard, W. A. *J. Phys. Chem. B* **2004**, *108*, 8614.

(31) Wang, L. J.; Nan, G. J.; Yang, X. D.; Peng, Q.; Li, Q. K.; Shuai, Z. G. *Chem. Soc. Rev.* **2010**, *39*, 423.

(32) Nagamatsu, S.; Kaneto, K.; Azumi, R.; Matsumoto, M.; Yoshida, Y.; Yase, K. *J. Phys. Chem. B* **2005**, *109*, 9374.

(33) Ling, M. M.; Bao, Z. N. *Chem. Mater.* **2004**, *16*, 4824.

(34) Dimitrakopoulos, C. D.; Malenfant, P. R. L. *Adv. Mater.* **2002**, *14*, 99.

(35) Kraft, A. *ChemPhysChem* **2001**, *2*, 163.

(36) Horowitz, G.; Hajlaoui, M. E.; Hajlaoui, R. *J. Appl. Phys.* **2000**, *87*, 4456.

(37) Sirringhaus, H.; Kawase, T.; Friend, R. H.; Shimoda, T.; Inbasekaran, M.; Wu, W.; Woo, E. P. *Science* **2000**, *290*, 2123.

(38) Weidkamp, K. P.; Afzali, A.; Tromp, R. M.; Hamers, R. J. *J. Am. Chem. Soc.* **2004**, *126*, 12740.

(39) Chen, J. L.; Leblanc, V.; Kang, S. H.; Benning, P. J.; Schut, D.; Baldo, M. A.; Schmidt, M. A.; Bulovic, V. *Adv. Funct. Mater.* **2007**, *17*, 2722.

(40) Briseno, A. L.; Aizenberg, J.; Han, Y. J.; Penkala, R. A.; Moon, H.; Lovinger, A. J.; Kloc, C.; Bao, Z. A. *J. Am. Chem. Soc.* **2005**, *127*, 12164.

(41) Briseno, A. L.; Mannsfeld, S. C. B.; Ling, M. M.; Liu, S. H.; Tseng, R. J.; Reese, C.; Roberts, M. E.; Yang, Y.; Wudl, F.; Bao, Z. N. *Nature* **2006**, *444*, 913.

(42) Holmes, D.; Kumaraswamy, S.; Matzger, A. J.; Vollhardt, K. P. C. *Chem. Eur. J.* **1999**, *5*, 3399.

(43) Kelley, T. W.; Boardman, L. D.; Dunbar, T. D.; Muyres, D. V.; Pellerite, M. J.; Smith, T. Y. P. *J. Phys. Chem. B* **2003**, *107*, 5877.

(44) Goidmann, C.; Haas, S.; Krellner, C.; Pernstich, K. P.; Gundlach, D. J.; Batlogg, B. *J. Appl. Phys.* **2004**, *96*, 2080.

(45) Mondal, R.; Tönshoff, C.; Khon, D.; Neckers, D. C.; Bettinger, H. F. *J. Am. Chem. Soc.* **2009**, *131*, 14281.

(46) Azumi, R.; Goto, M.; Honda, K.; Matsumoto, M. *Bull. Chem. Soc. Jpn.* **2003**, *76*, 1561.

(47) Fichou, D.; Bachet, B.; Demanze, F.; Billy, I.; Horowitz, G.; Garnier, F. *Adv. Mater.* **1996**, *8*, 500.

(48) Siegrist, T.; Kloc, C.; Laudise, R. A.; Katz, H. E.; Haddon, R. C. *Adv. Mater.* **1998**, *10*, 379.

(49) Horowitz, G.; Bachet, B.; Yassar, A.; Lang, P.; Demanze, F.; Fave, J.-L.; Garnier, F. *Chem. Mater.* **2002**, *7*, 1337.

(50) Murphy, A. R.; Frechet, J. M. J. *Chem. Rev.* **2007**, *107*, 1066.

(51) Moon, H.; Zeis, R.; Borkent, E. J.; Besnard, C.; Lovinger, A. J.; Siegrist, T.; Kloc, C.; Bao, Z. N. *J. Am. Chem. Soc.* **2004**, *126*, 15322.

(52) Reese, C.; Bao, Z. N. *J. Mater. Chem.* **2006**, *16*, 329.

(53) Dong, H. L.; Wang, C. L.; Hu, W. P. *Chem. Commun.* **2010**, *46*, 5211.

(54) Anthony, J. E.; Brooks, J. S.; Eaton, D. L.; Parkin, S. R. *J. Am. Chem. Soc.* **2001**, *123*, 9482.

(55) Anthony, J. E. *Chem. Rev.* **2006**, *106*, 5028.

(56) Anthony, J. E.; Eaton, D. L.; Parkin, S. R. *Org. Lett.* **2002**, *4*, 15.

(57) Park, S. K.; Jackson, T. N.; Anthony, J. E.; Mourey, D. A. *Appl. Phys. Lett.* **2007**, *91*.

(58) Payne, M. M.; Parkin, S. R.; Anthony, J. E. *J. Am. Chem. Soc.* **2005**, *127*, 8028.

(59) Podzorov, V.; Menard, E.; Borissov, A.; Kiryukhin, V.; Rogers, J. A.; Gershenson, M. E. *Phys. Rev. Lett.* **2004**, *93*.

(60) Cornil, J.; Calbert, J. P.; Bredas, J. L. *J. Am. Chem. Soc.* **2001**, *123*, 1250.

(61) Miao, Q.; Chi, X. L.; Xiao, S. X.; Zeis, R.; Lefenfeld, M.; Siegrist, T.; Steigerwald, M. L.; Nuckolls, C. *J. Am. Chem. Soc.* **2006**, *128*, 1340.

(62) Garnier, F.; Deloffre, F.; Horowitz, G.; Hajlaoui, R. *Synth. Met.* **1993**, *57*, 4747.

(63) Garnier, F.; Horowitz, G.; Fichou, D.; Yassar, A. *Synth. Met.* **1996**, *81*, 163.

(64) Moret, M.; Campione, M.; Borghesi, A.; Miozzo, L.; Sassella, A.; Trabattoni, S.; Lotz, B.; Thierry, A. *J. Mater. Chem.* **2005**, *15*, 2444.

(65) Halik, M.; Klauk, H.; Zschieschang, U.; Schmid, G.; Ponomarenko, S.; Kirchmeyer, S.; Weber, W. *Adv. Mater.* **2003**, *15*, 917.

(66) Mushrush, M.; Facchetti, A.; Lefenfeld, M.; Katz, H. E.; Marks, T. J. *J. Am. Chem. Soc.* **2003**, *125*, 9414.

(67) Maunoury, J. C.; Howse, J. R.; Turner, M. L. *Adv. Mater.* **2007**, *19*, 805.

(68) Sung, A.; Ling, M. M.; Tang, M. L.; Bao, Z. A.; Locklin, J. *Chem. Mater.* **2007**, *19*, 2342.

(69) Kobayashi, K.; Masu, H.; Shuto, A.; Yamaguchi, K. *Chem. Mater.* **2005**, *17*, 6666.

(70) Kobayashi, K.; Shimaoka, R.; Kawahata, M.; Yamanaka, M.; Yamaguchi, K. *Org. Lett.* **2006**, *8*, 2385.

(71) Patrick, C. R.; Prosser, G. S. *Nature* **1960**, *187*, 1021.

(72) Feast, W. J.; Lovenich, P. W.; Puschmann, H.; Taliani, C. *Chem. Commun.* **2001**, 505.

(73) Coates, G. W.; Dunn, A. R.; Henling, L. M.; Dougherty, D. A.; Grubbs, R. H. *Angew. Chem. Int. Ed.* **1997**, *36*, 248.

(74) Facchetti, A.; Yoon, M. H.; Stern, C. L.; Katz, H. E.; Marks, T. J. *Angew. Chem. Int. Ed* **2003**, *42*, 3900.

(75) Swartz, C. R.; Parkin, S. R.; Bullock, J. E.; Anthony, J. E.; Mayer, A. C.; Malliaras, G. G. *Org. Lett.* **2005**, *7*, 3163.

(76) Chen, Z. H.; Muller, P.; Swager, T. M. *Org. Lett.* **2006**, *8*, 273.

(77) Cho, D. M.; Parkin, S. R.; Watson, M. D. *Org. Lett.* **2005**, *7*, 1067.

(78) Chang, Y. C.; Chen, Y. D.; Chen, C. H.; Wen, Y. S.; Lin, J. T.; Chen, H. Y.; Kuo, M. Y.; Chao, I. *J. Org. Chem.* **2008**, *73*, 4608.

(79) Barbarella, G.; Zambianchi, M.; Bongini, A.; Antolini, L. *J. Org. Chem.* **1996**, *61*, 4708.

(80) Schoonbeek, F. S.; van Esch, J. H.; Wegewijs, B.; Rep, D. B. A.; de Haas, M. P.; Klapwijk, T. M.; Kellogg, R. M.; Feringa, B. L. *Angew. Chem. Int. Ed* **1999**, *38*, 1393.

(81) Rep, D. B. A.; Roelfsema, R.; van Esch, J. H.; Schoonbeek, F. S.; Kellogg, R. M.; Feringa, B. L.; Palstra, T. T. M.; Klapwijk, T. M. *Adv. Mater.* **2000**, *12*, 563.

(82) Gesquiere, A.; De Feyter, S.; De Schryver, F. C.; Schoonbeek, F.; van Esch, J.; Kellogg, R. M.; Feringa, B. L. *Nano Lett.* **2001**, *1*, 201.

(83) Garnier, F.; Hajlaoui, R.; Yassar, A.; Srivastava, P. *Science* **1994**, *265*, 1684.

(84) Pisula, W.; Menon, A.; Stepputat, M.; Lieberwirth, I.; Kolb, U.; Tracz, A.; Sirringhaus, H.; Pakula, T.; Mullen, K. *Adv. Mater.* **2005**, *17*, 684.

(85) Hines, D. R.; Mezhenny, S.; Breban, M.; Williams, E. D.; Ballarotto, V. W.; Esen, G.; Southard, A.; Fuhrer, M. S. *Appl. Phys. Lett.* **2005**, *86*.

(86) Wang, J. Z.; Zheng, Z. H.; Li, H. W.; Huck, W. T. S.; Sirringhaus, H. *Nature Materials* **2004**, *3*, 171.

(87) Afzali, A.; Dimitrakopoulos, C. D.; Breen, T. L. *J. Am. Chem. Soc.* **2002**, *124*, 8812.

(88) Buchholz, V.; Enkelmann, V. *Molecular Crystals and Liquid Crystals* **2001**, *356*, 315.

(89) Rogers, J. A.; Bao, Z.; Katz, H. E.; Dodabalapur, A. *Thin-film Transistors* **2003**, 377.

(90) Bao, Z. N.; Feng, Y.; Dodabalapur, A.; Raju, V. R.; Lovinger, A. J. *Chem. Mater.* **1997**, *9*, 1299.

(91) Duffy, D. C.; Jackman, R. J.; Vaeth, K. M.; Jensen, K. F.; Whitesides, G. M. *Adv. Mater.* **1999**, *11*, 546.

(92) Menard, E.; Meitl, M. A.; Sun, Y. G.; Park, J. U.; Shir, D. J. L.; Nam, Y. S.; Jeon, S.; Rogers, J. A. *Chem. Rev.* **2007**, *107*, 1117.

(93) Baude, P. F.; Ender, D. A.; Haase, M. A.; Kelley, T. W.; Muyres, D. V.; Theiss, S. D. *Appl. Phys. Lett.* **2003**, *82*, 3964.

(94) Hebner, T. R.; Wu, C. C.; Marcy, D.; Lu, M. H.; Sturm, J. C. *Appl. Phys. Lett.* **1998**, *72*, 519.

(95) Choi, J. H.; Kim, D.; Yoo, P. J.; Lee, H. H. *Adv. Mater.* **2005**, *17*, 166.

(96) Mannsfeld, S. C. B.; Sharei, A.; Liu, S. H.; Roberts, M. E.; McCulloch, I.; Heeney, M.; Bao, Z. A. *Adv. Mater.* **2008**, *20*, 4044.

(97) Abdou, M. S. A.; Diazguijada, G. A.; Arroyo, M. I.; Holdcroft, S. *Chem. Mater.* **1991**, *3*, 1003.

(98) Afzali, A.; Dimitrakopoulos, C. D.; Graham, T. O. *Adv. Mater.* **2003**, *15*, 2066.

(99) Schmidt, G. M. J. *Journal of the Chemical Society* **1964**, 2014.

(100) Cohen, M. D.; Schmidt, G. M. J.; Sonntag, F. I. *Journal of the Chemical Society* **1964**, 2000.

(101) Kaupp, G. *Current Opinion in Solid State & Materials Science* **2002**, *6*, 131.

(102) Irie, M.; Kobatake, S.; Horichi, M. *Science* **2001**, *291*, 1769.

(103) Kohler, W.; Novak, K.; Enkelmann, V. *Journal of Chemical Physics* **1994**, *101*, 10474.

(104) Papaefstathiou, G. S.; Zhong, Z. M.; Geng, L.; MacGillivray, L. R. *J. Am. Chem. Soc.* **2004**, *126*, 9158.

(105) Zaumseil, J.; Sirringhaus, H. *Chem. Rev.* **2007**, *107*, 1296.

(106) Li, Z. F.; Du, J.; Tang, Q.; Wang, F.; Xu, J. B.; Yu, J. C.; Miao, Q. A. *Adv. Mater.* **2010**, *22*, 3242.

(107) Kawatsuki, N.; Ando, R.; Ishida, R.; Kondo, M.; Minami, Y. *Macromolecular Chemistry and Physics* **2010**, *211*, 1741.

(108) Kido, J.; Kohda, M.; Okuyama, K.; Nagai, K. *Appl. Phys. Lett.* **1992**, *61*, 761.

(109) Hoffmann, C. L.; Rabolt, J. F. *Macromolecules* **1996**, *29*, 2543.

(110) He, L.; Liu, J. F.; Wu, Z. X.; Wang, D. D.; Liang, S. X.; Zhang, X. W.; Jiao, B.; Wang, D. W.; Hou, X. *Thin Solid Films* **2010**, *518*, 3886.

(111) Wu, S.; Shi, F.; Zhang, Q. J.; Bubeck, C. *Macromolecules* **2009**, *42*, 4110.

(112) Friscic, T.; Drab, D. M.; MacGillivray, L. R. *Org. Lett.* **2004**, *6*, 4647.

(113) Wynberg, H.; Groen, M. B.; Kellogg, R. M. *J. Org. Chem.* **1970**, *35*, 2828.

(114) Costanzo, L. L.; Giuffrida, S.; Pistara, S.; Scarlata, G.; Torre, M. *Journal of Photochemistry* **1982**, *18*, 317.

(115) Amato, M. E.; Musumarra, G.; Scarlata, G.; Lamba, D.; Spagna, R. *Journal of Crystallographic and Spectroscopic Research* **1989**, *19*, 791.

(116) Dauria, M.; Racioppi, R. *Tetrahedron* **1997**, *53*, 17307.

(117) Clement, S.; Meyer, F.; De Winter, J.; Coulembier, O.; Velde, C.; Zeller, M.; Gerbaux, P.; Balandier, J. Y.; Sergeyev, S.; Lazzaroni, R.; Geerts, Y.; Dubois, P. *J. Org. Chem.* **2010**, *75*, 1561.

(118) Ito, Y.; Borecka, B.; Olovsson, G.; Trotter, J.; Scheffer, J. R. *Tetrahedron Letters* **1995**, *36*, 6087.

(119) Ito, Y.; Hosomi, H.; Ohba, S. *Tetrahedron* **2000**, *56*, 6833.

(120) D'Auria, M.; Emanuele, L.; Mauriello, G.; Racioppi, R. *J. Photochem. Photobiol. A-Chem.* **2000**, *134*, 147.

(121) Houlton, P. R.; Kemp, W. *Tetrahedron Letters* **1968**, 1045.

(122) Meinwald, J.; Young, J. W.; Walsh, E. J.; Courtin, A. *Pure and Applied Chemistry* **1970**, *24*, 12.

(123) Takeuchi, M.; Tuihiji, T.; Nishimura, J. *J. Org. Chem.* **1993**, *58*, 7388.

(124) Nishimura, J.; Takeuchi, M.; Takahashi, H.; Ueda, E.; Matsuda, Y.; Oku, A. *Bull. Chem. Soc. Jpn.* **1989**, *62*, 3161.

(125) Hart, H.; Suzuki, M. *Tetrahedron Letters* **1975**, 3451.

(126) Sheldrick, G. M. University of Göttingen, Germany, 1997.

(127) Voth, A. R.; Khuu, P.; Oishi, K.; Ho, P. S. *Nature Chemistry* **2009**, *1*, 74.

(128) Kaupp, G. *Crystengcomm* **2003**, 117.

(129) Sarma, J. A. R. P.; Bernstein, J. *Molecular Engineering* **1992**, *2*, 103.

(130) Pedireddi, V. R.; Sarma, J.; Desiraju, G. R. *Journal of the Chemical Society-Perkin Transactions 2* **1992**, 311.

(131) Kaupp, G. *International Journal of Photoenergy* **2001**, *3*, 55.

(132) Vedernikov, A. I.; Kuz'Mina, L. G.; Sazonov, S. K.; Lobova, N. A.; Loginov, P. S.; Churakov, A. V.; Strelenko, Y. A.; Howard, J. A. K.; Alfimov, M. V.; Gromov, S. P. *Russian Chemical Bulletin* **2007**, *56*, 1860.

(133) Kole, G. K.; Tan, G. K.; Vittal, J. J. *Org. Lett.* **2010**, *12*, 128.

(134) Gromov, S. P.; Ushakov, E. N.; Fedorova, O. A.; Baskin, II; Buevich, A. V.; Andryukhina, E. N.; Alfimov, M. V.; Johnels, D.; Edlund, U. G.; Whitesell, J. K.; Fox, M. A. *J. Org. Chem.* **2003**, *68*, 6115.

(135) Yamashita, Y. *Sci. Technol. Adv. Mater.* **2009**, *10*.

(136) Gsanger, M.; Oh, J. H.; Konemann, M.; Hoffken, H. W.; Krause, A. M.; Bao, Z. N.; Wurthner, F. *Angew. Chem. Int. Ed* **2010**, *49*, 740.

(137) Takimiya, K.; Yamamoto, T.; Ebata, H.; Izawa, T. *Sci. Technol. Adv. Mater.* **2007**, *8*, 273.

(138) Yang, X. D.; Li, Q. K.; Shuai, Z. G. *Nanotechnology* **2007**, *18*.

(139) Treier, M.; Nguyen, M. T.; Richardson, N. V.; Pignedoli, C.; Passerone, D.; Fasel, R. *Nano Lett.* **2009**, *9*, 126.

(140) Mattheus, C. C.; Baas, J.; Meetsma, A.; de Boer, J. L.; Kloc, C.; Siegrist, T.; Palstra, T. T. M. *Acta Crystallographica Section E-Structure Reports Online* **2002**, *58*, O1229.

(141) Nicolas, Y.; Blanchard, P.; Roncali, J.; Allain, M.; Mercier, N.; Deman, A. L.; Tardy, J. *Org. Lett.* **2005**, *7*, 3513.

(142) Merlo, J. A.; Newman, C. R.; Gerlach, C. P.; Kelley, T. W.; Muyres, D. V.; Fritz, S. E.; Toney, M. F.; Frisbie, C. D. *J. Am. Chem. Soc.* **2005**, *127*, 3997.

(143) Meng, H.; Sun, F. P.; Goldfinger, M. B.; Jaycox, G. D.; Li, Z. G.; Marshall, W. J.; Blackman, G. S. *J. Am. Chem. Soc.* **2005**, *127*, 2406.

(144) Videlot-Ackermann, C.; Ackermann, J.; Brisset, H.; Kawamura, K.; Yoshimoto, N.; Raynal, P.; El Kassmi, A.; Fages, F. *J. Am. Chem. Soc.* **2005**, *127*, 16346.

(145) Um, M. C.; Jang, J.; Kang, J.; Hong, J. P.; Yoon, D. Y.; Lee, S. H.; Kim, J. J.; Hong, J. I. *J. Mater. Chem.* **2008**, *18*, 2234.

(146) Klauk, H.; Zschieschang, U.; Weitz, R. T.; Meng, H.; Sun, F.; Nunes, G.; Keys, D. E.; Fincher, C. R.; Xiang, Z. *Adv. Mater.* **2007**, *19*, 3882.

(147) Meng, H.; Sun, F.; Goldfinger, M. B.; Gao, F.; Londono, D. J.; Marshal, W. J.; Blackman, G. S.; Dobbs, K. D.; Keys, D. E. *J. Am. Chem. Soc.* **2006**, *128*, 9304.

(148) Drolet, N.; Morin, J.-F.; Leclerc, N.; Wakim, S.; Tao, Y.; Leclerc, M. *Adv. Funct. Mater.* **2005**, *15*, 1671.

(149) Roncali, J. *Acc. Chem. Res.* **2000**, *33*, 147.

(150) Roncali, J. *Chem. Rev.* **1997**, *97*, 173.

(151) Xiao, S. X.; Tang, J. Y.; Beetz, T.; Guo, X. F.; Tremblay, N.; Siegrist, T.; Zhu, Y. M.; Steigerwald, M.; Nuckolls, C. *J. Am. Chem. Soc.* **2006**, *128*, 10700.

(152) Ji, H. X.; Hu, J. S.; Wan, L. J.; Tang, Q. X.; Hu, W. P. *J. Mater. Chem.* **2008**, *18*, 328.

(153) Tang, Q. X.; Li, H. X.; Song, Y. B.; Xu, W.; Hu, W. P.; Jiang, L.; Liu, Y. Q.; Wang, X. K.; Zhu, D. B. *Adv. Mater.* **2006**, *18*, 3010.

(154) Briseno, A. L.; Mannsfeld, S. C. B.; Jenekhe, S. A.; Bao, Z.; Xia, Y. *Mater. Today* **2008**, *11*, 38.

(155) Tang, Q. X.; Jiang, L.; Tong, Y. H.; Li, H. X.; Liu, Y. L.; Wang, Z. H.; Hu, W. P.; Liu, Y. Q.; Zhu, D. B. *Adv. Mater.* **2008**, *20*, 2947.

(156) Jiang, L.; Fu, Y. Y.; Li, H. X.; Hu, W. P. *J. Am. Chem. Soc.* **2008**, *130*, 3937.

(157) Zhou, Y.; Liu, W. J.; Ma, Y. G.; Wang, H. L.; Qi, L. M.; Cao, Y.; Wang, J.; Pei, J. *J. Am. Chem. Soc.* **2007**, *129*, 12386.

(158) Kim, D. H.; Lee, D. Y.; Lee, H. S.; Lee, W. H.; Kim, Y. H.; Han, J. I.; Cho, K. *Adv. Mater.* **2007**, *19*, 678.

(159) Reid, O. G.; Munechika, K.; Ginger, D. S. *Nano Lett.* **2008**, *8*, 1602.

(160) Sassella, A.; Borghesi, A.; Destri, S.; Porzio, W.; Tubino, R. *Synth. Met.* **1999**, *101*, 530.

(161) Botta, C.; Destri, S.; Porzio, W.; Sassella, A.; Borghesi, A.; Tubino, R. *Optical Materials* **1999**, *12*, 301.

(162) Bernstein, J. *Polymorphism in Molecular Crystals*; Oxford University Press, 2002.

(163) Siegrist, T.; Besnard, C.; Haas, S.; Schiltz, M.; Pattison, P.; Chernyshov, D.; Batlogg, B.; Kloc, C. *Adv. Mater.* **2007**, *19*, 2079.

(164) Fichou, D. *J. Mater. Chem.* **2000**, *10*, 571.

(165) Jiang, H.; Yang, X.; Cui, Z.; Liu, Y.; Li, H.; Hu, W.; Liu, Y.; Zhu, D. *Appl. Phys. Lett.* **2007**, *91*.

(166) Kitamura, M. *Crystengcomm* **2009**, *11*, 949.

(167) Threlfall, T. L. *Analyst* **1995**, *120*, 2435.

(168) Bernstein, J.; Hagler, A. T. *J. Am. Chem. Soc.* **1978**, *100*, 673.

(169) Nangia, A. *Acc. Chem. Res.* **2008**, *41*, 595.

(170) Pan, H.; Liu, P.; Li, Y.; Wu, Y.; Ong, B. S.; Zhu, S.; Xu, G. *Adv. Mater.* **2007**, *19*, 3240.

(171) Barbarella, G.; Zambianchi, M.; DiToro, R.; Colonna, M.; Antolini, L.; Bongini, A. *Adv. Mater.* **1996**, *8*, 327.

(172) Barbarella, G.; Zambianchi, M.; Marimon, M. D. I.; Antolini, L.; Bongini, A. *Adv. Mater.* **1997**, *9*, 484.

(173) Widany, J.; Daminelli, G.; Di Carlo, A.; Lugli, P.; Jungnickel, G.; Elstner, M.; Frauenheim, T. *Physical Review B* **2001**, *63*.

(174) Barbarella, G.; Zambianchi, M.; Antolini, L.; Ostoja, P.; Maccagnani, P.; Bongini, A.; Marseglia, E. A.; Tedesco, E.; Gigli, G.; Cingolani, R. *J. Am. Chem. Soc.* **1999**, *121*, 8920.

(175) Muguruma, H.; Saito, T. K.; Hotta, S. *Thin Solid Films* **2003**, *445*, 26.

(176) Muguruma, H.; Hotta, S. *J. Phys. Chem. B* **2006**, *110*, 23075.

(177) Muguruma, H.; Kobiro, K.; Hotta, S. *Chem. Mater.* **1998**, *10*, 1459.

(178) Sokolov, A. N.; Sumrak, J. C.; MacGillivray, L. R. *Chem. Commun.* **2010**, *46*, 82.

(179) Chaloner, P. A.; Gunatunga, S. R.; Hitchcock, P. B. *Acta Crystallographica Section C-Crystal Structure Communications* **1994**, *50*, 1941.

(180) Cui, C. X.; Kertesz, M. *Physical Review B* **1989**, *40*, 9661.

(181) McClure, S. A.; Buriak, J. M.; DiLabio, G. A. *Journal of Physical Chemistry C* **2010**, *114*, 10952.

(182) Millefiori, S.; Alparone, A.; Millefiori, A. *Journal of Heterocyclic Chemistry* **2000**, *37*, 847.

(183) Jacinto, F. S. F.; Siqueira, L. J. A.; Alves, W. A. *Journal of Raman Spectroscopy* **2009**, *40*, 1585.

(184) Ehrendorfer, C.; Karpfen, A. *Journal of Physical Chemistry* **1995**, *99*, 5341.

APPENDIX A: TABLES OF CRYSTALLOGRAPHIC DATA

Table A1: Crystallographic parameters for α-PTE, 2(α-PTE)·(4,6-diCl-res), and 2(α-PTE)·(4,6-diBr-res)

Compound	α-PTE	2(α-PTE)·(4,6-diCl-res)	2(α-PTE)·(46-diBr-res)
T / K	293(2)	293(2)	293(2)
λ / Å	0.71073	0.71073	0.71073
Crystal system	monoclinic	monoclinic	monoclinic
Space group	P c	P 2_1/c	P 2_1
a / Å	6.1274(7)	13.8337(15)	16.5092(18)
b / Å	7.6048(9)	5.8050(7)	18.6806(19)
c / Å	10.3172(11)	32.889(4)	18.3928(19)
α / ^{o}	90.00	90	90.00
β / ^{o}	93.323(5)	101.686(5)	105.247(5)
γ / ^{o}	90.00	90.00	90.00
V / Å^3	479.949	2586.39	5472.71
Z	2	4	12
ρ_{calc} / g cm^{-3}	1.296	1.421	1.657
μ / mm^{-1}	0.285	0.442	4.565
2θ range / ^{o}	2.68-25.00	1.50-25.00	1.28-25.00
collected reflections	2413	11782	28269
unique reflections	1613	4246	17079
Parameters	212	388	1298
S	0.920	0.891	0.981
R	0.0403	0.0850	0.0746
wR^2	0.1197	0.1835	0.1934
$\rho_{min, max}$ / e Å^{-3}	0.155, -0.141	0.479, -0.398	0.730, -0.589

Table A2: Crystallographic parameters for 2(α-PTE)·(4,6-diI-res) and 2(α-PTE)·(5-acetyl-res)

Compound	2(α-PTE)·(4,6-diI-res)	2(α-PTE)·(5-acetyl-res)
T / K	298(2)	293(2)
λ / Å	0.71073	0.71073
Crystal system	monoclinic	monoclinic
Space group	P 2_1	P 2_1/c
a / Å	9.2775(10)	15.5425(17)
b / Å	34.412(4)	13.2128(14)
c / Å	9.8978(11)	8.2328(9)
α / °	90.00	90.00
β / °	116.864(5)	95.853(5)
γ / °	90.00	90.00
V / Å^3	2818.9(5)	1681.87
Z	5	3
ρ_{calc} / g cm^{-3}	1.735	1.560
μ / mm^{-1}	2.407	0.279
2θ range / °	2.53-22.50	2.03-25.00
collected reflections	9321	9162
unique reflections	6438	2884
parameters	778	193
S	1.041	1.0820
R	0.0266	0.0902
wR^2	0.0573	0.2453
$\rho_{min, max}$ / e Å^{-3}	0.304, -0.373	0.278, -0.214

Table A3: Crystallographic parameters for β-PTE, 2(β-PTE)·(4,6-diCl-res), and 2(β-PTE)· (4,6-diI-res)

Compound	β-PTE	2(β-PTE)·(4,6-diCl-res)	2(β-PTE)·(4,6-diI-res)
T / K	293(2)	293(2)	293(2)
λ / Å	0.71073	0.71073	0.71073
Crystal system	Monoclinic	Triclinic	monoclinic
Space group	P 2_1	P -1	P 2_1
a / Å	6.344(10)	9.3977(10)	9.2833(10)
b / Å	7.555(13)	10.2804(11)	34.548(4)
c / Å	9.736(16)	13.7923(15)	9.8979(11)
α / ^{o}	90.00	84.148(5)	90.00
β / ^{o}	94.45(10)	89.570(5)	117.717(5)
γ / ^{o}	90.00	76.851(5)	90.00
V / Å^3	465.229	1290.64	2810.2
Z	2	2	4
ρ_{calc} / g cm^{-3}	1.337	1.424	1.741
μ / mm^{-1}	0.294	0.443	2.415
2θ range / ^{o}	2.10-24.71	1.48-25.00	1.18-25.00
collected reflections	1537	8092	14141
unique reflections	1098	4545	8807
parameters	146	325	536
S	1.205	0.753	0.911
R	0.1454	0.0542	0.0705
wR^2	0.3669	0.1573	0.1612
$\rho_{min, max}$ / e Å^{-3}	0.364, -0.244	0.317, -0.339	0.503, -0.667

Table A4: Crystallographic parameters for 2(NPE)·(4,6-diCl-res)·CH_3CN, 2(NPE)·(4,6-diBr-res), and 2(NPE)·(4,6-diI-res)

Compound	2(NPE)·(4,6-dCl-res)·CH_3CN	2(NPE)·(4,6-diBr-res)	2(NPE)·(4,6-diI-res)
T / K	293(2)	293(2)	293(2)
λ / Å	0.71073	0.71073	0.71073
Crystal system	Monoclinic	orthorhombic	orthorhombic
Space group	P 2_1	P c a 2_1	P c a 2_1
a / Å	13.9837(15)	36.164(4)	36.620(9)
b / Å	7.7338(9)	5.8828(7)	5.8690(13)
c / Å	16.6630(18)	15.4096(16)	15.686(4)
α / °	90.00	90.00	90.00
β / °	97.236(5)	90.00	90.00
γ / °	90.00	90.00	90.00
V / Å^3	1787.7	3278.32	3371.28
Z	2	4	4
ρ_{calc} / g cm^{-3}	1.262	1.480	1.530
μ / mm^{-1}	0.222	2.511	1.898
2θ range / °	2.03-25.00	1.32-24.99	1.30-25.00
collected reflections	9151	20845	9976
unique reflections	5732	5715	4737
parameters	444	416	416
S	0.999	1.005	0.839
R	0.0574	0.0425	0.0742
wR^2	0.1232	0.0870	0.1879
$\rho_{min, max}$ / e Å^{-3}	0.235, -0.162	0.419, -0.546	0.477, -0.616

Table A5: Crystallographic parameters for (β-PTE)·(benzoic acid) and 2(β-PTE)·(succinic acid)

Compound	(β-PTE)·(benzoic acid)	2(β-PTE)·(succinic acid)
T / K	293(2)	293(2)
λ / Å	0.71073	0.71073
Crystal system	Monoclinic	monoclinic
Space group	P 2_1/n	P 2_1/c
a / Å	7.1608(8)	9.28267(10)
b / Å	20.287(3)	19.692(2)
c / Å	11.0658(12)	13.6649(15)
α / °	90.00	90.00
β / °	107.004(5)	108.704(5)
γ / °	90.00	90.00
V / Å^3	1537.27	2365.93
Z	4	6
ρ_{calc} / g cm^{-3}	1.337	1.377
μ / mm^{-1}	0.217	0.261
2θ range / °	3.03-25.00	1.88-25.00
collected reflections	9082	15457
unique reflections	2675	4160
parameters	199	307
S	1.033	1.601
R	0.0351	0.1280
wR^2	0.0880	0.3878
$\rho_{min, max}$ / e Å^{-3}	0.213, -0.259	1.502, -0.878

Table A6: Crystallographic parameters for (d2tcb)·(4,6-diI-res) and (d3tcb)·(4,6-diI-res)

Compound	(α-2tcb)·(4,6-diI-res)	(β-3tcb)·(4,6-diI-res)
T / K	293(2)	293(2)
λ / Å	0.71073	0.71073
Crystal system	monoclinic	Monoclinic
Space group	P 2_1/c	P 2_1/c
a / Å	17.7900(19)	17.699(8)
b / Å	9.9059(11)	10.176(4)
c / Å	16.8926(18)	16.360(9)
α / ^{o}	90.00	90.00
β / ^{o}	109.293(5)	108.02(5)
γ / ^{o}	90.00	90.00
V / Å^3	2809.74	2801.99
Z	4	4
ρ_{calc} / g cm^{-3}	1.741	1.803
μ / mm^{-1}	2.415	2.425
2θ range / ^{o}	1.21-25.00	2.86-25.00
collected reflections	17999	7574
unique reflections	4936	4049
parameters	372	325
S	1.079	1.018
R	0.1075	0.0860
wR^2	0.3265	0.2118
$\rho_{min, max}$ / e Å^{-3}	3.548, -1.011	0.873, -0.686

Table A7: Crystallographic parameters for DTE, and 2(DTE)·2(4,6-diCl-res)

Compound	DTE (single crystal)	2(DTE)·2(4,6-diCl-res)
T / K	293(2)	200(2)
λ / Å	0.71073	0.71073
Crystal system	monoclinic	Monoclinic
Space group	C 2/c	P 2_1/n
a / Å	18.56(2)	8.7110(10)
b / Å	5.705(5)	29.680(3)
c / Å	7.507(7)	9.3937(10)
α / ^{o}	90.00	90.00
β / ^{o}	96.62(4)	103.100(5)
γ / ^{o}	90.00	90.00
V / Å^3	789.577	2365.47
Z	2	4
ρ_{calc} / g cm^{-3}	1.457	1.475
μ / mm^{-1}	0.340	0.479
2θ range / ^{o}	4.56-25.00	1.37-25.00
collected reflections	1804	14471
unique reflections	662	4148
parameters	68	309
S	1.183	1.041
R	0.1389	0.0508
wR^2	0.3530	0.0864
$\rho_{min, max}$ / e Å^{-3}	0.400, -0.355	0.281, -0.244

Table A8: Crystallographic parameters for 2(DTE)·2(4,6-diBr-res) and 2(DTE)·2(4,6-diI-res)

Compound	2(DTE)·2(4,6-diBr-res)	2(DTE)·2(4,6-diI-res)
T / K	190(2)	190(2)
λ / Å	0.71073	0.71073
Crystal system	Monoclinic	monoclinic
Space group	P 2_1/n	P 2_1/n
a / Å	8.8516(10)	9.1475(10)
b / Å	29.752(3)	29.759(3)
c / Å	9.4637(10)	9.6474(11)
α / °	90.00	90.00
β / °	104.461(5)	106.621(5)
γ / °	90.00	90.00
V / Å^3	2413.33	2516.49
Z	4	4
ρ_{calc} / g cm^{-3}	1.691	1.870
μ / mm^{-1}	3.560	2.692
2θ range / °	2.82-25.00	3.01-24.99
collected reflections	13336	15613
unique reflections	4253	4413
parameters	307	307
S	0.988	1.067
R	0.0230	0.0252
wR^2	0.0541	0.0508
$\rho_{min, max}$ / e Å^{-3}	0.389, -0.240	0.611, -0.406

Table A9: Crystallographic parameters for 2(DTE)·2(4,6-ditbu-res) and 2(DTE)·2(5-methyl-res)

Compound	2(DTE)·2(4,6-ditbu-res)	2(DTE)·2(5-methyl-res)
T / K	190(2)	190(2)
λ / Å	0.71073	0.71073
Crystal system	Triclinic	Triclinic
Space group	P -1	P -1
a / Å	9.8117(11)	8.4904(9)
b / Å	11.5897(13)	9.3378(10)
c / Å	15.2313(16)	15.0279(16)
α / ^{o}	68.675(5)	78.665(5)
β / ^{o}	88.837(5)	87.623(5)
γ / ^{o}	69.858(5)	75.612(5)
V / Å^3	1503.82	1131.52
Z	2	2
ρ_{calc} / g cm^{-3}	1.256	1.381
μ / mm^{-1}	0.210	0.264
2θ range / ^{o}	2.54-25.00	2.48-25.00
collected reflections	10256	7374
unique reflections	5280	3945
parameters	361	299
S	1.062	1.031
R	0.0357	0.0827
wR^2	0.0917	0.2517
$\rho_{min, max}$ / e Å^{-3}	0.199, -0.226	0.820, -0.446

Table A10: Crystallographic parameters for P2TE, 2(P2TE)·(4-Cl-res), and 2(P2TE)·(4,6-diCl-res)

Compound	P2TE	2(P2TE)·2(4-Cl-res)	2(P2TE)·2(4,6-diCl-res)
T / K	210(2)	209(2)	209(2)
λ / Å	0.71073	0.71073	0.71073
Crystal system	Orthorhombic	Monoclinic	Monoclinic
Space group	P n a 2_1	P 2_1	P 2_1
a / Å	21.765(3)	13.4886(14)	13.5713(15)
b / Å	15.8031(17)	7.7244(9)	7.9124(9)
c / Å	7.4894(8)	30.872(4)	31.032(4)
α / ^{o}	90.00	90.00	90.00
β / ^{o}	90.00	95.172(5)	90.229(5)
γ / ^{o}	90.00	90.00	90.000
V / Å^3	2576.01	3203.5	3332.24
Z	8	6	6
ρ_{calc} / g cm^{-3}	1.389	1.294	1.431
μ / mm^{-1}	0.392	0.389	0.482
2θ range / ^{o}	1.87-25.00	1.32-25.00	2.89-25.00
collected reflections	16319	17584	20140
unique reflections	4531	5645	5859
parameters	365	406	458
S	0.871	1.048	1.087
R	0.0599	0.0680	0.0345
wR^2	0.1046	0.2096	0.879
$\rho_{min, max}$ / e Å^{-3}	0.215, -0.215	2.533, -0.570	0.266, -0.288

Table A11: Crystallographic parameters for 2(P2TE)·(4,6-diBr-res)-α, 2(P2TE)·(4,6-diBr-res)-β, and 2(P2TE)·(4,6-diI-res)

Compound	2(P2TE)·(4,6-diBr-res)	2(P2TE)·2(4,6-diBr-res)	2(P2TE)·2(4,6-diI-res)
T / K	190(2)	190(2)	209(2)
λ / Å	0.71073	0.71073	0.71073
Crystal system	monoclinic	Monoclinic	monoclinic
Space group	P 2_1/c	P 2_1	P 2_1/n
a / Å	18.2103(19)	9.6187(11)	9.0444(10)
b / Å	5.8191(7)	41.043(5)	42.291(5)
c / Å	31.917(4)	9.7517(11)	9.3753(10)
α / °	90.00	90.00	90.00
β / °	100.868(5)	118.414(5)	103.718(5)
γ / °	90.00	90.00	90.00
V / Å^3	3321.5	3386.01	3483.73
Z	4	8	6
ρ_{calc} / g cm^{-3}	1.609	1.582	1.811
μ / mm^{-1}	2.729	2.677	2.904
2θ range / °	1.14-25.00	2.46-25.00	2.66-25.00
collected reflections	16494	18227	22229
unique reflections	5802	11176	6110
parameters	415	849	509
S	0.991	1.023	1.205
R	0.0729	0.0377	0.0539
wR^2	0.1203	0.0787	0.1207
$\rho_{min, max}$ / e Å^{-3}	1.360, -0.699	0.354, -0.271	0.717, -0.801

APPENDIX B: IR OVERLAYS

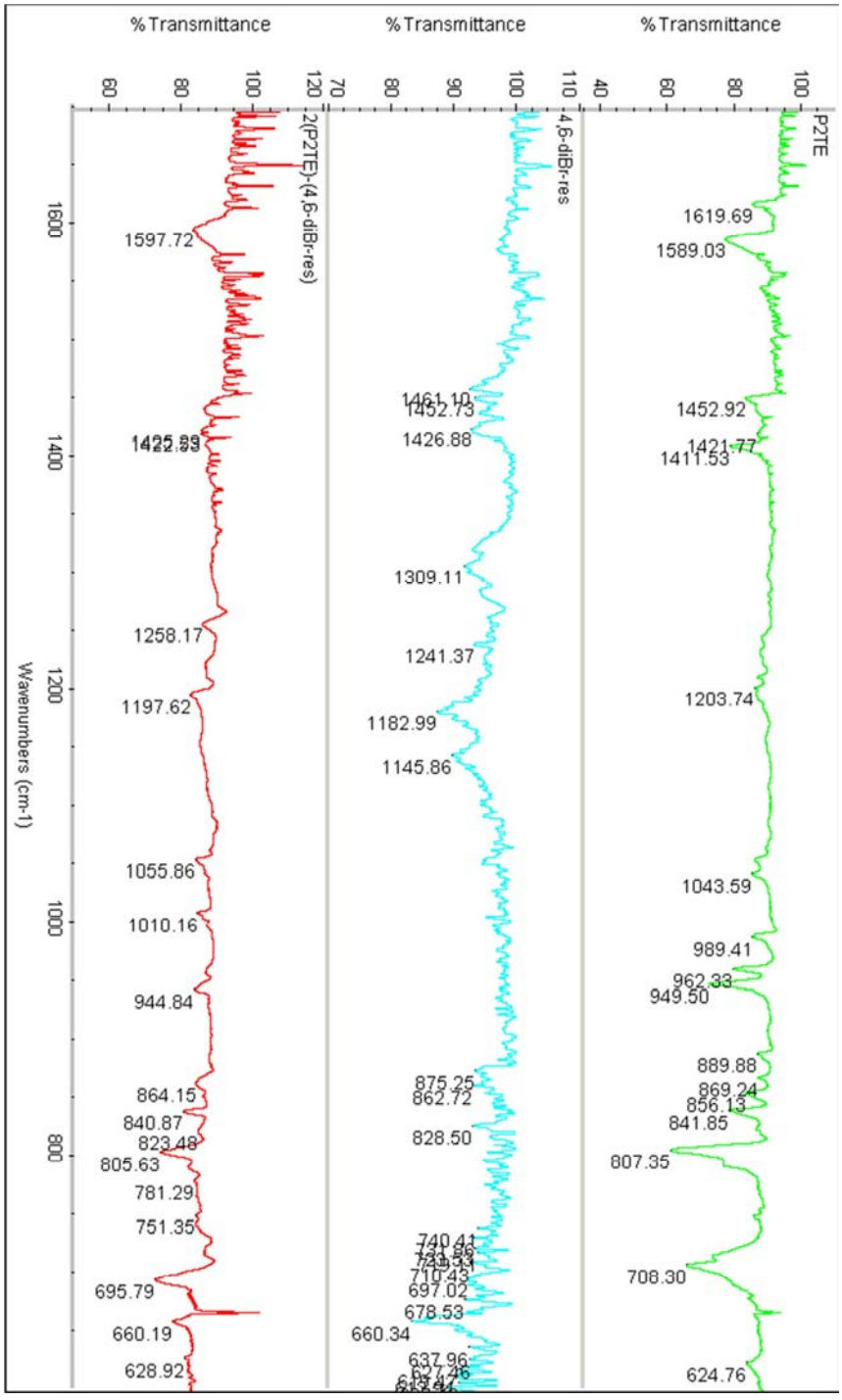

Figure B.1 Overlay of IR spectra of P2TE, 4,6-diBr-res and 2(P2TE)·(4,6-diBr-res)

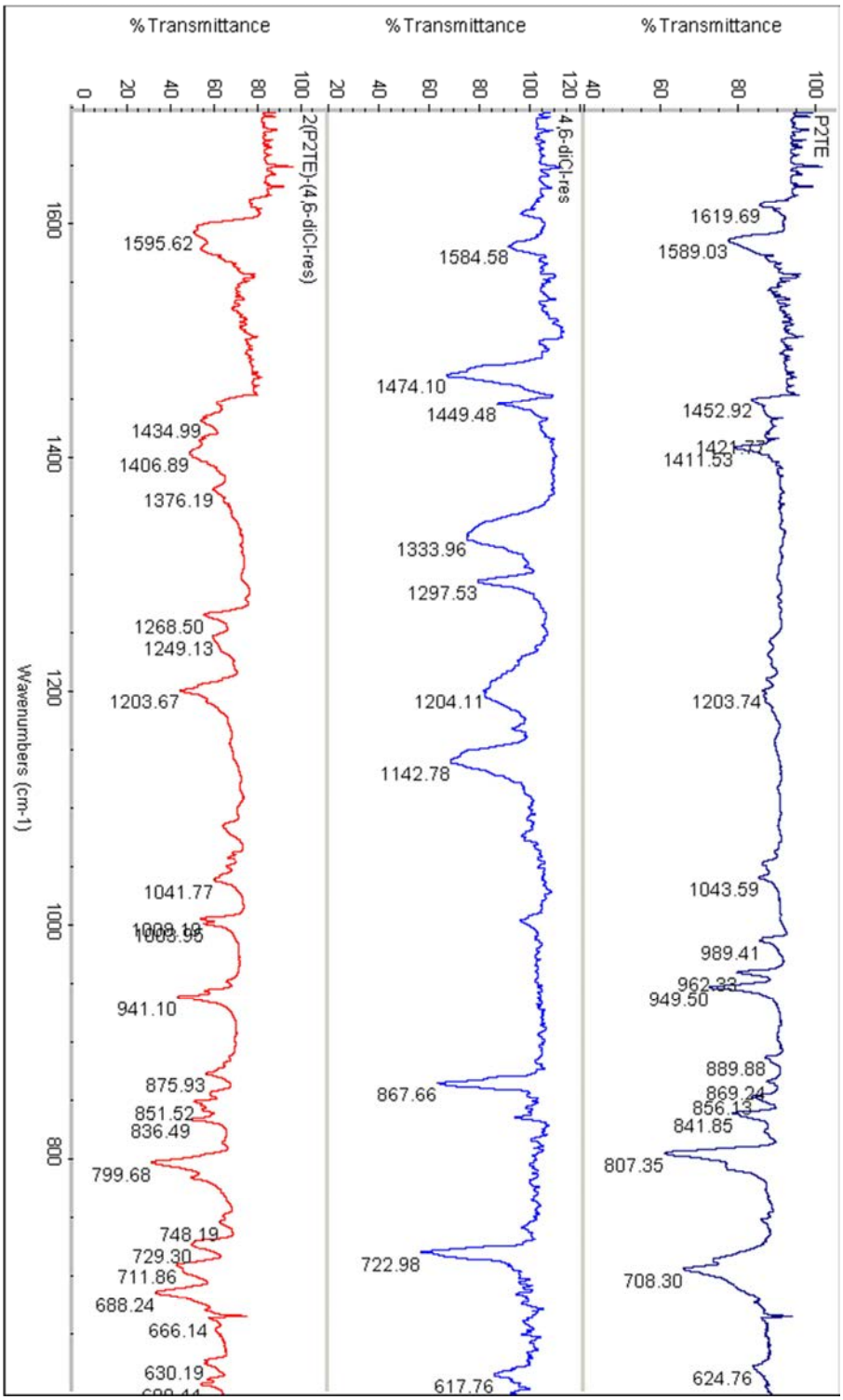

Figure B.2 Overlay of IR spectra of P2TE, 4,6-diCl-res, and 2(P2TE)·(4,6-diCl-res)

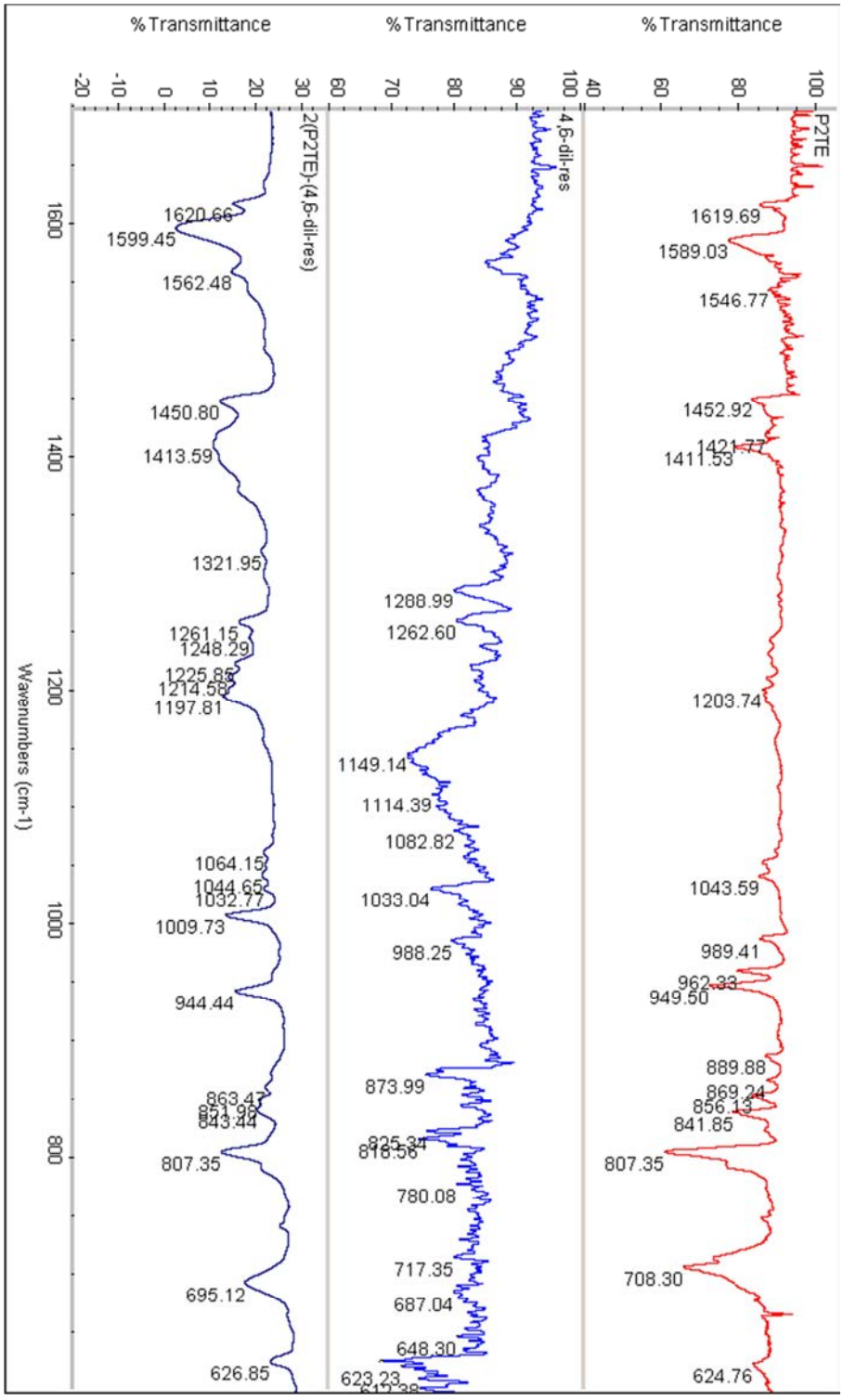

Figure B.3 Overlay of IR spectra of P2TE, 4,6-diI-res, and 2(P2TE)·(4,6-diI-res)